UNIVERSITÀ DEGLI STUDI DI BRESCIA

DIPARTIMENTO DI SCIENZE CLINICHE E SPERIMENTALI

DOTTORATO DI RICERCA IN INTELLIGENZA ARTIFICIALE IN MEDICINA E INNOVAZIONE NELLA RICERCA CLINICA E METODOLOGICA

---

settore scientifico disciplinare
MED/17

CICLO
XXXVII

TITOLO TESI

ARTIFICIAL INTELLIGENCE-BASED INTEGRATED APPROACH FOR SKIN CANCER RECOGNITION

NOME DEL DOTTORANDO

Dott. SIMONE SOGLIA

NOME DEL SUPERVISORE

Prof. PIERGIACOMO CALZAVARA-PINTON

ABSTRACT

Introduction: the incidence of melanoma is continuously increasing and it is responsible for the majority of skin cancer deaths. Early diagnosis and complete removal of the tumor tissue before the onset of deep invasion are the main factors for the reduction of its mortality and morbidity. For this reason, different non-invasive imaging techniques to allow the early and more accurate identification of malignant lesions have been developed.

Objectives of the study: this study aims to elaborate an AI integrated approach, based on images made using Line-field confocal optical coherence tomography (LC-OCT), able to correctly identify dermoscopically suspicious melanocytic lesions as benign, malignant or at uncertain prognostic significance.

Materials and methods: A retrospective study was conducted to elaborate and evaluate the accuracy of an AI model in distinguishing images of melanocytic lesions into three diagnostic categories: melanocytic nevi, atypical/dysplastic melanocytic nevi and melanoma. The analyzed images consisted of vertical sections (DICOM) acquired via LC-OCT. The set of LC-OCT DICOM images was enriched, in order to try to increase the signal/noise ratio (SNR) with respect to the investigation outcome with different filters (RAW, Gaussian, LOG and MERGED). The images filtered with Gaussian and RAW filter were used to extract pixel clusters, according to the SLIC Superpixels and Affinity Propagation (AP) Clustering algorithm. Regions of interest were extracted and image biomarkers were extracted with a library in R, called Moddicom.

Different machine learning models (bivariate logistic regression, decision tree and random forest) were trained to understand if any biomarker was able to discern melanoma from benign moles.

Results: 127 variables showed a statistically significant p-value on univariate testing. The most promising bivariate regression models were extracted. The performances on the training set are high, while those on the testing set are lower: this means that apparently good results of this technique are probably due to overfitting. Similarly, the decision tree and the random forest also showed excellent levels of accuracy, positive predictive value (PPV) and negative predictive value (NPV) for the training test with a drop in performance on the independent internal testing set.

Discussion and conclusions: In this pilot study we developed and demonstrated, for the first time in the literature, the feasibility of an artificial intelligence model for the in-vivo discrimination between benign melanocytic lesions, uncertain malignant potential lesions and melanoma based on LC-OCT images. We have identified several biomarkers potentially useful for this purpose.

Although this model has not yet demonstrated good results in terms of performance, several ways for its improvement have been identified and proposed.

ABSTRACT

Introduzione: l'incidenza del melanoma è in continuo aumento ed è responsabile della maggior parte dei decessi per tumore della pelle. La diagnosi precoce e la rimozione completa del tumore prima che inizi la fase di invasione profonda costituiscono le principali armi per ridurne mortalità e morbidità. Per questo motivo sono state sviluppate diverse tecniche non invasive di imaging per consentire l'identificazione precoce e più accurata delle lesioni maligne.

Obiettivi dello studio: questo studio si propone di elaborare un modello basato sull' utilizzo dell'intelligenza artificiale (AI), in grado di distinguere, partendo da immagini ottenute con la tomografia a coerenza ottica confocale (LC-OCT), lesioni melanocitiche sospette all'indagine dermoscopica in benigne, maligne o con significato prognostico incerto.

Materiali e metodi: è stato condotto uno studio retrospettivo per elaborare e valutare l'accuratezza di un modello AI nel distinguere le immagini di lesioni melanocitiche in tre categorie diagnostiche: nevi melanocitici, nevi melanocitici atipici/displastici e melanoma. Sono state analizzate sezioni verticali (DICOM standard) acquisite tramite LC-OCT. Il set di immagini LC-OCT è stato arricchito, per cercare di aumentare il rapporto segnale/rumore (SNR) con diversi filtri (RAW, Gaussiano, LOG e MERGED). Le immagini filtrate con filtro gaussiano e RAW sono state utilizzate per estrarre cluster di pixel, secondo l'algoritmo SLIC Superpixels e Affinity Propagation (AP) Clustering. Sono state estratte le regioni di interesse e i biomarcatori con una libreria in R, chiamata Moddicom.

Diversi modelli di machine learning (regressione logistica bivariata, albero decisionale e random forest) sono stati addestrati per capire se qualche biomarcatore fosse in grado di distinguere il melanoma dalle altre lesioni.

Discussione e conclusioni: In questo studio pilota abbiamo sviluppato e dimostrato, per la prima volta in letteratura, la possibilità di sviluppare un modello di intelligenza artificiale per la discriminazione in vivo tra lesioni melanocitiche benigne, lesioni a potenziale maligno incerto e melanoma, basato su immagini LC-OCT. Abbiamo identificato diversi biomarcatori potenzialmente utili a questo scopo.

Sebbene questo modello non abbia ancora dimostrato buoni risultati in termini di prestazioni, sono stati identificati e proposti diverse strade per migliorarlo.

INDICE

1. INTRODUCTION

Over the last 50 years, the incidence of melanoma has increased more rapidly than any other type of cancer.[1,2] Although it still represents less than 5% of all skin cancers, melanoma is responsible for the majority of skin cancer deaths.[3]

To date, the main prognostic factor for the patient is represented by early diagnosis and complete removal of the tumor tissue before the onset of deep invasion and the development of metastases.[4]

The standard diagnostic procedure begins with a visual, clinical and dermoscopic examination of the surface structures of the skin.[5] In case a suspicious lesion is found, an excisional biopsy is performed, and the removed tissue is sent to pathologists for histological examination.

The result of this time-consuming procedure is that nearly 60% of all skin biopsies lead to the diagnosis of benign lesions.[6] On the other hand, 20% of all skin cancers (including approximately one-third of melanomas) are missed at an early stage.[7]

For this reason, different diagnostic methods have been developed over the years that use non-invasive imaging techniques to allow the early and more accurate identification of malignant lesions.[8-10]

1.1 Melanoma

1.1.1 Epidemiology

Melanoma is a malignant tumor that originates from melanocytes. In 85% of cases, it arises on the skin and represents 5% of malignant skin tumors. More rarely, melanoma originates from melanocytes of the mucous membranes or from those located in extracutaneous sites such as the eye, ear and meninges. The incidence of melanoma is continuously increasing, with an estimated annual increase of 5-7% in the last twenty years, in particular, 4.4% per year in males, and 3.1% per year in females.[11]

The highest incidence rates were found in Australia (40/100,000 inhabitants) and New Zealand, followed by Northern European countries, while the lowest in Japan and Central Africa (0.4/100,000 inhabitants).

In the Italian population it is the second most frequent tumor in males under 50 years of age and the third most frequent in females under 50 years of age. In Italy there were almost 14,000 new cases in 2017 (with a slight preponderance in males).

1.1.2 Etiopathogenesis

Melanoma is a malignant neoplasm with a complex and heterogeneous etiopathogenesis in which both constitutional (genetic and phenotypic) and environmental risk factors are implicated. The main risk factors include: the number of common and atypical nevi, phenotypic characteristics, family or personal history of melanoma and/or carcinomas and precancerous lesions and the pattern of exposure to ultraviolet radiation.

Epidemiological data indicate that subjects with red or blond hair, freckles, light eyes, light complexion and little or no ability to tan (phototype I and II according to Fitzpatrick) easily develop rashes after sun exposure and run a higher risk of developing skin tumors. Furthermore, acute and intermittent sun exposure, especially in the first 18 years of life, correlates with a greater propensity to develop melanoma in adulthood. It has also been highlighted that greater intermittent exposure to the sun for short periods can be associated with a greater risk of developing melanoma in adulthood, especially if the subjects have a light phototype.[12]

A high number of nevi is an excellent indicator of melanoma risk, and the number of nevi tends to increase with sun exposure during childhood, reaffirming the importance of childhood exposure.

Approximately 10% of patients affected by melanoma have at least one first-degree relative affected by this pathology.[13]

The following genes, and the pathways dependent on them, are recognized as having a crucial role in the pathogenesis of melanoma: CDKN2A (p16CDKN2A-CDK4-RB and p14CDKN2A-MDM2-p53 pathway), NRAS-BRAF (MAPK and PI3K-AKT pathway), cKIT and MITF.[14]

1.1.3 Role of UV radiation in melanoma

The part of UV radiation that reaches the earth's surface includes UVB (280-320 nm), UVA2 (320-340 nm) and UVA1 (340-400 nm), each of which is responsible for different negative biological effects in skin cell populations.[15]

UVB acts predominantly anaerobically through direct damage to DNA which leads to the formation of pyrimidine-cyclobutane dimers and photoproducts 6-4.

UVB is the main inducer of erythema and is considered the main culprit of UV-induced carcinogenesis (Figure 1).[16]

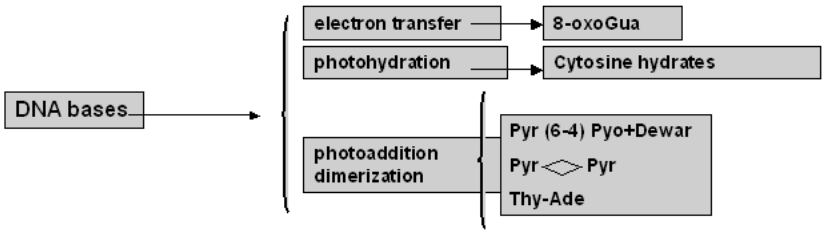

Figura 1. UVB effects on melanocytes.

The biological effects of UVA, on the other hand, are mainly mediated by aerobic photo-oxidation reactions which lead to the formation of oxygen radicals (ROS). These are capable of damaging DNA, leading to the formation of 8-oxo-7,8 dihydroguanine (8-oxogua) resulting in GC->TA transversions, as well as damaging the cytoplasmic membrane and cytoplasmic organelles (Figure 2). However, this latter mechanism is also shared by UVB which can therefore cause both aerobic and anaerobic damage.

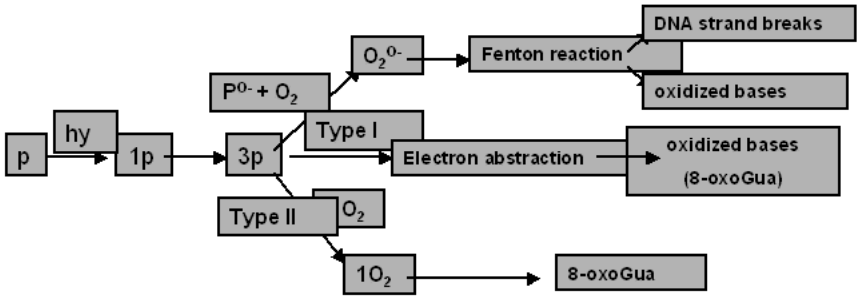

Figure 2. Molecular damage from UVA.

The UVA band has a longer wavelength than UVB and penetrates deeper into the skin. It is estimated that approximately 20-50% of the UVA emitted by sunlight reaches the basal layer of the epidermis where the melanocytes are located, while only 10-14% of the UVB reaches it. UVA is less effective than UVB in inducing erythema but is the main inducer of both immediate and persistent pigmentation.

In primary melanomas arising in sites regularly exposed to the sun, point mutations of the N-RAS oncogene are found, while none of the melanomas present in sites with intermittent sun exposure reported such mutations.[17]

These mutations are observed at the level of the dipyrimidine bases, a typical marker of UVB radiation, however there is no C-T (cytosine-thymine) transition, also typical of UVB radiation.

B-RAF mutations are mainly found in melanomas located in skin intermittently exposed to solar radiation.[18]

UV radiation can also interact with lipids, proteins and DNA, generating ROS, which activate transcription factors that influence cell survival, block the cell cycle or apoptosis.[19]

1.3.4. Primary and secondary prevention

Primary prevention consists in identifying, on the basis of scientifically documented data, the predisposing factors that can favor the onset of the disease: the objective is precisely to prevent its onset or at least reduce it. Health promotion means spreading correct lifestyles through clear and simple, but scientifically documented information, that can be carried out in everyday life[20] and implementing initiatives aimed at raising awareness. The aim is to raise awareness among the population regarding the disease and the need for measures to adopt to prevent it.[21,22]

Secondary prevention, on the other hand, concerns clinically healthy subjects who have already existing biological damage, with the aim of identifying the disease in an early or difficult to recognize phase. Thanks to the better understanding of clinical patterns and the development of dermatoscopy, the dermatologist has the diagnostic ability to evaluate the change of an evolving pigmented lesion.

1.2 Dermatoscopy

Dermatoscopy, surface skin microscopy or epiluminescence is a diagnostic method that constitutes a valid aid in the non-invasive diagnosis of melanoma and other pigmented skin growths.

The term dermoscopy was coined in 1920 by J. Saphier, a German dermatologist, who published a series of works using a diagnostic instrument similar to a binocular microscope which allowed an accurate morphological study of the anatomical structures of the skin. The application of the dermoscopy technique to pigmented skin lesions was inaugurated by Goldman in 1951[23] who, a few years later, created the first portable

manual dermoscope. With Rona Mackie's publications, the knowledge and use of dermoscopy begins to spread in the dermatological environment as a tool for pre-operative analysis of pigmented lesions. It was in the 1980s that we witnessed a growing number of publications regarding the morphological aspects of benign and malignant lesions and the correlations of dermatoscopic patterns with histopathological morphology. Currently, dermoscopy can be performed using various optical instruments. The one most frequently used in outpatient practice is the portable manual dermatoscope which has a fixed magnification of 10x. Another instrumentation is the digital videodermatoscope, consisting of a probe (camera) connected to a computer via optical fibers. The latter instrumentation allows enlargements of up to 200x and the presence of image archiving software allowing to evaluate the modifications of the pigmented lesions examined over time as well as the possibility of transmitting them remotely (teledermoscopy).

The performance of dermoscopy has been the subject of study by many authors and the results agree that the use of this technique significantly increases the diagnostic accuracy compared to the naked eye examination, allowing the differentiation between benign and malignant melanocytic lesions and facilitating the early diagnosis of atypical melanocytic lesions.[24,25]

Many studies in the literature investigated the concordance between dermoscopic features and certain histological structures. In the analysis of a pigmented lesion in dermoscopy, the color and structural characteristics are evaluated and are schematically divided into global and local (Table 1).

Local features	**Global Features**
Pigment network	Network pattern
Dots and globules	Globular pattern
Striae	Cobblestone pattern
Pseudopods	Homogeneous pattern
Blu-whitish veil	Starburst pattern
Blotches	Parallel pattern

Hypopigmentations	Compound pattern
Regression structures	Multicomponent pattern
horny pseudocysts	Lacunar pattern
Comedone-like openings	Nonspecific pattern
Exophytic papillary structures	
Maple leaf area	
Vascular structures	

Table 1. Local and global features of pigmented lesions at dermoscopy.

The color of the skin lesions is determined by the localization of the melanin pigment in the various skin layers: black is appreciated when the melanin is located at the stratum corneum level, the various shades of brown when it is located in the epidermis, gray-blue when it is in the papillary dermis and finally dark blue when it is in the reticular dermis. The red color is associated with the presence of blood vessels and the white color is often determined by the phenomenon of regression and/or healing lesions.

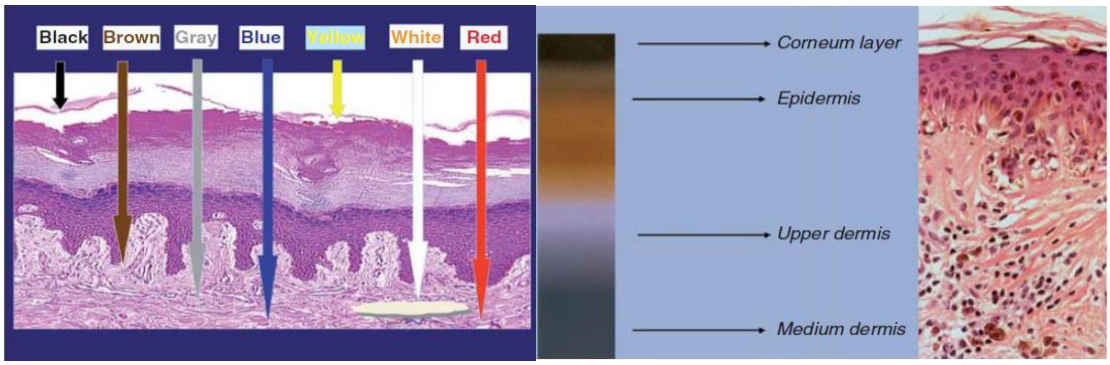

Figure 3. Colors in dermoscopy.

The analysis of the global characteristics of the pigmented lesion with the identification of a main pattern allows an initial diagnostic orientation.
The following patterns are distinguished.

Network or reticular pattern. It is the diagnostic pattern that allows us to establish whether the lesion is melanocytic or not. The pigmentary network can be typical or atypical. The

typical one is characterized by a network of narrow and regular meshes, homogeneous in color with a tendency to fade towards the periphery, while the atypical one is characterized by a network of irregular meshes, distributed in a disorderly manner in the context of the lesion itself.

The pigmentary network generally stops abruptly at the periphery, and the meshwork is commonly thickened in atypical areas. Due to the particular anatomy of the skin in this location, characterized by closely spaced hair follicles and lacking the typical alternation between epidermal interpapillary ridges and dermal papillae which is responsible for the typical reticular appearance, facial lesions take on a dermoscopic appearance called pseudoreticulum. The latter is characterized by an appearance of rounded meshes of uniform diameter. This dermoscopic appearance, as well as in nevi, is also present in solar lentigo and lentigo maligna for which the differential diagnosis requires the evaluation of other dermoscopic criteria.

Figure 4. Reticular pattern.

Globular pattern. It is characterized by the presence of numerous round or oval "globular aggregates" of variable diameter and ranging in color from brown to black. This pattern is common in congenital melanocytic nevi but also in Clark and Unna nevi (acquired melanocytic nevi).

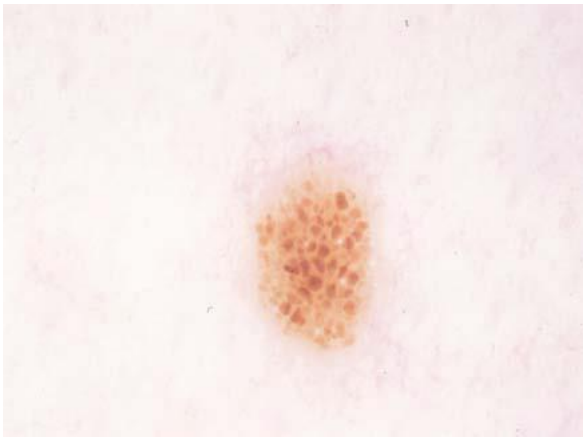

Figure 5. Globular pattern.

Cobblestone pattern. It is composed of large aggregated globular structures with frequent polygonal morphology. We find it most commonly in papillomatous dermal nevi (unna nevus).

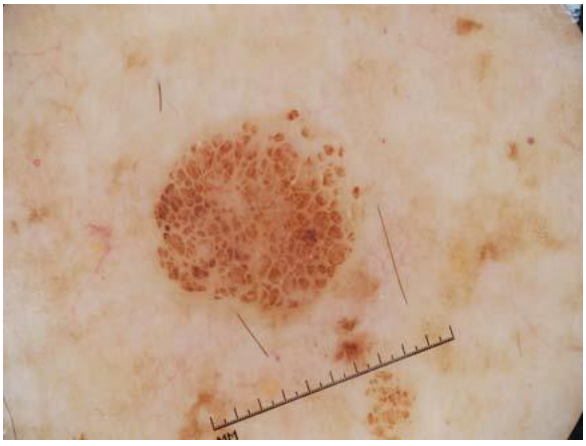

Figure 6. Cobblestone pattern.

Homogeneous pattern. Dermoscopically it is appreciated as a brown, grey-blue, grey-black pigmentation in the absence of a pigmentary network and other local dermoscopic parameters. This pattern represents a typical morphological character of the Blue nevus. However, it can also be appreciated in thrombosed hemangiomas and tattoos.

Figure 7. Pattern omogeneo.

Starbust pattern. It presents with pigmentary streaks distributed radially at the periphery of a pigmented lesion. It is mainly found in Reed nevi but can also be present in melanomas and the differential diagnosis between these is difficult.

Figure 8. Starbust pattern.

Parallel pattern. It is found exclusively in acral melanocytic lesions (palmar and plantar sites) in relation to the particular anatomy of these areas. Pigmentation can be along the furrows or along the skin ridges (furrow or parallel ridge pattern).

Figure 9. Parallel pattern.

Compund pattern. They are pigmented lesions with two associated dermoscopic structures.

Multicomponent pattern. Pigmented lesions with three or more associated dermoscopic structures are thus classified. This pattern is highly suggestive of melanoma although it can be observed in some cases in acquired and congenital melanocytic nevi.

Lacunar pattern**.** The characteristic of this pattern is the red-brown color. It is typically seen in angiomas.

Figure 10. Lacunar pattern.

Nonspecific pattern**.** This includes all lesions that do not fit into any of the global patterns mentioned above and are considered to be potentially malignant.

The local characteristics are instead represented by:

Pigment network. This consists of brownish pigmented lines on a light brown background. Histologically the lines correspond to the more or less pigmented and elongated interpapillary patches while the spaces between the links correspond to the dermal papillae. The presence of a pigmentary network is highly indicative of a melanocytic lesion regardless of its biological behavior.

Dots and globules. They are well-circumscribed pigmentary structures, generally round or oval with a diameter respectively less than and greater than 0.1 millimeters which can be regular or irregular in shape and distribution. The corresponding histological picture is characterized by aggregated foci of melanocytes, melanophages or even accumulations of melanin. The size and shape of the dots/globules reflects that of the pigmentary aggregates while the color depends on the anatomical level where these structures are located. Their distribution can contribute to the diagnosis of atypia, in association with the local characters mentioned above since in benign melanocytic lesions they are generally regularly distributed while in melanoma they are irregular both in shape and distribution.

Striae. They are linear structures of brown to black color, of variable thickness, not associated with the lines of the pigmentary network. They can be observed throughout the lesion but are best appreciated when located in the periphery. The latter are called radial striae. Histologically they are related to cases of junctional melanocytes. A symmetrical and radial arrangement over the entire lesion gives the lesion the "starbust" appearance that is generally observed in Reed's nevus. Their irregular distribution is instead strongly suggestive of malignancy.

Pseudopods. They are finger-like projections of dark pigment at the periphery of the lesion. Histologically they are similar to striae, so much so that some authors consider them variants of the striae themselves.

Whitish-blue veil. It is a diffuse confluent blue-gray pigmentation associated with pigment networks, dots, globules and/or striae. It cannot occupy the entire lesion. Histologically it corresponds to an acanthotic epidermis with compact orthokeratosis

and/or to the presence of intensely pigmented melanocytes in the superficial dermis. The veil is generally found in Spitz's and Reed's nevi and in melanoma.

Blotches. It is an intensely pigmented area caused by a large concentration of melanic pigment distributed at all levels of the epidermis and/or superficial dermis which obscures the underlying structures, often making it difficult to differentiate between the absence/presence of atypia.

Hypopigmentation. Localized or diffuse area of decreased pigment in the context of a pigmented lesion. It can be focal or multifocal. The histopathological counterpart obviously corresponds to areas of decreased melanic pigmentation. In this area it is not possible to identify any structure (globules, network, etc.).

Regression structures. Dermoscopically they appear as white areas and blue areas present individually or in combination. The white areas are also called scar-like because they resemble the dermoscopic picture of a superficial scar. The blue areas, also called blue-grey or "peppering", are foci with a dotted or diffuse appearance of blue-grey color. Differential diagnosis with the veil is often not possible. Histologically, the white areas correspond to fibrosis and the blue areas to melanosis (melanophages in the thickened papillary dermis). It is a rather indicative criterion for the diagnosis of melanoma.

Horny pseudocysts. They are rounded structures of variable sizes and white or yellowish in color. They correspond histologically to globules of intraepidermal horny material. They are predominantly observed in seborrheic keratoses.

Comedo-like openings. They are round or oval structures of brown color and correspond histologically to keratin plugs located in dilated follicular outlets. These are also observed especially in seborrheic keratoses.

Exophytic papillary structures. They are closely juxtaposed dome-shaped structures. They are commonly seen in papillomatous dermal nevi (Unna nevi) and also in seborrheic keratoses.

Maple leaf area. They are brown spots with appearance similar to maple leaves. Histologically they correspond to aggregates variable pigmented epithelial cells present in the superficial dermis. They are a pathognomonic finding of basal cell carcinoma (BCC).

Vascular structures. Various aspects of the vascular pattern can be recognized on dermoscopic examination. The appearence of vascularization were originally classified by Kreusch[26] and subsequently modified by Argenziano[27] as reported in Table 2.

Vascular structures	**Meaning**
Arborized vessels	Basal cell carcinoma
Crown vessels	Sebaceous hyperplasia
Comma vessels	Dermal nevus
Dots vessels	Keratinocyte tumors
Hairpin vessels	Common in thin melanomas, sometimes in seborrheic keratoses and keratoacanthomas
Irregular vessels	Melanoma

Tabella 2. Vascular structures at dermoscopy.

The diagnostic path to analyze a lesion dermatoscopically consists of two steps.[28] The first step involves differentiating between a melanocytic lesion from a non-melanocytic one, while the second allows the presumed distinction of a melanocytic lesion into malignant and benign. In case of atypia, the lesion must be surgically excised; the subsequent histological analysis will allow a definitive diagnosis of the nature of the lesion. The classic method for dermoscopically classifying a lesion is that of "pattern analysis", introduced by Pehamberger in 1987, which is based on the contemporary and

qualitative evaluation of the individual dermatoscopic criteria.[29] It is the method that allows to improve the diagnostic classification of the lesion, but requires dermatoscopic experience. For this reason, classification methods have been introduced, subject to various modifications, which facilitate the diagnosis of less experienced dermatologists. The diagnostic sensitivity of the expert clinician increases significantly when the instrumental evaluation is associated with an accurate anamnestic collection and careful clinical observation. Another easy-to-use algorithm for the evaluation of pigmented lesions is the "Seven-point system" proposed by Argenziano in 1998[30] which requires the identification of seven dermatoscopic criteria. Argenziano distinguishes three major and four minor criteria, assigning the former a score of two while the latter a score of one. If the overall result is equal to or greater than three, the melanocytic lesion is considered suspicious and therefore must be surgically removed for histological diagnosis (Table 3).

Major criteria (+2)	Minor criteria (+1)
Atypical pigment network	Irregular striae
Blu-whitish veil	Irregular pigmentations
Atypical vascular pattern	Irregular dots and globules
	Regression structures

Table 3. 7-point-check list.

Subsequently Argenziano et al. modified the algorithm by abolishing the distinction between major and minor criteria and assigning a score of 1 to all 7 criteria. The authors recommend surgical excision of lesions with a score equal to or greater than 1.[31]

Histopathology and staging

Melanomas are normally divided into different clinical-histological subtypes:

- Superficial Spreading Melanoma - SSM: it is the most common histotype of melanoma, representing approximately 70% of cases. The age of greatest incidence is between the fourth and fifth decade of life. Clinically it manifests itself as a flat or slightly raised lesion. The color is variegated, inhomogeneous with areas of pigmentation ranging from brown to red, pink, blue-grey or black, with focal areas of hypopigmentation. It can be

located in any skin and mucosal site although it prefers the trunk in males and the lower limbs in females.

- nodular melanoma (Nodular Melanoma – NM): represents approximately 9 to 15% of melanoma cases in the Caucasian population with an average age of diagnosis of 53 years. More frequent in men than women, it can affect all skin areas and in 11-25% of cases it is histologically associated with a nevus. Clinically it presents as a papule or nodule of regular hemispherical shape, with a blackish-brown or bluish-black color and a fleshy consistency. The lesion grows rapidly without an apparent radial growth phase unlike other forms of melanoma and easily undergoes erosion and bleeding with consequent formation of crusts.
- Lentigo Maligna (LM): represents approximately 9% of melanoma cases with an average age of diagnosis of 68 years; it is a slow-growing in situ melanoma that can evolve into invasive melanoma (Lentigo Maligna Melanoma - LMM). It is a tumor that most frequently affects elderly Caucasians, almost always located in photoexposed areas such as the face and is more frequently located on the cheek; women are affected twice as frequently as men. It appears as an irregular blackish-brown macule that slowly widens to form a patch.
- acral lentiginous melanoma: It represents approximately 4% of melanoma cases in the Caucasian population while it is more represented in Asian, Hispanic and African populations. It affects the glabrous skin, and particularly the palmar, plantar regions and the nail bed. It manifests itself as an irregularly pigmented macular lesion present for some time, which tends to grow slowly; on its surface it develops areas of regression that often make diagnosis difficult.
- unclassifiable melanoma
- rare variants (amelanotic melanoma, desmoplastic melanoma, spitzoid melanoma, animal type melanoma, nevoid melanoma).

According to the recommendations deriving from a review of the literature, patients with a suspicious skin lesion should be sent to a surgeon/dermatologist for surgical excision of the same, which should preferably be of the complete excisional type with margins of healthy tissue of 1-2 mm.

Each dermoscopic structure has a precise histopathological equivalent, representing the ideal bridge between the clinic and histology.[32] To understand this correlation it is essential to better clarify the in vivo behavior of skin tumors.
However, there are some limitations inherent to the two procedures that make it difficult to fully understand the anatomy of tumors and pathological findings in skin diseases. For example, vertical sections of histopathology cannot be sufficiently correlated with horizontal sections of dermoscopy, and some small dermoscopic structures are difficult to identify in histopathological sections. Finally, ex vivo pathology may differ from in vivo dermoscopic observations due to sample processing (modification of cellular appearance, observation of blood vessels, etc.).
With the aim of correlating dermoscopy and histopathology, some authors have carried out studies comparing horizontal histopathological sections with dermoscopic images in skin tumors in a limited number of patients.[33]
Similarly, over the years numerous works have been published on the correlation between pathological findings, dermoscopic structures and the other cornerstone of dermatological tumor diagnostics, confocal laser microscopy (RCM). [32, 34]

1.3 Confocal laser microscopy

The light source used by the RCM is a low-power laser with a near-infrared wavelength (830 nm diode, power <35 mW) that emits coherent monochromatic light.[35-36] The light beam passes from the source through a system of optical lenses and mirrors (Figure 11), finally scanning a focal point in the tissue. The subsequently reflected light passes through a pinhole to the detector: only the light of the analyzed area can enter through the hole, while the scattered "out of focus" light is blocked.

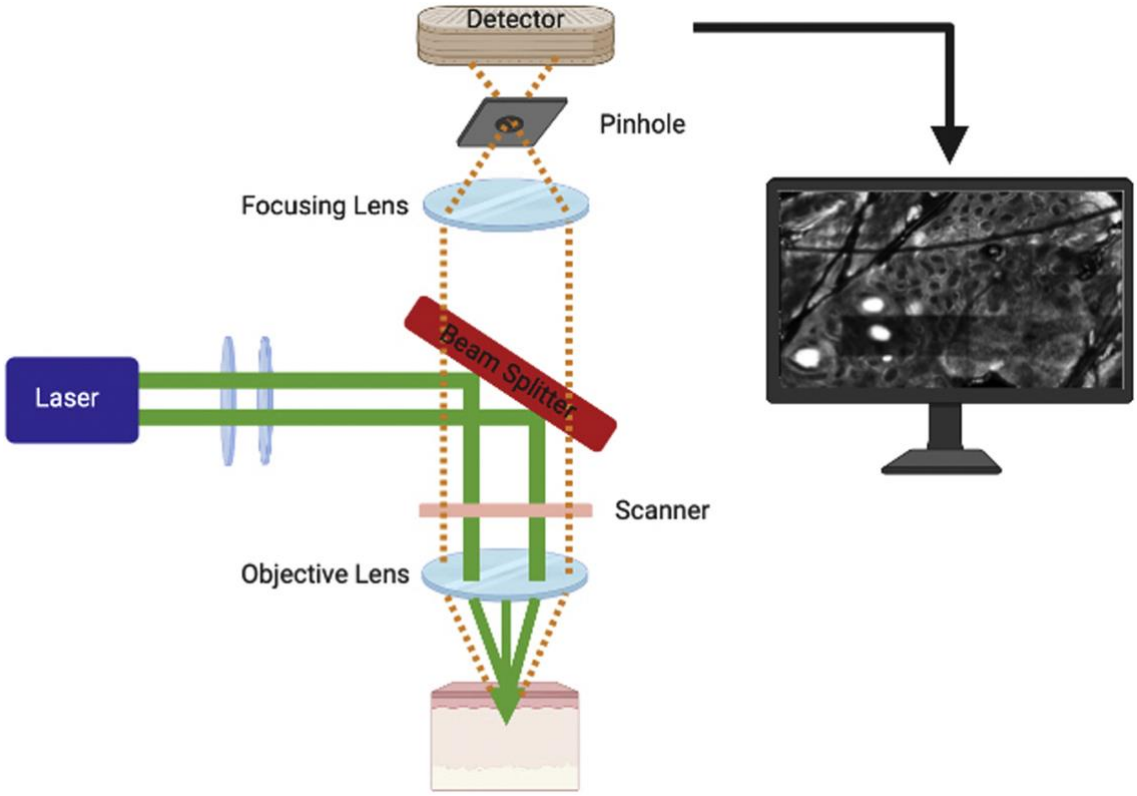

Figure 11. Diagram representing the optical operating principles of the RCM.

RCM images appear in a grayscale based on the relative refractive indices of tissue elements: those with a higher refractive index appear brighter. Melanin, for example, has a high refractive index of 1.7, so melanin-containing cells appear brighter than surrounding tissue elements.[37] The refractive indices of the sample are shown in Table 4. The basic RCM image is a single "optical section" that instantly displays a 0.5 - × 0.5 mm2 field of view in the horizontal (X-Y) plane. By moving the objective lens towards the skin, the focal plane is moved progressively deeper (on the Z axis).[37]

Skin components	Refractive index
Melanin in pigmented keratinocytes or melanocytes	1.7
Keratin	1.5
Hairs	1.37-1.7 (in base al contenuto di melanina)
Stratum corneum	1.55
Collagen	1.40-1.61
Organelles, fibrillar proteins, membranes and globular proteins	1.39-1.47
Derma	1.36-1.41
Cytoplasm e intracellular fluid	1.35-1.37
Epidermis	1.34
Red blood cells	1.40-1.42
Inflammatory cells	1.38-1.48
Serum and plasma	1.39
Nuclei	1.23-1.34

Table 4. Refractive index of the different skin components in descending order.

There are two types of RCM devices: fixed and manual (Figure 12).

Figure 12. RCM devices. A. Fixed device (Vivascope 1500). B. Manual device (Vivascope 3000).

The first type requires fixing the probe to the skin and its use is therefore limited to flat surfaces (for example the back).[35,36]

A metal ring is, in fact, fixed to the skin with a disposable polycarbonate adhesive window. A drop of immersion fluid (commonly mineral oil) is applied to the skin before applying the ring-window assembly, and a water-based gel is applied to the objective lens as another immersion medium.[36] The RCM probe is then magnetically coupled to the ring. The fixed RCM device allows 16 × 16 adjacent sections obtained at the same depth to be stitched together, creating mosaic images up to 8 × 8 mm2. The mosaic commonly

manages to enclose the entire lesion and also part of normal skin. If the diameter of the lesion is >8 mm, the ring is centered on the most suspicious area; if heterogeneous in color and large, the ring can be positioned so that the images sample disparate areas. The dermatologist can digitally control the movement of the probe in the horizontal plane and on the Z axis. From the skin surface to the superficial dermis, stacks of individual optical sections of the same X-Y area can be automatically acquired.

On the other hand, the manual device has a smaller probe that does not require attachment to the skin. After applying a drop of immersion oil to the surface, the movement in the X-Y plane depends on the manual sliding of the RCM probe over the skin. In this way, this device then allows imaging of curved anatomical sites (e.g. ears). Although it is possible to obtain image stacks with the manual device, it is not possible to reconstruct mosaic images, so its field of view is limited to 0.75 × 0.75 mm2.

1.3.1 RCM on healthy skin

Stratum Corneum

The stratum corneum appears shiny due to the high refractive index of keratin (Figure 13). The dark slits, representing the dermatoglyphics, separate the "islands" of keratinocytes.[38,39] Corneocytes measure 10 μm to 30 μm and appear as flat, polygonal anucleated cells.[40] The thickness of the stratum corneum varies from 0 μm to 15 μm, depending on the anatomical location.

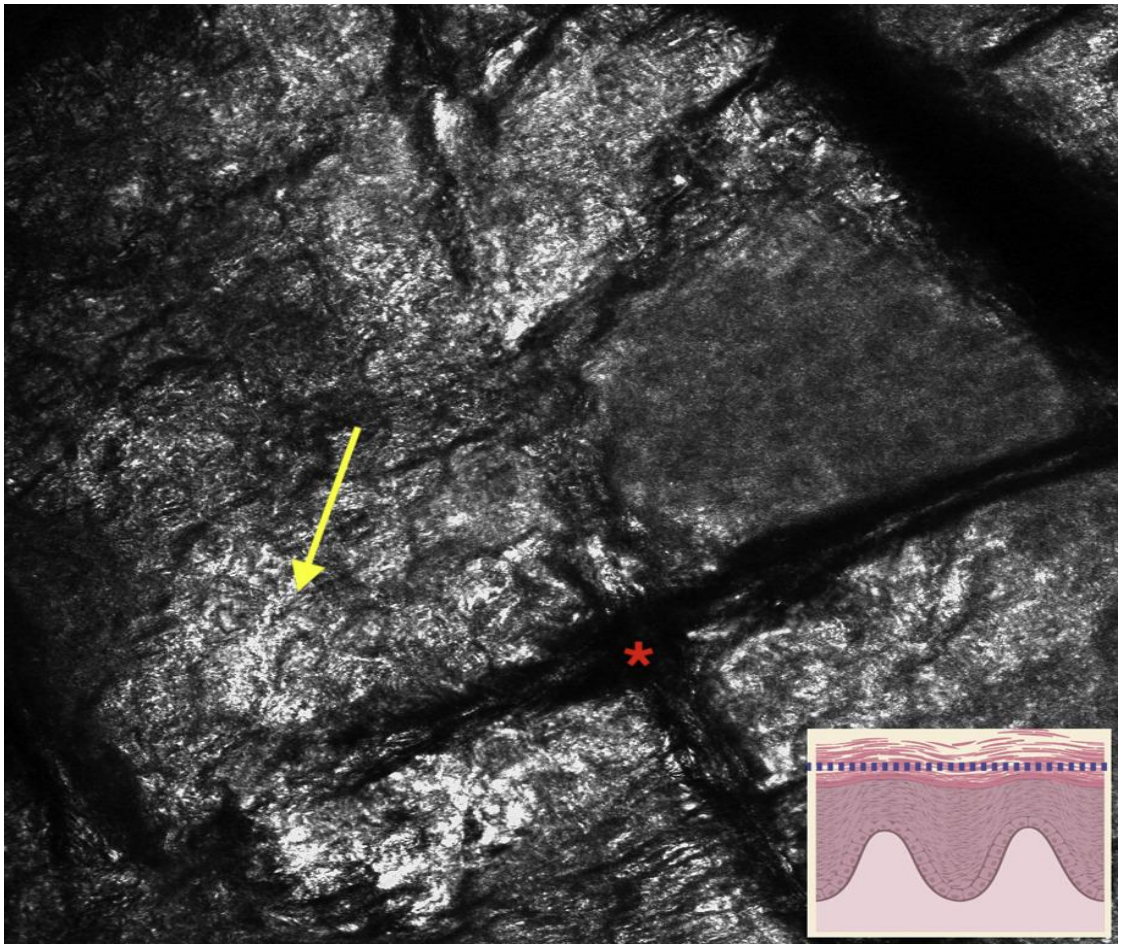

Figure 13. Normal skin. 0.5 × 0.5 mm2 section at the level of the stratum corneum showing a bright layer of flat anucleated keratinocytes (yellow arrow), interrupted by dark fissures (red asterisk) representing the dermatoglyphics.

Granular layer

The stratum granulosum lies 15 μm to 20 μm below the surface40. It consists of viable keratinocytes with central dark nuclei and surrounding refractile granular cytoplasm, due to the presence of keratohyalin organelles and granules.[39-41] This layer typically has a "honeycomb" appearance. resulting from the arrangement of keratinocytes arranged next to each other, showing bright polygonal cell outlines.

Stratum Spinosum

The stratum spinosum is located at a depth between 20 μm and 100 μm and has a higher keratinocyte density than the stratum granulosum.[39,40] Keratinocytes decrease in size with

increasing depth. The stratum spinosum also has a honeycomb appearance, consisting of bright polygonal keratinocytes with refractile cytoplasm and a dark central nucleus (Figure 14).

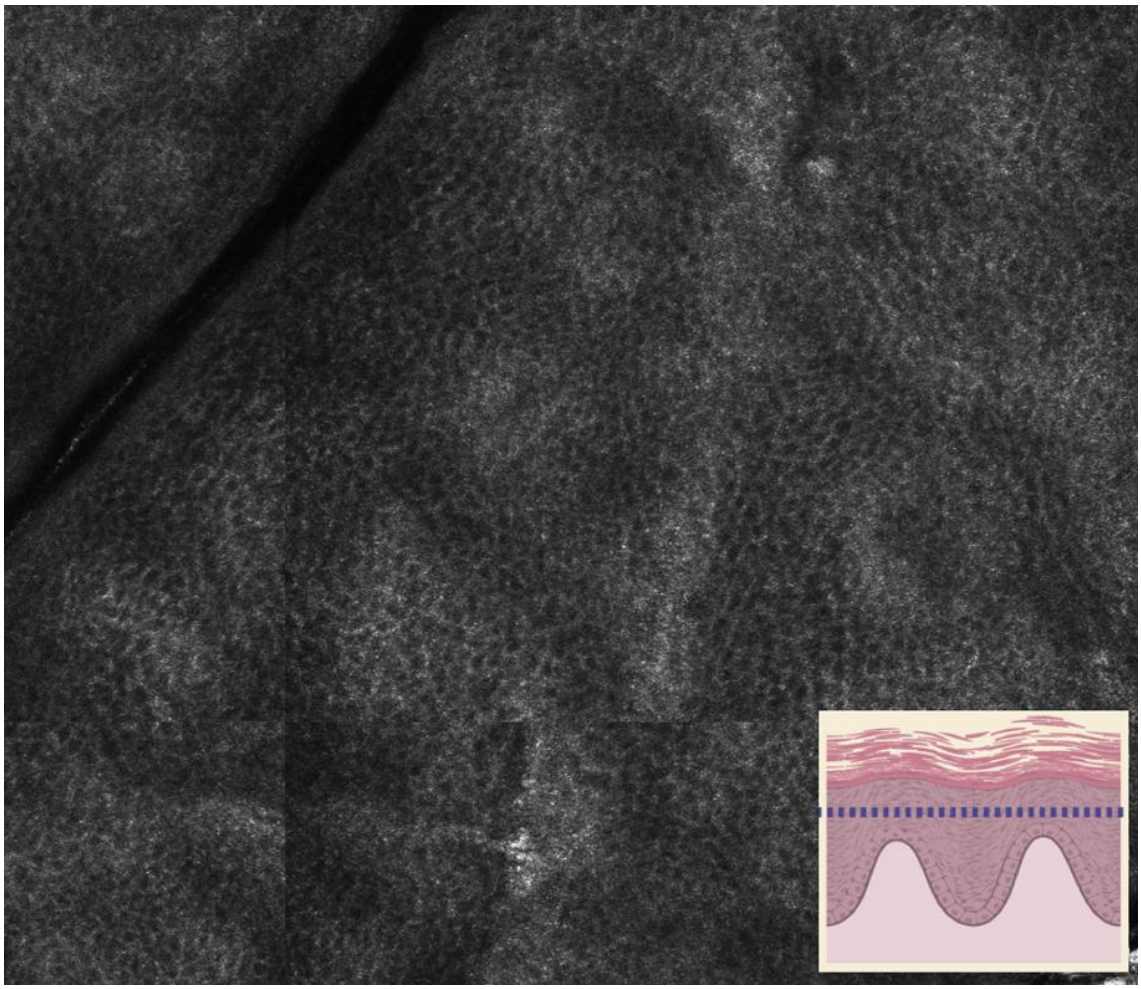

Figure 14. Normal skin. Mosaic (1.5 × 1.5 mm2) at the level of the middle spinous layer showing uniformly sized keratinocytes. The central nucleus of the keratinocytes appears dark, while the surrounding cytoplasm has well-demarcated bright polygonal outlines, forming a honeycomb pattern.

Basal layer and dermal-epidermal junction

At a depth between 50 μm and 100 μm, basal keratinocytes often show an opposite refractive pattern: the cells are brighter in the center than in the peripheral cytoplasm due to the presence of melanin. This produces a cobblestone pattern of numerous bright round

basal keratinocytes overlying the dermal papillae (Fig. 15). The cobblestone pattern is more pronounced in individuals with darker skin.[39-40] Within the basal layer melanocytes can be identified; they do not always take on the classic dendritic shape, but can have different shapes, including oval and fusiform.[41]

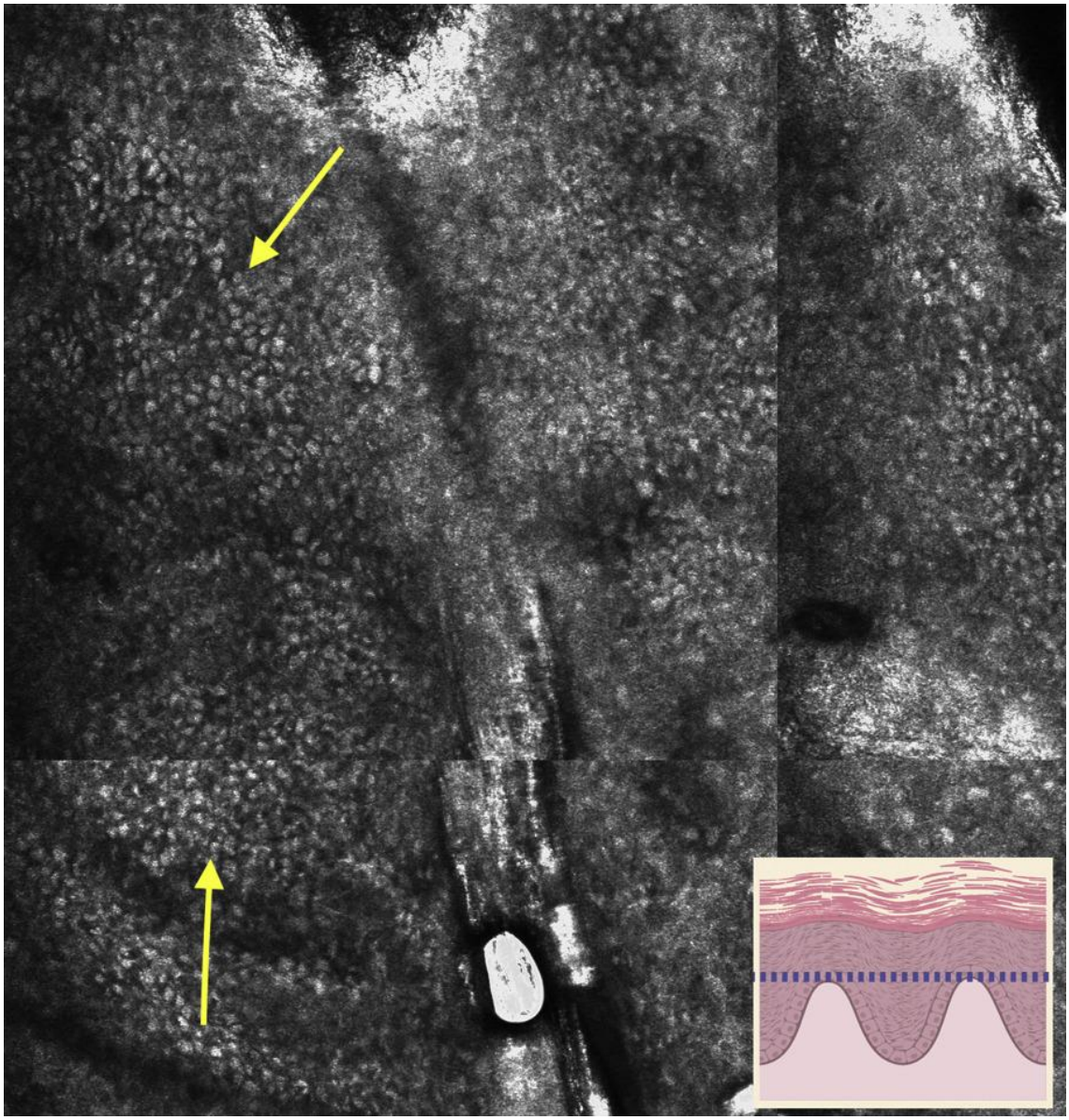

Figure 15. Normal skin. Mosaic (1 × 1 mm2) at the basal layer depicting bright keratinocytes (arrows) with a cuboidal or round shape, forming a cobblestone pattern.

At the dermoepidermal junction (DEJ) there are oval to round “rings” composed of brighter basal keratinocytes arranged circumferentially around darker, less refractile dermal papillae (figure 16). During image acquisition, blood vessels crossing the dermal papillae can be visualized in real time.

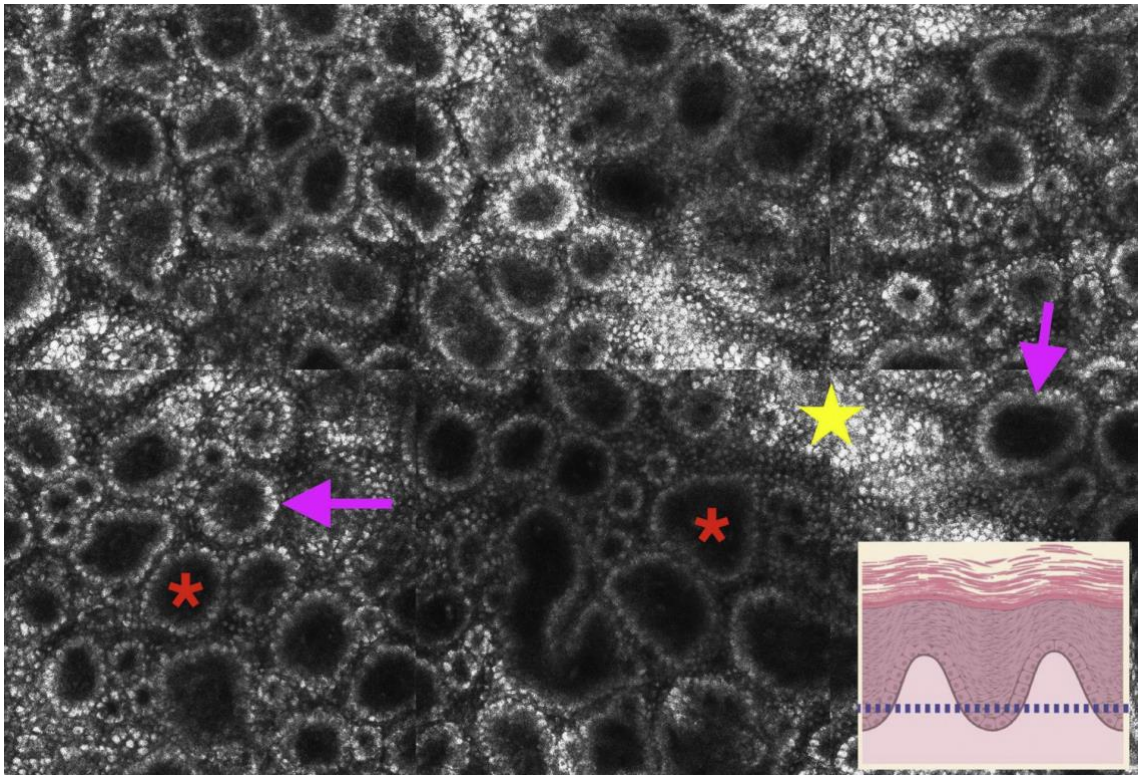

Figure 16. Normal skin. 0.5 × 0.5 mm2 optical section at the dermoepidermal junction showing dark dermal papillae (asterisks) with a well-demarcated border of bright cells (arrow) forming a ring pattern. This plane partially intersects the basal layer, and thus the cobblestone (star) pattern can be visualized intertwining between the papillae.

Superficial dermis

At a depth between 100 μm and 150 μm, collagen fibers can be seen forming a cross-linked pattern.[40] The dermis characterized by fibrosis or solar elastosis shows more refractile collagen than normal skin. In the deeper reticular dermis, collagen appears as thicker bundles arranged in parallel. Melanophages may appear as highly refractile, large,

irregularly shaped stellate cells without a visible nucleus. Only the superficial components of the adnexal structures can be seen by the RCM.

1.3.2 Basic terminology

Table 5 shows the most important terms used to describe the most frequent RCM patterns.

RCM pattern	Description	Histological correlate
	Epidermal layers	
Honeycomb pattern	Bright polygonal cell outlines of keratinocytes showing uniformity in size, shape, thickness and brightness of contours	Normal pattern of keratinocytes in the spinous and granulosa layers; the brightness is due to keratohyalin granules and organelles in the cytoplasm of keratinocytes
Atypical honeycomb pattern	Bright polygonal cell outlines of keratinocytes showing variability in size, shape, thickness and brightness of the outlines	Atypical keratinocytes of the spinous and granular layers showing a disorganized arrangement, crowding, and pleomorphism of the nuclei
Typical cobblestone patterm	Uniform pattern of bright, closely spaced round cells separated by less refractive polygonal contours	Keratinocytes are brightest in the center, due to the arrangement of melanin; normal pattern of pigmented basal keratinocytes and variant of the normal pattern of the spino-granular layers in darker skin
Atypical cobblestone pattern	Non-uniform pattern of bright, closely spaced round cells separated by less refractive polygonal outlines, with cells showing variability in size and brightness	Atypical, pigmented keratinocytes showing disorganized arrangement, crowding, and pleomorphism of the nuclei
Pagetoid diffusion	Bright round or dendritic atypical, nucleated cells in the suprabasal layers of the epidermis	Atypical melanocytes in the suprabasal layers; Langerhans cells can be difficult to distinguish from dendritic melanocytes
	Dermal-epidermal junction/papillary dermis	
Edged pattern	Dark dermal papillae surrounded by a ring-shaped border of bright cells	Normal pattern at the dermal-epidermal junction with dermal papillae surrounded by pigmented basal keratinocytes or melanocytes
Ring pattern	Pattern at the junction at low magnification showing a predominance of "edged papillae"	Normal presentation of the junction with pigmented basal keratinocytes or melanocytes at the sides and tips of the ridges; This aspect is also present in case of

RCM pattern	Description	Histological correlate
		lentiginous junctional proliferation of melanocytes
Meshwork pattern	Pattern at the junction at low magnification showing bright, interconnected aggregates giving a more enlarged appearance to the interpapillary spaces	Junctional nests of melanocytes along the sides and tips of the ridges, which sometimes fuse (bridging)
Dense nests	Compact, round, oval or polygonal cellular aggregates clearly delineated	Round, oval or polygonal junctional or dermal nests of melanocytes
Atypical cells	Large (>20 μm), rounded, or dendritic nucleated cells in the suprabasal epidermis, junction, or dermis, occurring as single cells or forming nondense clusters	Atypical melanocytes
Junctional architectural disorder	Architectural disorder including the presence of non-edged papillae, disorganized rings, atypical meshwork patterns, or poorly defined areas with no recognizable patterns	Irregular pattern, present in the context of neoplastic cell proliferation

Table 5. RCM basic terminology.

The detailed description of the presentation patterns of benign and malignant melanocytic neoplasms is beyond the scope of this dissertation. However, the presence of pagetoid spread, atypical mesh pattern with atypical cells and architectural disorder leans more towards a diagnosis of malignancy (Figure 17).

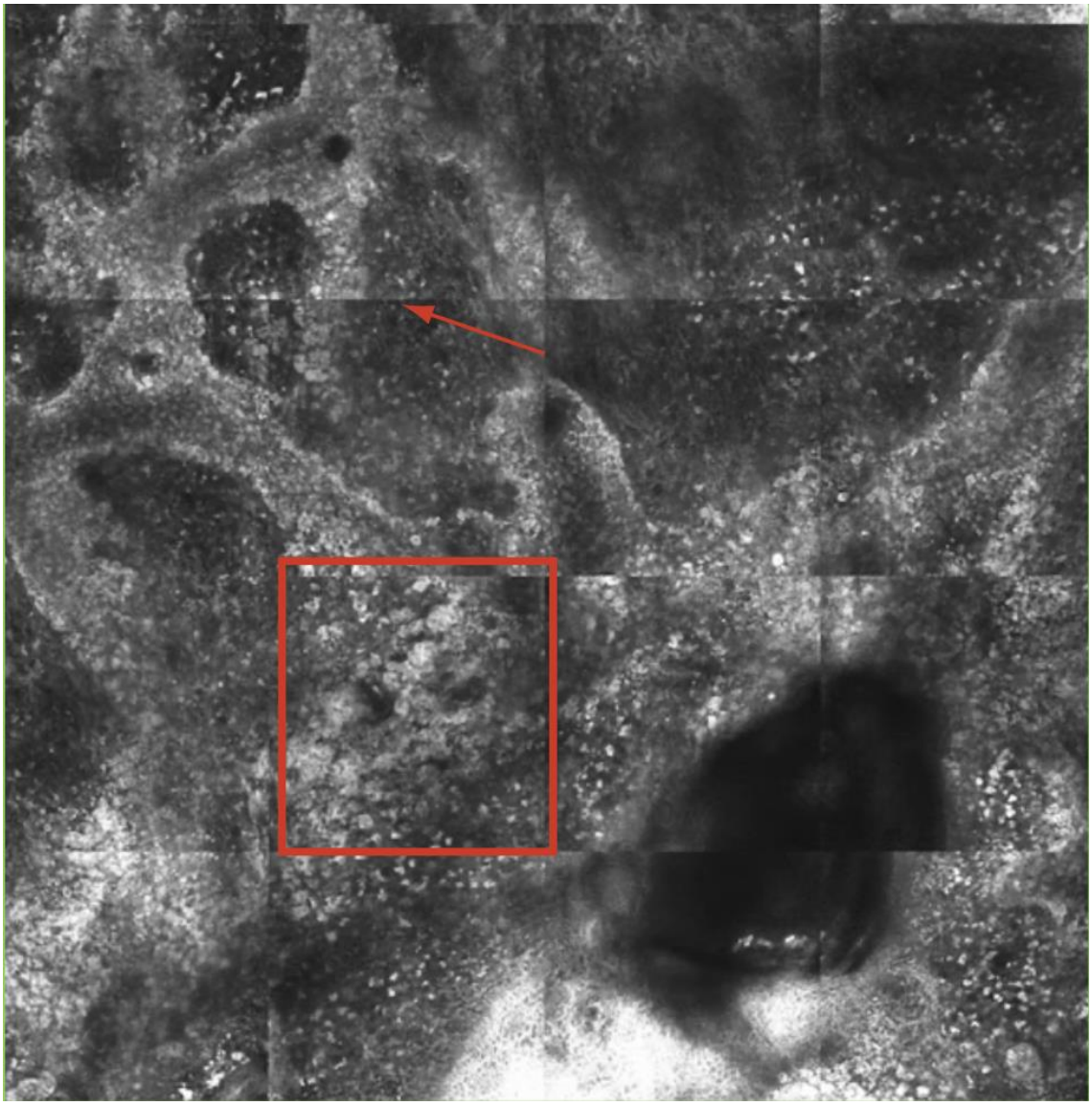

Figure 17. RCM mosaic (2 × 2 mm) of an SSM showing junctional thickening due to the presence of atypical melanocytes. At the periphery the network is more preserved (arrow) while it is replaced in the center by the presence of atypical cells (red square).

1.3.3 Clinical indications

The RCM should not replace but should instead be used as an additional tool to the clinical and dermoscopic examination.[42] Currently, the main clinical application of RCM is the diagnosis of equivocal skin lesions with a low to moderate pretest probability of malignancy. RCM is not intended to diagnose lesions with clear criteria for malignancy

based on clinical and dermoscopic examination. In particular, RCM is useful in cases where it is more difficult to resort to a biopsy examination: adults with lesions in aesthetically sensitive areas (for example, the face) or regions with slow wound healing (for example, the lower limbs).

Indeed, Borsari[43] found in a retrospective analysis that one of the best indications for RCM is the diagnosis of localized lesions on sun-damaged skin, particularly the head and neck areas.

Several studies have shown that RCM increases the diagnostic accuracy of melanoma. A systematic review pooling data from 5 studies including 909 lesions found a sensitivity of 93% (95% confidence interval [CI] 89-96%) and a specificity of 76% (95% CI 68-83%). [44]

Another possible application of RCM is the presurgical margin assessment of skin tumors to facilitate surgical planning. After obtaining a biopsy sample, a clinical dermoscopic evaluation of a basal cell carcinoma, for example, is not reliable in evaluating the margins of the tumor, particularly in certain histotypes with a higher risk of recurrence such as scleroderma basal cell carcinoma.[45]

The presentation of lentigo maligna in aesthetically sensitive areas and the difficulty in identifying clear surgical margins, with an associated significant recurrence rate, make this melanoma hystotype a therapeutic challenge.[46] To this end, RCM has been used for planning surgical margins of lentigo maligna, particularly in recurrent cases after surgery.[47]

Alongside these main applications, RCM can also have a role in other fields: the monitoring of tumor response following the use of non-invasive treatments,[48] the monitoring of possible tumor recurrences on surgical scars[49] and the diagnosis of inflammatory skin diseases.[50]

1.3.4 Limitations

Despite its great usefulness, this technique has a limited penetration depth and does not allow 3D reconstructions to be obtained, therefore it does not allow us to fully understand the in vivo architecture of the analyzed lesion. As already explained, RCM views the skin in horizontal sections similar to dermoscopy. Therefore, a 3D representation of the skin

anatomy is not possible with this technique.

In response to these needs, a new optical technique called Line-field Confocal Optical Coherence Tomography (LC-OCT), a non-invasive in vivo imaging device with deep penetration and high resolution, has recently been developed.[51]

1.4 LC-OCT

LC-OCT combines the physical principles of OCT and RCM, with a penetration to a depth of ~400 µm and an isotropic resolution of ~1 µm. The device consists of a manual probe connected to a mobile structure incorporating a central unit and a display. You can record both short videos and image captures from surface to depth (stack). The instrument has an axial resolution of 1.1 µm, a lateral resolution of 1.3 µm, and a field of view of 1.2 mm × 0.5 mm (vertical) and 1.2 mm × 0.5 mm (en -face). Images are displayed in grayscale. Immersion oil is applied between the glass window of the probe and the skin surface.[52]

Combining the advantages of OCT (greater penetration, imaging with vertical and horizontal sections) and RCM (high resolution), this instrument appears to be particularly suitable for studying skin anatomy. Furthermore, it offers the possibility of reconstructing a 3D image of the lesions and, thanks to a dermoscopic camera integrated into the same probe, to precisely visualize the point of the lesion we are analyzing (Figure 18).

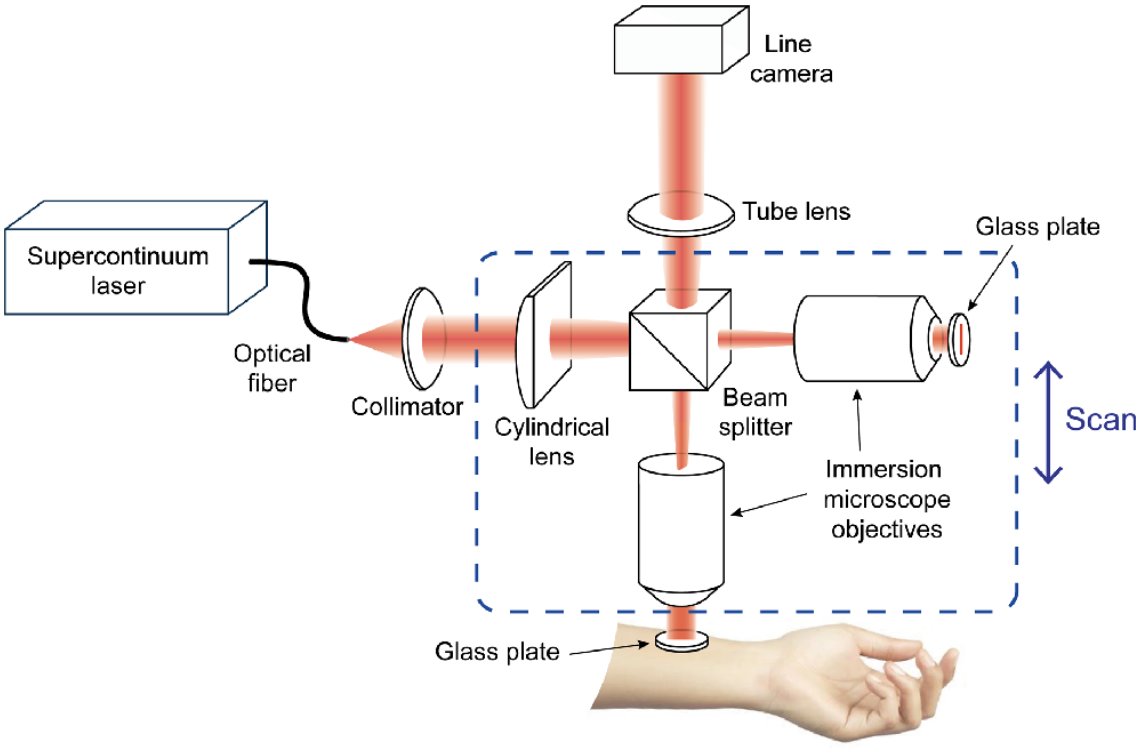

Figure 18. Operation diagram of the LC-OCT. The instrument consists of a Linnik-type interference microscope, i.e. a Michelson interferometer with an objective in each arm. The skin is illuminated by a broadband light beam generated by a supercontinuum laser. The interferometric signal is detected by a line scan camera. The entire interferometer is moved to scan the tissue in depth.

Despite the relative novelty of the tool, several studies have been carried out to evaluate its possible applications in dermatology.

1.4.1 Healthy skin

In LC-OCT images, individual cells and even the nuclei that compose them can be distinguished, as well as follicular outlets and blood vessels. En-face and vertical images show significant variations depending on the anatomical position.

The stratum corneum in vertical sections appears composed of rows of corneocytes and sometimes hyperreflective scales. Erosions appear as dark, irregular discontinuities on the surface. Keratinocytes appear as slightly darker polygonal cells, which show bright

outlines and decrease in size from the stratum corneum to the stratum granulosum and spinosum. Hair follicles are visible as dark longitudinal shadows, sometimes with a shiny hair shaft. The dermal-epidermal junction appears as a thin dark line made up of a layer of small basal cells that separates the epidermis from the papillary dermis, which appears hyperreflective. Blood vessels are represented as hyporeflective linear and convoluted structures (Figure 19).

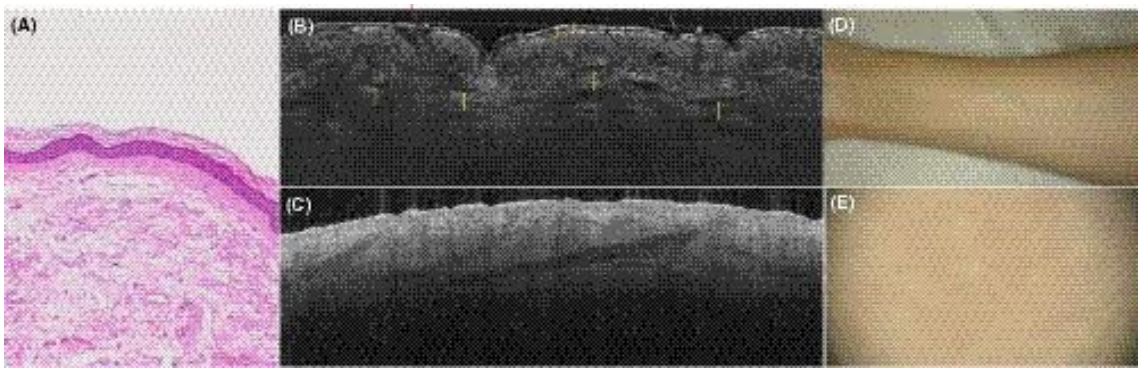

Figure 19. Comparison of hematoxylin-eosin sections, vertical LC-OCT images, and OCT images of a healthy forearm. (A) Hematoxylin-eosin section (10x magnification). (B) Vertical LC-OCT section (1.2 × 0.5 mm) shows that the stratum corneum is composed of corneocytes, and detached hyperreflective scales are also visible (blue arrow). Erosions appear as a dark and irregular discontinuity of the surface (red arrow). Keratinocytes are slightly darker polygonal cells, showing bright outlines (orange arrows). Hair follicles are visible as dark longitudinal shadows (green area), sometimes with a bright hair shaft (green arrow). The dermal-epidermal junction appears as a thin dark line consisting of a layer of small basal cells (white arrows), which separates the epidermis from the hyperreflective papillary dermis. Blood vessels are depicted as hyporeflective linear and convoluted structures (yellow arrows). (C) The same healthy skin on the right forearm (6 × 1 mm) in OCT, showing less architectural and cytological detail (D) clinical photo (E) its dermoscopic correlate.

In the en-face mode (Figure 20), individual hyperreflective corneocytes of 10-30 μm are visualized on the surface of the stratum corneum as in RCM. The keratinocytes that make

up the epidermis appear as polygonal cells with dark nuclei and are arranged in a sort of honeycomb pattern that appears regular. More pigmented keratinocytes appear brighter and create a cobblestone pattern. Hair follicles are very well distinguishable concentric round structures, with a dark central opening, surrounded by a multilayer of darker epithelial cells. The dermal-epidermal junction shows a regular ring architecture, composed of round to oval, dark dermal papillae centered by capillary loops. Hyperreflective collagen fibers and bundles and linear and rounded hyporeflective blood vessels dominate in the papillary dermis.

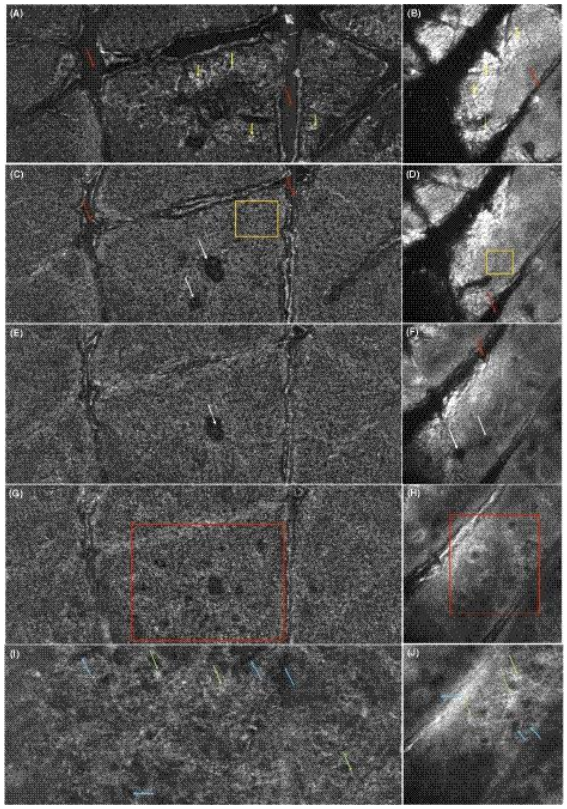

Figure 20. Comparison of en-face RCM and LC-OCT images of the skin of a right forearm. (A) In en-face mode (0.5 × 1.2 mm) in LC-OCT images, single hyperreflective corneocytes of 10–30 μm can be seen in the stratum corneum (yellow arrows) as in RCM (B). (C) The keratinocytes that make up the epidermis are polygonal cells with dark nuclei and appear in a regular honeycomb pattern (orange area). The same can be seen in the

RCM images (D). Skin folds appear as sharply demarcated linear non-refractive furrows between groups of keratinocytes (red arrows) in (A and C) but also in RCM images (B, D, F). In (C and E) LC-OCT images as well as in (F) RCM, hair follicles are very well distinguishable concentric round structures, with a dark, round, central opening surrounded by a multilayer of darker epithelial cells (white arrows). (G and H): The dermal-epidermal junction, in LC-OCT and RCM images of normal skin has a regular ring architecture with dark round to oval dermal papillae centered by dermal capillary loops (red area). (I and J) In the papillary dermis in LC-OCT, but also in RCM, hyperreflective collagen fibers and bundles (green arrows) and linear and rounded hyporeflective blood vessels (blue arrows) predominate.

1.4.2 Basal cell carcinoma

LC-OCT has proven to be very useful in the diagnosis of basal cell carcinomas.[53] Lobules, tortuous blood vessels, and the presence of small bright cells within the epidermis are the LC-OCT criteria most frequently associated with the diagnosis of BCC.

Lobules represent an extremely important criterion as they correspond to the most distinctive histological feature of BCC (aggregates of basaloid cells growing in the dermis) and have previously been identified as such by studies with RCM[54] and OCT.[55] On LC-OCT the lobules are typically characterized by a triad of colors, a bright outer rim surrounding a darker middle one and an inner gray nucleus. The external bright edge is characterized by a greater reflectivity than the surrounding stroma probably due to the compression (mass effect) exerted by the tumor islands on the collagen fibers.

The medium dark border probably corresponds to peritumoral deposition of mucin. The gray nucleus instead corresponds to a dense cellularity predominantly oriented along the same axis. This probably explains the presence of a peculiar pattern, called millefeuille, as it recalls the arrangement seen in the French dessert of the same name: it corresponds to a laminated structure in which the orientation of the basaloid cells is predominantly parallel to the epidermis. This pattern can be visualized thanks to the cellular resolution of LC-OCT, while it could not be appreciated by previous OCT technologies. The millefeuille pattern represents an added value of LC-OCT compared to traditional OCT and HD-OCT, for which the nucleus of a BCC lobule was simply defined as signal-free,

hyporeflective or grey.[56]

Blood vessels appear as dark structures within the dermis, especially near tumor islands (neo-angiogenesis), as previously observed in histopathology and other non-invasive imaging techniques. They are particularly easy to identify with the in vivo/video LC-OCT acquisition mode where you can capture the presence of red blood cells flowing within them.

The presence of bright cells of various shapes and sizes, some dendritic, was detected both within the epidermis and lobules in most BCCs. Their histopathological correlate is probably represented by immune cells and activated melanocytes.

Significant differences were detected between various subtypes of BCC. Histopathologically, superficial BCC is characterized by tumor islands resting on the epidermis and a lack of obvious stroma involvement. Similarly, on LC-OCT examination, there is a greater probability of superficial BCC when lobules connected to the epidermis with an unmodified stroma are observed; the lobules are more frequently hemispherical and less frequently elongated, they tend to be small, they less frequently show the classic triad of colors and the presence of bright cells (Figure 21).

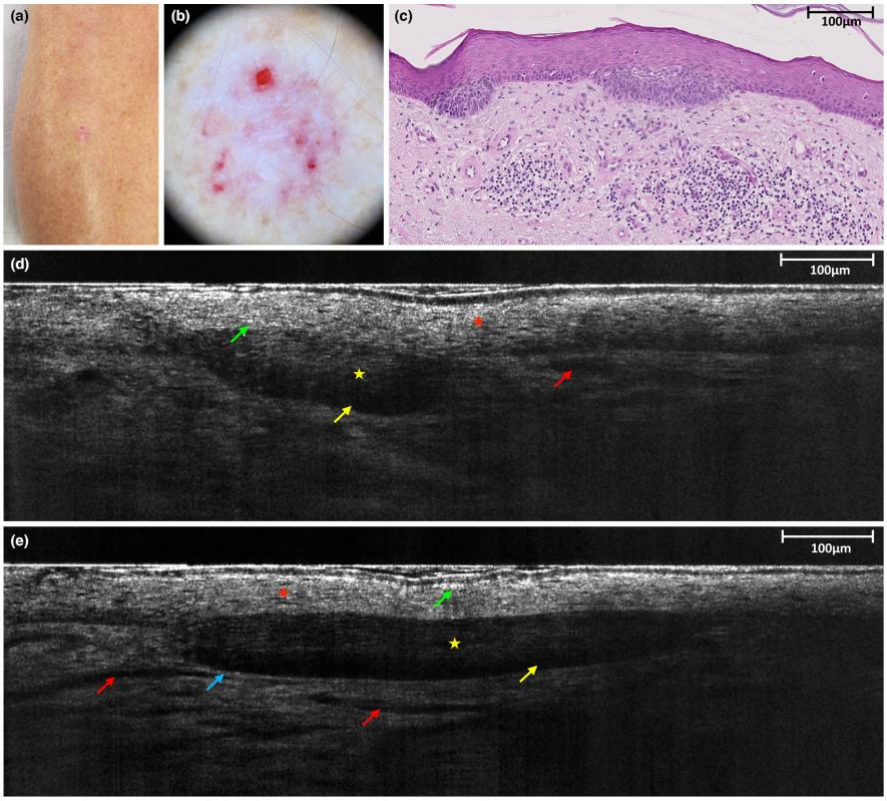

Figure 21. Superficial basal cell carcinoma (sBCC) on the right anterior leg of a 65-year-old woman: clinical (a), dermoscopic (b), and histopathological (c) presentation; LC-OCT images (d, e). The LC-OCT examination reveals the presence of hemispherical lobules composed of a gray internal nucleus characterized by the peculiar milfoil-like appearance (yellow stars), surrounded by a dark border particularly visible in the deepest part of the lobule (yellow arrows). An outer bright rim is only partially visible in the deepest part of the lobules (blue arrow). The lobules are closely connected to the epidermis (red stars). Blood vessels are visualized as well-defined hyporeflective structures, of various shapes/sizes, located within the dermis and especially close to the lobules (red arrows). Small, bright cells can be seen as hyperreflective structures within the epidermis (green arrows).

Nodular BCC, however, shows lobules not connected to the epidermis and stromal changes. The lobules are frequently large and contain large bright cells (Figure 22).

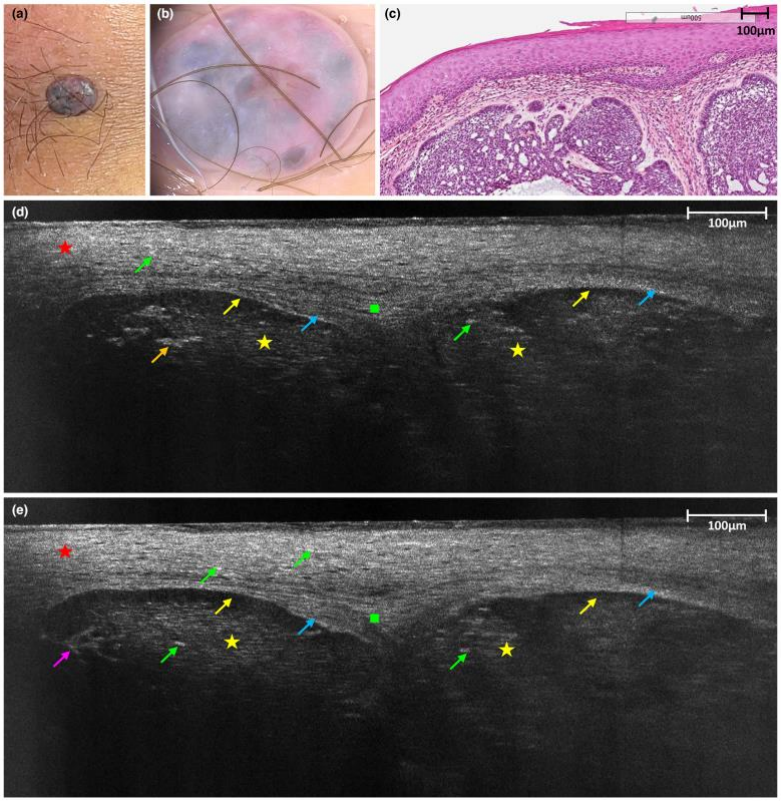

Figure 22. Nodular basal cell carcinoma on the right buttock of a 71-year-old man: clinical (a), dermoscopic (b) and histopathological (c) presentation; LC-OCT images (d, e). The LC-OCT examination reveals the presence of macrolobules composed of a gray

internal nucleus characterized by the peculiar milfoil pattern (yellow stars) surrounded by a dark intermediate border (yellow arrows) and a bright external border (blue arrows). The lobules are clearly separated from the epidermis (red stars). Stroma changes, such as elongation and increased brightness, are visible (green squares). Small bright cells can be seen as hyperreflective structures within the epidermis and lobules (green arrows). Large (orange arrow) and bright dendritic cells (pink arrow) are also visible within the lobules.

Regarding infiltrating BCC, the strongest predictor is the presence of branched lobules, which probably correspond to the BCC filaments seen in histopathology, and the “dark sillhouettes” described in RCM (Figure 23).

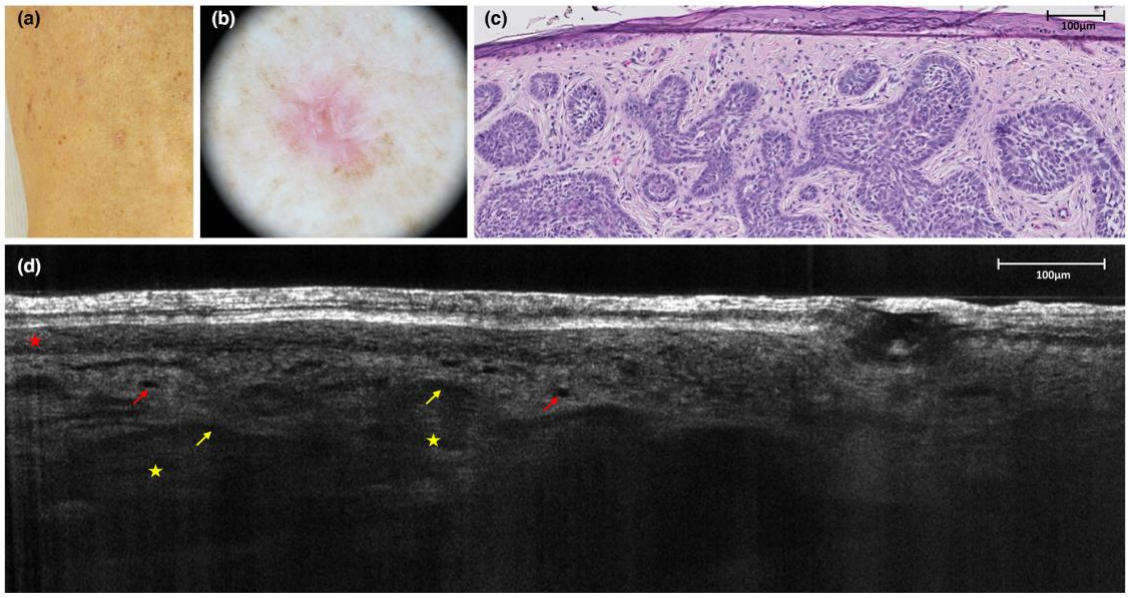

Figure 23. Infiltrative basal cell carcinoma of the right leg of a 79-year-old man: clinical (a), dermoscopic (b) and histopathological (c) presentation; LC-OCT image (d). The LC-OCT examination reveals the presence of branched lobules composed of a gray internal nucleus characterized by the peculiar milfoil pattern (yellow star) surrounded by a dark border (yellow arrows). The lobules are clearly separated from the epidermis (red star). Blood vessels are visualized as well-defined hyporeflective structures, of various shapes/sizes, located within the dermis and especially close to the lobules (red arrows).

1.4.3 Squamous cell carcinoma

LC-OCT can identify the main features of AK and SCC and help distinguish these two conditions. Hyperkeratosis, acanthosis, parakeratosis, erosion/ulceration, disorganized epithelial architecture, dyskeratotic keratinocytes, crowded nuclei, atypical nuclei, tumor budding and dilated vessels represent the important features of both AK and SCC.[57] Furthermore, the presence of a poorly defined dermal-epidermal junction represents the characteristic most associated with invasive tumors. Disorganized epithelial architecture reflects a loss of orderly maturation of keratinocytes, while the presence of dyskeratotic keratinocytes indicates that altered keratinization processes are taking place. The nuclei of keratinocytes are visible as well-demarcated hyporeflective oval areas and their irregularity in shape and size can be considered an indirect sign of keratinocyte pleomorphism.

Compared to AKs, SCCs have a significantly greater average thickness both as regards the lesion itself and the stratum corneum and a disorganized epidermal architecture is more frequently found in the second case. A poorly demarcated dermal-epidermal junction represents the morphological characteristic that more precisely allows us to distinguish SCCs from AKs (Figure 24, 25).

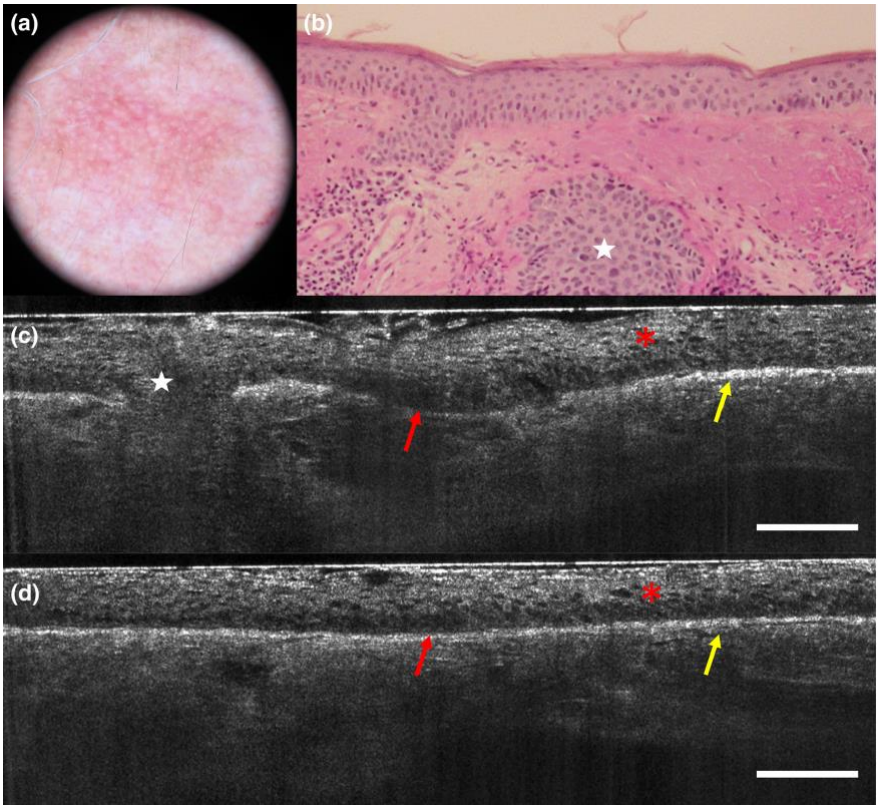

Figure 24. (a–d) Actinic keratosis: (a) dermoscopic, (b) histopathological and (c, d) LC-OCT images. (b) Histopathological examination shows mild atypia of keratinocytes in the epidermis and prominent hair follicles (white star). (c,d) LC-OCT examination reveals the presence of atypical keratinocyte nuclei within the epidermis (red asterisk) and a well-delineated dermoepidermal junction (DEJ, red arrow). (c) A hair follicle (white star) is also present. Scale bar = 100 µm.

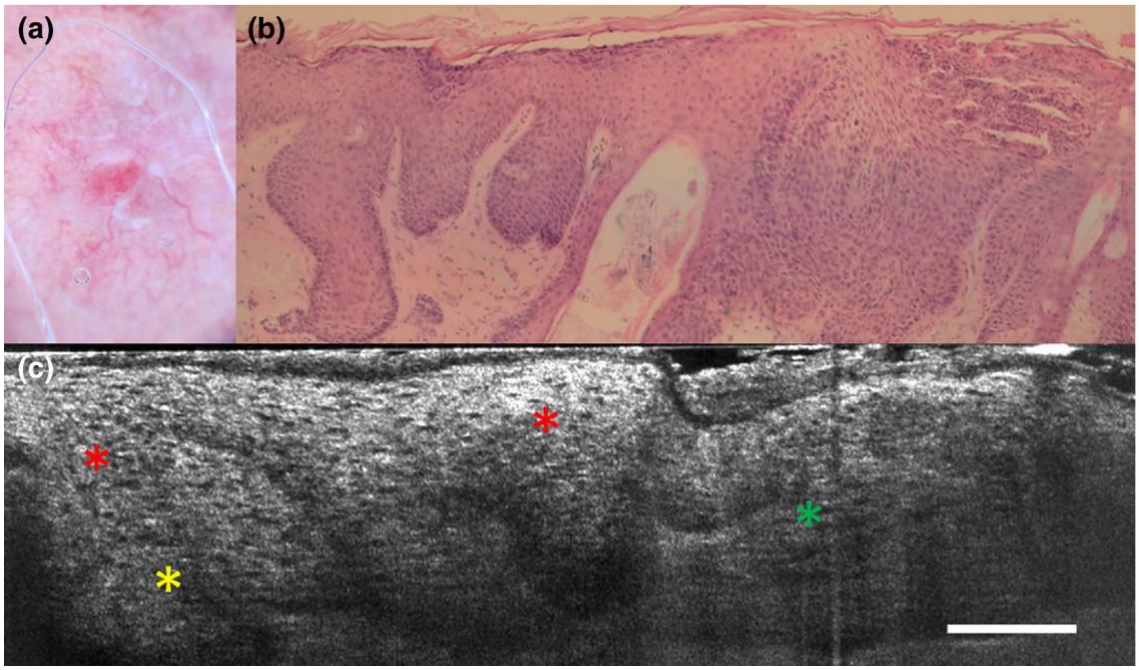

Figure 25. (a–c) Invasive squamous cell carcinoma: (a) dermoscopic, (b) histopathological, and (c) LC-OCT images. (c) LC-OCT examination reveals the presence of atypical keratinocyte nuclei of irregular size and shape within the epidermis (red asterisk). The dermoepidermal junction is not well delineated (green asterisk) and large tumor branches are visible (yellow asterisk). Scale bar = 100 µm.

1.4.4 Melanocytic lesions

The complexity of the diagnosis of melanocytic lesions is responsible for the fact that to date only few works are present in the literature on this topic.[58-60]

The description of the appearance of melanocytic lesions with LC-OCT consisted of several successive phases. As a first step, the LC-OCT counterpart of the main dermoscopic criteria used for melanocytic lesions of both benign and malignant nature was investigated (example in Figure 26).[61] LC-OCT allowed for the first time to perform an in vivo, 3-D correlation between dermoscopic criteria and pathological-like features of melanocytic lesions, allowing to discover new correlations and to confirm the ones already hypothesized with other methods of non-invasive diagnostics.

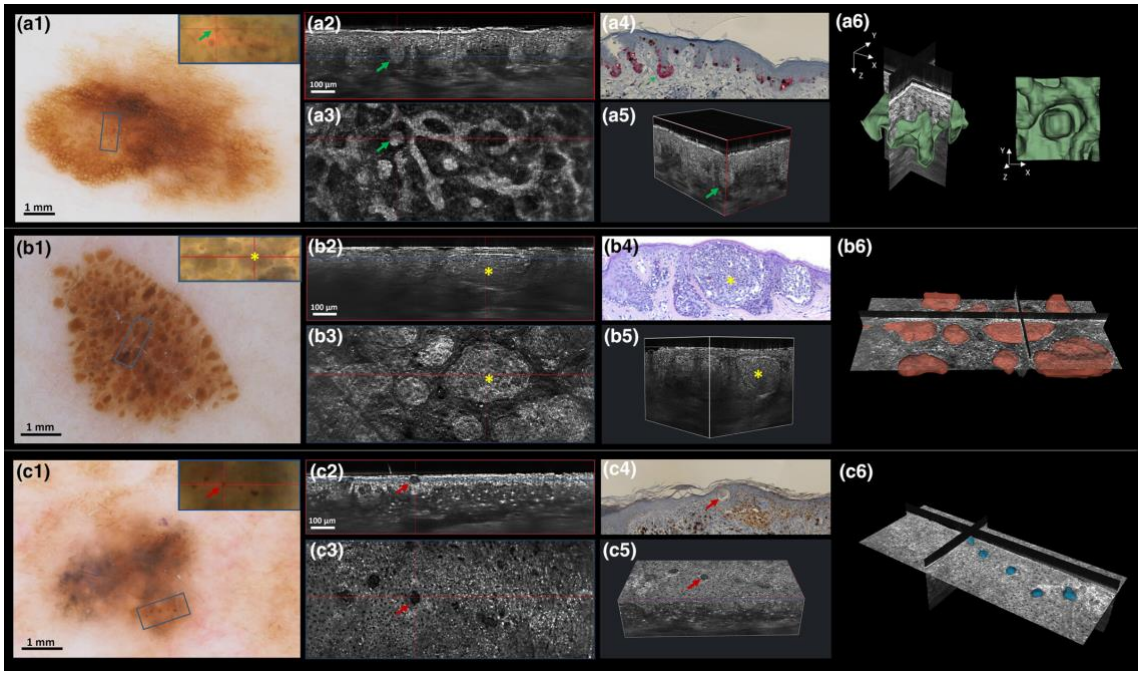

Figure 26. Brown dots and globules. They can correspond to the presence of junctional nests at the tip of the rete ridges (green arrows) (a1–a6), big nests of melanocytes close to the surface of the skin (asterisks) (b1–b6) or to roundish keratin structures (cysts/pseudocysts) in the epidermis (red arrows) (c1–c6). Dermoscopic image of a compound nevus with severe atypia (a1), compound melanocytic nevus with moderate atypia (b1) and of a melanocytic proliferation (c1). (a2–c2) Vertical and (a3–c3) horizontal images (a4–c4) histological image and (a5–c5) 3D reconstruction of the corresponding lesions. (a6–c6) 3D reconstruction with semi-automatic segmentation of the shape and distribution of the melanocytic nests and cysts/pseudocyst.

The next step was to define precise diagnostic criteria that would allow to distinguish benign from malignant melanocytic lesions.[62] A series of both architectural and cytological criteria have been recognized. In particular, the main melanoma diagnostic criteria include detecting >10 pagetoid cells in 3D acquisition, irregular 3D epidermal architecture, disrupted dermo-epidermal junction and clefting (Table 6).

Criteria	Definition
Number of pagetoid cells > 10	More than 10 atypical melanocytes of round or dendritic shape detected in epidermis per single vertical visual field
Disrupted dermo-epidermal junction	Ill-defined dermoepidermal junction due to the architectural disorder of the melanocytic nests located on dermal ridges and papillae
Clefting	Clear dark space in between the bright nucleated cells and surrounding epidermis or stroma. Nest of bright nucleated cells can become discohesive from its surrounding structures

Table 6. Definition of the main LC-OCT diagnostic criteria of melanoma

2. OBJECTIVES OF THE STUDY

Recently, performance studies based on the use of LC-OCT in the diagnosis of non-melanoma skin cancer have been made.[63]

In particular, the authors found a 3%-increase in diagnostic accuracy from dermoscopy [88% (sensitivity 90%; specificity 86%)] to LC-OCT [91% (sensitivity 98%; specificity 80%)] for BCC. Regarding SCC Cinotti et al.[63] found that LC-OCT increased the diagnostic confidence by 24.7% compared with dermoscopy alone. Similar performance studies are currently being conducted for the evaluation of melanocytic lesions, however at the moment the proposed diagnostic criteria do not seem sufficient to adequately differentiate melanoma from benign melanocytic or other diagnostic entities with uncertain prognostic significance, such as atypical melanocytic nevi and RCM is still used as the main technique for this purpose.

The use of artificial intelligence (AI) applied to dermatological diagnostics could be an effective strategy in improving the LC-OCT performance in the diagnosis of melanoma. Therefore, this study aims to elaborate an AI integrated approach, based on images made using LC-OCT, able to correctly identify dermoscopically suspicious melanocytic lesions as benign, malignant or at uncertain prognostic significance.

3. MATERIALS AND METHODS

A retrospective study was conducted to elaborate and evaluate the accuracy of an AI algorithm in distinguishing images of melanocytic lesions into three diagnostic categories: melanocytic nevi, atypical/dysplastic melanocytic nevi and melanoma.
The analyzed images consisted of vertical sections (DICOM) acquired via LC-OCT method (1200x500 µm) collected by two experienced dermatologists (SS and MV) at the dermatology department of ASST Spedali Civili di Brescia (IT) between June 2020 and September 2024.
Only lesions with an unambiguous diagnosis, clinically or histologically, were included.

LC-OCT images were acquired with a CE-marked LC-OCT device (DAMAE Medical, Paris, France) in a standardized manner. For each melanocytic lesion, multiple 3D and vertical LC-OCT acquisitions were performed in separate areas of the lesion. All acquisitions were localized manually using the instrument's built-in dermoscopic image (2.5mm field of view, 5µm resolution).

All acquisitions with poor image quality were excluded from the study.

Step I
The set of LC-OCT DICOM images was thus enriched, in order to try to increase the signal/noise ratio (SNR) with respect to the investigation outcome (Figure 27):
- no filter (RAW images)
- Gaussian filter (this is a convolution filter whose main objective is to reduce high frequency noise)

- LOG filter (Laplacian after Gaussian), is a filter that emphasizes the second derivatives, eliminating the contribution of the previous derivatives. Useful for the study of gradients, it has been widely used in radiomics in both MRI and PET investigations.
- MERGED filter, this is an unconventional filter, which consists of the average of a LOG and a Gaussian image.

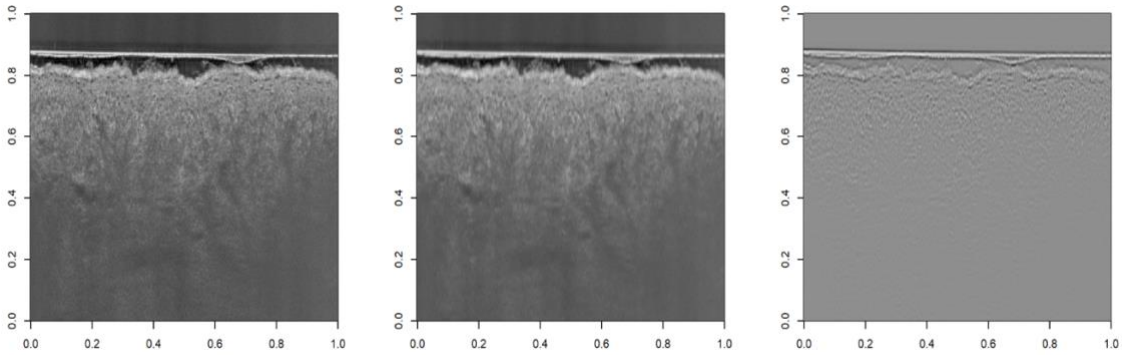

Figure 27. Example of vertical LC-OCT acquisitions in PNG, GAU and LOG format.

Step II

The images filtered with Gaussian and RAW filter were used by two experienced engineers (RG, MV) from the University of Brescia (IT) and University of Huddersfield (UK) to extract pixel clusters, according to the SLIC Superpixels and Affinity Propagation (AP) Clustering algorithm.[64] First, the SLICAP technique uses the SLIC superpixel algorithm to form an over-segmentation of an image. Then, a similarity is constructed based on the features of superpixels. Finally, the AP algorithm clusters these superpixels with the similarities obtained.

These groupings of homologous regions were then grouped again to form two regions, corresponding anatomically to the upper part and the lower/deep part of the dermis.

Step III

The masks obtained in the previous step were applied to the images of step I (RAW, GAU, LOG and MERGED) to extract regions of interest (ROI), from which pixels, image biomarkers were subsequently extracted (Figure 28).

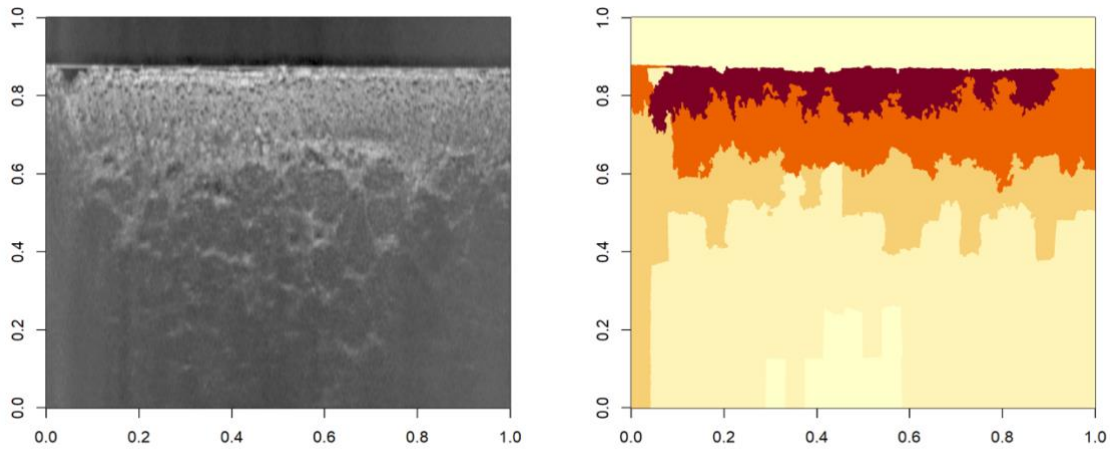

Figure 28. Example of regions of interests (ROI), highlighted by different colors, which were extracted.

Step IV

The image biomarkers were extracted with a library in R, called Moddicom,[65] image biomarker standardisation initiative (IBSI) compliant,[66-68] which extracted (based on what was previously produced) 1670 candidate biomarkers.

Step V

Several Machine Learning (ML) models were trained to understand if any biomarker was able to discern melanoma vs nevus/dysplastic nevus. In particular:

- Bivariate logistic regression: with a forward feature selection strategy, the most promising bivariate regression models were extracted.
  To limit overfitting, a 7:3 cross-fold validation was used.
- Decision Tree. A C4.5 decision tree was trained on the entire set of biomarkers and the performance on the training (and subsequently on the testing set) in terms of accuracy, NPV and PPV was obtained. Again, the probability density functions of accuracy, NPV and PPV were obtained with a 7:3 25-cross fold validation (Figure 29).

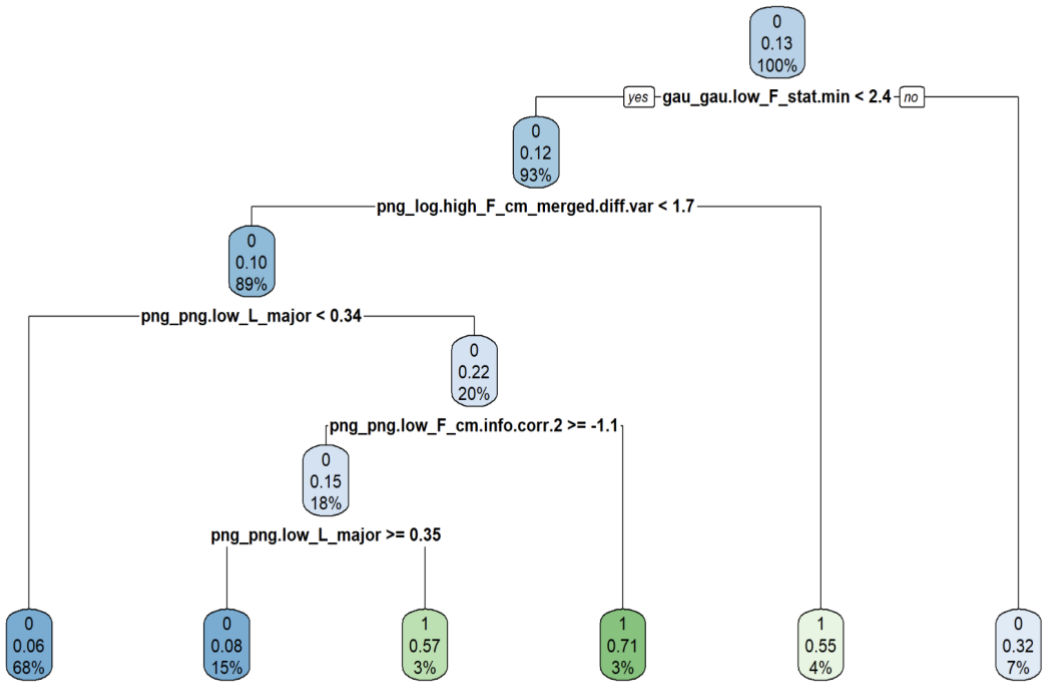

Figure 29. Example of decision tree.

- A Random Forest was then trained downstream.

A summary diagram of the analysis conducted can be found in image 30.

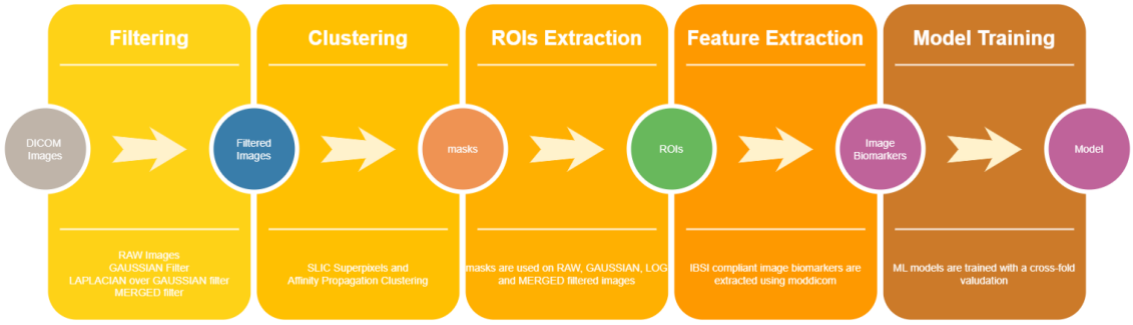

Figura 30. Diagram of the analysis conducted.

3.1 Ethical aspects

The study was conducted following the principles set out in the Declaration of Helsinki and all patients provided written informed consent.

3.2 Statistical analysis

Statistical analysis was performed using R software version 4.1.3 (R foundation for Statistical Computing, Vienna, Austria).

In order to distinguish melanoma and nevus/dysplastic nevus populations, for each of the 1670 variables extracted a univariate analysis has been made. A Mann-Whitney (MW) Kernel Densel Estimation (KDE) for each variable has been obtained. A p-value < 0.05 was considered statistically significant.

Afterwards, a bivariate logistic regression, with a forward feature selection strategy (based on p-value), was performed. Performance matrices were expressed as area under the curve (AUC) both for the training and for the testing set.

Finally, both for the decision tree and for the random forest, the performance of the variables on the training (and subsequently on the testing set) were expressed in terms of accuracy, negative (NPV) and positive (PPV) predictive value.

4. RESULTS

A total of 265 melanocytic lesions were analyzed, 152 melanocytic nevi, 78 dysplastic nevi and 35 malignant melanomas. The diagnosis of benign lesions was obtained in most cases using an excisional biopsy.

In the remaining part of the benign lesions the diagnosis was reached only through clinical-dermoscopic or via RCM evaluation, given their unequivocal characteristics.

Routine histopathological analyzes were performed for all melanomas.

The following 1670 candidate biomarkers have been extracted (Table 7):

FALSE [1] "png_png.low_F_stat.mean"	FALSE [836] "png_gau.high_F_stat.mean"
FALSE [2] "png_png.low_F_stat.var"	FALSE [837] "png_gau.high_F_stat.var"
FALSE [3] "png_png.low_F_stat.skew"	FALSE [838] "png_gau.high_F_stat.skew"
FALSE [4] "png_png.low_F_stat.kurt"	FALSE [839] "png_gau.high_F_stat.kurt"
FALSE [5] "png_png.low_F_stat.median"	FALSE [840] "png_gau.high_F_stat.median"
FALSE [6] "png_png.low_F_stat.min"	FALSE [841] "png_gau.high_F_stat.min"
FALSE [7] "png_png.low_F_stat.10thpercentile"	FALSE [842] "png_gau.high_F_stat.10thpercentile"
FALSE [8] "png_png.low_F_stat.90thpercentile"	FALSE [843] "png_gau.high_F_stat.90thpercentile"
FALSE [9] "png_png.low_F_stat.max"	FALSE [844] "png_gau.high_F_stat.max"
FALSE [10] "png_png.low_F_stat.iqr"	FALSE [845] "png_gau.high_F_stat.iqr"
FALSE [11] "png_png.low_F_stat.range"	FALSE [846] "png_gau.high_F_stat.range"
FALSE [12] "png_png.low_F_stat.mad"	FALSE [847] "png_gau.high_F_stat.mad"
FALSE [13] "png_png.low_F_stat.rmad"	FALSE [848] "png_gau.high_F_stat.rmad"
FALSE [14] "png_png.low_F_stat.energy"	FALSE [849] "png_gau.high_F_stat.energy"
FALSE [15] "png_png.low_F_stat.rms"	FALSE [850] "png_gau.high_F_stat.rms"
FALSE [16] "png_png.low_F_stat.entropy"	FALSE [851] "png_gau.high_F_stat.entropy"
FALSE [17] "png_png.low_F_stat.uniformity"	FALSE [852] "png_gau.high_F_stat.uniformity"
FALSE [18] "png_png.low_F_stat.Nic.entropy"	FALSE [853] "png_gau.high_F_stat.Nic.entropy"
FALSE [19] "png_png.low_F_stat.Nic.kurt"	FALSE [854] "png_gau.high_F_stat.Nic.kurt"
FALSE [20] "png_png.low_F_stat.Nic.Skew"	FALSE [855] "png_gau.high_F_stat.Nic.Skew"
FALSE [21] "png_png.low_F_stat.Nic.skew"	FALSE [856] "png_gau.high_F_stat.Nic.skew"
FALSE [22] "png_png.low_F_morph.surface"	FALSE [857] "png_gau.high_F_morph.surface"
FALSE [23] "png_png.low_F_morph.volume"	FALSE [858] "png_gau.high_F_morph.volume"
FALSE [24] "png_png.low_F_morph.av"	FALSE [859] "png_gau.high_F_morph.av"
FALSE [25] "png_png.low_F_morph.comp.1"	FALSE [860] "png_gau.high_F_morph.comp.1"
FALSE [26] "png_png.low_F_morph.comp.2"	FALSE [861] "png_gau.high_F_morph.comp.2"
FALSE [27] "png_png.low_F_morph.sph.dispr"	FALSE [862] "png_gau.high_F_morph.sph.dispr"
FALSE [28] "png_png.low_F_morph.sphericity"	FALSE [863] "png_gau.high_F_morph.sphericity"
FALSE [29] "png_png.low_F_morph.asphericity"	FALSE [864] "png_gau.high_F_morph.asphericity"
FALSE [30] "png_png.low_F_morph.com"	FALSE [865] "png_gau.high_F_morph.com"
FALSE [31] "png_png.low_L_major"	FALSE [866] "png_gau.high_L_major"
FALSE [32] "png_png.low_L_minor"	FALSE [867] "png_gau.high_L_minor"
FALSE [33] "png_png.low_L_least"	FALSE [868] "png_gau.high_L_least"
FALSE [34] "png_png.low_F_morph.pca.elongation"	FALSE [869] "png_gau.high_F_morph.pca.elongation"
FALSE [35] "png_png.low_F_morph.pca.flatness"	FALSE [870] "png_gau.high_F_morph.pca.flatness"
FALSE [36] "png_png.low_F_cm.joint.max"	FALSE [871] "png_gau.high_F_cm.joint.max"
FALSE [37] "png_png.low_F_cm.joint.avg"	FALSE [872] "png_gau.high_F_cm.joint.avg"

FALSE [38] "png_png.low_F_cm.joint.var"	FALSE [873] "png_gau.high_F_cm.joint.var"
FALSE [39] "png_png.low_F_cm.joint.entr"	FALSE [874] "png_gau.high_F_cm.joint.entr"
FALSE [40] "png_png.low_F_cm.diff.avg"	FALSE [875] "png_gau.high_F_cm.diff.avg"
FALSE [41] "png_png.low_F_cm.diff.var"	FALSE [876] "png_gau.high_F_cm.diff.var"
FALSE [42] "png_png.low_F_cm.diff.entr"	FALSE [877] "png_gau.high_F_cm.diff.entr"
FALSE [43] "png_png.low_F_cm.sum.avg"	FALSE [878] "png_gau.high_F_cm.sum.avg"
FALSE [44] "png_png.low_F_cm.sum.var"	FALSE [879] "png_gau.high_F_cm.sum.var"
FALSE [45] "png_png.low_F_cm.sum.entr"	FALSE [880] "png_gau.high_F_cm.sum.entr"
FALSE [46] "png_png.low_F_cm.energy"	FALSE [881] "png_gau.high_F_cm.energy"
FALSE [47] "png_png.low_F_cm.contrast"	FALSE [882] "png_gau.high_F_cm.contrast"
FALSE [48] "png_png.low_F_cm.dissimilarity"	FALSE [883] "png_gau.high_F_cm.dissimilarity"
FALSE [49] "png_png.low_F_cm.inv.diff"	FALSE [884] "png_gau.high_F_cm.inv.diff"
FALSE [50] "png_png.low_F_cm.inv.diff.norm"	FALSE [885] "png_gau.high_F_cm.inv.diff.norm"
FALSE [51] "png_png.low_F_cm.inv.diff.mom"	FALSE [886] "png_gau.high_F_cm.inv.diff.mom"
FALSE [52] "png_png.low_F_cm.inv.diff.mom.norm"	FALSE [887] "png_gau.high_F_cm.inv.diff.mom.norm"
FALSE [53] "png_png.low_F_cm.inv.var"	FALSE [888] "png_gau.high_F_cm.inv.var"
FALSE [54] "png_png.low_F_cm.corr"	FALSE [889] "png_gau.high_F_cm.corr"
FALSE [55] "png_png.low_F_cm.auto.corr"	FALSE [890] "png_gau.high_F_cm.auto.corr"
FALSE [56] "png_png.low_F_cm.clust.tend"	FALSE [891] "png_gau.high_F_cm.clust.tend"
FALSE [57] "png_png.low_F_cm.clust.shade"	FALSE [892] "png_gau.high_F_cm.clust.shade"
FALSE [58] "png_png.low_F_cm.clust.prom"	FALSE [893] "png_gau.high_F_cm.clust.prom"
FALSE [59] "png_png.low_F_cm.info.corr.1"	FALSE [894] "png_gau.high_F_cm.info.corr.1"
FALSE [60] "png_png.low_F_cm.info.corr.2"	FALSE [895] "png_gau.high_F_cm.info.corr.2"
FALSE [61] "png_png.low_F_szm.sze"	FALSE [896] "png_gau.high_F_szm.sze"
FALSE [62] "png_png.low_F_szm.lze"	FALSE [897] "png_gau.high_F_szm.lze"
FALSE [63] "png_png.low_F_szm.lgze"	FALSE [898] "png_gau.high_F_szm.lgze"
FALSE [64] "png_png.low_F_szm.hgze"	FALSE [899] "png_gau.high_F_szm.hgze"
FALSE [65] "png_png.low_F_szm.szlge"	FALSE [900] "png_gau.high_F_szm.szlge"
FALSE [66] "png_png.low_F_szm.szhge"	FALSE [901] "png_gau.high_F_szm.szhge"
FALSE [67] "png_png.low_F_szm.lzlge"	FALSE [902] "png_gau.high_F_szm.lzlge"
FALSE [68] "png_png.low_F_szm.lzhge"	FALSE [903] "png_gau.high_F_szm.lzhge"
FALSE [69] "png_png.low_F_szm.glnu"	FALSE [904] "png_gau.high_F_szm.glnu"
FALSE [70] "png_png.low_F_szm.glnu.norm"	FALSE [905] "png_gau.high_F_szm.glnu.norm"
FALSE [71] "png_png.low_F_szm.zsnu"	FALSE [906] "png_gau.high_F_szm.zsnu"
FALSE [72] "png_png.low_F_szm.zsnu.norm"	FALSE [907] "png_gau.high_F_szm.zsnu.norm"
FALSE [73] "png_png.low_F_zsm.z.perc"	FALSE [908] "png_gau.high_F_zsm.z.perc"
FALSE [74] "png_png.low_F_szm.gl.var"	FALSE [909] "png_gau.high_F_szm.gl.var"
FALSE [75] "png_png.low_F_szm.zs.var"	FALSE [910] "png_gau.high_F_szm.zs.var"
FALSE [76] "png_png.low_F_szm.z.entr"	FALSE [911] "png_gau.high_F_szm.z.entr"
FALSE [77] "png_png.low_F_cm_2.5D.joint.max"	FALSE [912] "png_gau.high_F_cm_2.5D.joint.max"
FALSE [78] "png_png.low_F_cm_2.5D.joint.avg"	FALSE [913] "png_gau.high_F_cm_2.5D.joint.avg"
FALSE [79] "png_png.low_F_cm_2.5D.joint.var"	FALSE [914] "png_gau.high_F_cm_2.5D.joint.var"
FALSE [80] "png_png.low_F_cm_2.5D.joint.entr"	FALSE [915] "png_gau.high_F_cm_2.5D.joint.entr"
FALSE [81] "png_png.low_F_cm_2.5D.diff.avg"	FALSE [916] "png_gau.high_F_cm_2.5D.diff.avg"
FALSE [82] "png_png.low_F_cm_2.5D.diff.var"	FALSE [917] "png_gau.high_F_cm_2.5D.diff.var"
FALSE [83] "png_png.low_F_cm_2.5D.diff.entr"	FALSE [918] "png_gau.high_F_cm_2.5D.diff.entr"
FALSE [84] "png_png.low_F_cm_2.5D.sum.avg"	FALSE [919] "png_gau.high_F_cm_2.5D.sum.avg"
FALSE [85] "png_png.low_F_cm_2.5D.sum.var"	FALSE [920] "png_gau.high_F_cm_2.5D.sum.var"
FALSE [86] "png_png.low_F_cm_2.5D.sum.entr"	FALSE [921] "png_gau.high_F_cm_2.5D.sum.entr"
FALSE [87] "png_png.low_F_cm_2.5D.energy"	FALSE [922] "png_gau.high_F_cm_2.5D.energy"
FALSE [88] "png_png.low_F_cm_2.5D.contrast"	FALSE [923] "png_gau.high_F_cm_2.5D.contrast"
FALSE [89] "png_png.low_F_cm_2.5D.dissimilarity"	FALSE [924] "png_gau.high_F_cm_2.5D.dissimilarity"
FALSE [90] "png_png.low_F_cm_2.5D.inv.diff"	FALSE [925] "png_gau.high_F_cm_2.5D.inv.diff"
FALSE [91] "png_png.low_F_cm_2.5D.inv.diff.norm"	FALSE [926] "png_gau.high_F_cm_2.5D.inv.diff.norm"
FALSE [92] "png_png.low_F_cm_2.5D.inv.diff.mom"	FALSE [927] "png_gau.high_F_cm_2.5D.inv.diff.mom"

FALSE [93] "png_png.low_F_cm_2.5D.inv.diff.mom.norm"	FALSE [928] "png_gau.high_F_cm_2.5D.inv.diff.mom.norm"
FALSE [94] "png_png.low_F_cm_2.5D.inv.var"	FALSE [929] "png_gau.high_F_cm_2.5D.inv.var"
FALSE [95] "png_png.low_F_cm_2.5D.corr"	FALSE [930] "png_gau.high_F_cm_2.5D.corr"
FALSE [96] "png_png.low_F_cm_2.5D.auto.corr"	FALSE [931] "png_gau.high_F_cm_2.5D.auto.corr"
FALSE [97] "png_png.low_F_cm_2.5D.clust.tend"	FALSE [932] "png_gau.high_F_cm_2.5D.clust.tend"
FALSE [98] "png_png.low_F_cm_2.5D.clust.shade"	FALSE [933] "png_gau.high_F_cm_2.5D.clust.shade"
FALSE [99] "png_png.low_F_cm_2.5D.clust.prom"	FALSE [934] "png_gau.high_F_cm_2.5D.clust.prom"
FALSE [100] "png_png.low_F_cm_2.5D.info.corr.1"	FALSE [935] "png_gau.high_F_cm_2.5D.info.corr.1"
FALSE [101] "png_png.low_F_cm_2.5D.info.corr.2"	FALSE [936] "png_gau.high_F_cm_2.5D.info.corr.2"
FALSE [102] "png_png.low_F_cm_merged.joint.max"	FALSE [937] "png_gau.high_F_cm_merged.joint.max"
FALSE [103] "png_png.low_F_cm_merged.joint.avg"	FALSE [938] "png_gau.high_F_cm_merged.joint.avg"
FALSE [104] "png_png.low_F_cm_merged.joint.var"	FALSE [939] "png_gau.high_F_cm_merged.joint.var"
FALSE [105] "png_png.low_F_cm_merged.joint.entr"	FALSE [940] "png_gau.high_F_cm_merged.joint.entr"
FALSE [106] "png_png.low_F_cm_merged.diff.avg"	FALSE [941] "png_gau.high_F_cm_merged.diff.avg"
FALSE [107] "png_png.low_F_cm_merged.diff.var"	FALSE [942] "png_gau.high_F_cm_merged.diff.var"
FALSE [108] "png_png.low_F_cm_merged.diff.entr"	FALSE [943] "png_gau.high_F_cm_merged.diff.entr"
FALSE [109] "png_png.low_F_cm_merged.sum.avg"	FALSE [944] "png_gau.high_F_cm_merged.sum.avg"
FALSE [110] "png_png.low_F_cm_merged.sum.var"	FALSE [945] "png_gau.high_F_cm_merged.sum.var"
FALSE [111] "png_png.low_F_cm_merged.sum.entr"	FALSE [946] "png_gau.high_F_cm_merged.sum.entr"
FALSE [112] "png_png.low_F_cm_merged.energy"	FALSE [947] "png_gau.high_F_cm_merged.energy"
FALSE [113] "png_png.low_F_cm_merged.contrast"	FALSE [948] "png_gau.high_F_cm_merged.contrast"
FALSE [114] "png_png.low_F_cm_merged.dissimilarity"	FALSE [949] "png_gau.high_F_cm_merged.dissimilarity"
FALSE [115] "png_png.low_F_cm_merged.inv.diff"	FALSE [950] "png_gau.high_F_cm_merged.inv.diff"
FALSE [116] "png_png.low_F_cm_merged.inv.diff.norm"	FALSE [951] "png_gau.high_F_cm_merged.inv.diff.norm"
FALSE [117] "png_png.low_F_cm_merged.inv.diff.mom"	FALSE [952] "png_gau.high_F_cm_merged.inv.diff.mom"
FALSE [118] "png_png.low_F_cm_merged.inv.diff.mom.norm"	FALSE [953] "png_gau.high_F_cm_merged.inv.diff.mom.norm"
FALSE [119] "png_png.low_F_cm_merged.inv.var"	FALSE [954] "png_gau.high_F_cm_merged.inv.var"
FALSE [120] "png_png.low_F_cm_merged.corr"	FALSE [955] "png_gau.high_F_cm_merged.corr"
FALSE [121] "png_png.low_F_cm_merged.auto.corr"	FALSE [956] "png_gau.high_F_cm_merged.auto.corr"
FALSE [122] "png_png.low_F_cm_merged.clust.tend"	FALSE [957] "png_gau.high_F_cm_merged.clust.tend"
FALSE [123] "png_png.low_F_cm_merged.clust.shade"	FALSE [958] "png_gau.high_F_cm_merged.clust.shade"
FALSE [124] "png_png.low_F_cm_merged.clust.prom"	FALSE [959] "png_gau.high_F_cm_merged.clust.prom"
FALSE [125] "png_png.low_F_cm_merged.info.corr.1"	FALSE [960] "png_gau.high_F_cm_merged.info.corr.1"
FALSE [126] "png_png.low_F_cm_merged.info.corr.2"	FALSE [961] "png_gau.high_F_cm_merged.info.corr.2"
FALSE [127] "png_png.low_F_szm_2.5D.sze"	FALSE [962] "png_gau.high_F_szm_2.5D.sze"
FALSE [128] "png_png.low_F_szm_2.5D.lze"	FALSE [963] "png_gau.high_F_szm_2.5D.lze"
FALSE [129] "png_png.low_F_szm_2.5D.lgze"	FALSE [964] "png_gau.high_F_szm_2.5D.lgze"
FALSE [130] "png_png.low_F_szm_2.5D.hgze"	FALSE [965] "png_gau.high_F_szm_2.5D.hgze"
FALSE [131] "png_png.low_F_szm_2.5D.szlge"	FALSE [966] "png_gau.high_F_szm_2.5D.szlge"
FALSE [132] "png_png.low_F_szm_2.5D.szhge"	FALSE [967] "png_gau.high_F_szm_2.5D.szhge"
FALSE [133] "png_png.low_F_szm_2.5D.lzlge"	FALSE [968] "png_gau.high_F_szm_2.5D.lzlge"
FALSE [134] "png_png.low_F_szm_2.5D.lzhge"	FALSE [969] "png_gau.high_F_szm_2.5D.lzhge"
FALSE [135] "png_png.low_F_szm_2.5D.glnu"	FALSE [970] "png_gau.high_F_szm_2.5D.glnu"
FALSE [136] "png_png.low_F_szm_2.5D.glnu.norm"	FALSE [971] "png_gau.high_F_szm_2.5D.glnu.norm"
FALSE [137] "png_png.low_F_szm_2.5D.zsnu"	FALSE [972] "png_gau.high_F_szm_2.5D.zsnu"
FALSE [138] "png_png.low_F_szm_2.5D.zsnu.norm"	FALSE [973] "png_gau.high_F_szm_2.5D.zsnu.norm"
FALSE [139] "png_png.low_F_zsm_2.5D.z.perc"	FALSE [974] "png_gau.high_F_zsm_2.5D.z.perc"
FALSE [140] "png_png.low_F_szm_2.5D.gl.var"	FALSE [975] "png_gau.high_F_szm_2.5D.gl.var"
FALSE [141] "png_png.low_F_szm_2.5D.zs.var"	FALSE [976] "png_gau.high_F_szm_2.5D.zs.var"
FALSE [142] "png_png.low_F_szm_2.5D.z.entr"	FALSE [977] "png_gau.high_F_szm_2.5D.z.entr"
FALSE [143] "png_png.low_F_cm.2.5Dmerged.joint.max"	FALSE [978] "png_gau.high_F_cm.2.5Dmerged.joint.max"
FALSE [144] "png_png.low_F_cm.2.5Dmerged.joint.avg"	FALSE [979] "png_gau.high_F_cm.2.5Dmerged.joint.avg"
FALSE [145] "png_png.low_F_cm.2.5Dmerged.joint.var"	FALSE [980] "png_gau.high_F_cm.2.5Dmerged.joint.var"
FALSE [146] "png_png.low_F_cm.2.5Dmerged.joint.entr"	FALSE [981] "png_gau.high_F_cm.2.5Dmerged.joint.entr"
FALSE [147] "png_png.low_F_cm.2.5Dmerged.diff.avg"	FALSE [982] "png_gau.high_F_cm.2.5Dmerged.diff.avg"

FALSE [148] "png_png.low_F_cm.2.5Dmerged.diff.var"	FALSE [983] "png_gau.high_F_cm.2.5Dmerged.diff.var"
FALSE [149] "png_png.low_F_cm.2.5Dmerged.diff.entr"	FALSE [984] "png_gau.high_F_cm.2.5Dmerged.diff.entr"
FALSE [150] "png_png.low_F_cm.2.5Dmerged.sum.avg"	FALSE [985] "png_gau.high_F_cm.2.5Dmerged.sum.avg"
FALSE [151] "png_png.low_F_cm.2.5Dmerged.sum.var"	FALSE [986] "png_gau.high_F_cm.2.5Dmerged.sum.var"
FALSE [152] "png_png.low_F_cm.2.5Dmerged.sum.entr"	FALSE [987] "png_gau.high_F_cm.2.5Dmerged.sum.entr"
FALSE [153] "png_png.low_F_cm.2.5Dmerged.energy"	FALSE [988] "png_gau.high_F_cm.2.5Dmerged.energy"
FALSE [154] "png_png.low_F_cm.2.5Dmerged.contrast"	FALSE [989] "png_gau.high_F_cm.2.5Dmerged.contrast"
FALSE [155] "png_png.low_F_cm.2.5Dmerged.dissimilarity"	FALSE [990] "png_gau.high_F_cm.2.5Dmerged.dissimilarity"
FALSE [156] "png_png.low_F_cm.2.5Dmerged.inv.diff"	FALSE [991] "png_gau.high_F_cm.2.5Dmerged.inv.diff"
FALSE [157] "png_png.low_F_cm.2.5Dmerged.inv.diff.norm"	FALSE [992] "png_gau.high_F_cm.2.5Dmerged.inv.diff.norm"
FALSE [158] "png_png.low_F_cm.2.5Dmerged.inv.diff.mom"	FALSE [993] "png_gau.high_F_cm.2.5Dmerged.inv.diff.mom"
FALSE [159] "png_png.low_F_cm.2.5Dmerged.inv.diff.mom.norm"	FALSE [994] "png_gau.high_F_cm.2.5Dmerged.inv.diff.mom.norm"
FALSE [160] "png_png.low_F_cm.2.5Dmerged.inv.var"	FALSE [995] "png_gau.high_F_cm.2.5Dmerged.inv.var"
FALSE [161] "png_png.low_F_cm.2.5Dmerged.corr"	FALSE [996] "png_gau.high_F_cm.2.5Dmerged.corr"
FALSE [162] "png_png.low_F_cm.2.5Dmerged.auto.corr"	FALSE [997] "png_gau.high_F_cm.2.5Dmerged.auto.corr"
FALSE [163] "png_png.low_F_cm.2.5Dmerged.clust.tend"	FALSE [998] "png_gau.high_F_cm.2.5Dmerged.clust.tend"
FALSE [164] "png_png.low_F_cm.2.5Dmerged.clust.shade"	FALSE [999] "png_gau.high_F_cm.2.5Dmerged.clust.shade"
FALSE [165] "png_png.low_F_cm.2.5Dmerged.clust.prom"	FALSE [1000] "png_gau.high_F_cm.2.5Dmerged.clust.prom"
FALSE [166] "png_png.low_F_cm.2.5Dmerged.info.corr.1"	FALSE [1001] "png_gau.high_F_cm.2.5Dmerged.info.corr.1"
FALSE [167] "png_png.low_F_cm.2.5Dmerged.info.corr.2"	FALSE [1002] "png_gau.high_F_cm.2.5Dmerged.info.corr.2"
FALSE [168] "png_png.high_F_stat.mean"	FALSE [1003] "gau_gau.low_F_stat.mean"
FALSE [169] "png_png.high_F_stat.var"	FALSE [1004] "gau_gau.low_F_stat.var"
FALSE [170] "png_png.high_F_stat.skew"	FALSE [1005] "gau_gau.low_F_stat.skew"
FALSE [171] "png_png.high_F_stat.kurt"	FALSE [1006] "gau_gau.low_F_stat.kurt"
FALSE [172] "png_png.high_F_stat.median"	FALSE [1007] "gau_gau.low_F_stat.median"
FALSE [173] "png_png.high_F_stat.min"	FALSE [1008] "gau_gau.low_F_stat.min"
FALSE [174] "png_png.high_F_stat.10thpercentile"	FALSE [1009] "gau_gau.low_F_stat.10thpercentile"
FALSE [175] "png_png.high_F_stat.90thpercentile"	FALSE [1010] "gau_gau.low_F_stat.90thpercentile"
FALSE [176] "png_png.high_F_stat.max"	FALSE [1011] "gau_gau.low_F_stat.max"
FALSE [177] "png_png.high_F_stat.iqr"	FALSE [1012] "gau_gau.low_F_stat.iqr"
FALSE [178] "png_png.high_F_stat.range"	FALSE [1013] "gau_gau.low_F_stat.range"
FALSE [179] "png_png.high_F_stat.mad"	FALSE [1014] "gau_gau.low_F_stat.mad"
FALSE [180] "png_png.high_F_stat.rmad"	FALSE [1015] "gau_gau.low_F_stat.rmad"
FALSE [181] "png_png.high_F_stat.energy"	FALSE [1016] "gau_gau.low_F_stat.energy"
FALSE [182] "png_png.high_F_stat.rms"	FALSE [1017] "gau_gau.low_F_stat.rms"
FALSE [183] "png_png.high_F_stat.entropy"	FALSE [1018] "gau_gau.low_F_stat.entropy"
FALSE [184] "png_png.high_F_stat.uniformity"	FALSE [1019] "gau_gau.low_F_stat.uniformity"
FALSE [185] "png_png.high_F_stat.Nic.entropy"	FALSE [1020] "gau_gau.low_F_stat.Nic.entropy"
FALSE [186] "png_png.high_F_stat.Nic.kurt"	FALSE [1021] "gau_gau.low_F_stat.Nic.kurt"
FALSE [187] "png_png.high_F_stat.Nic.Skew"	FALSE [1022] "gau_gau.low_F_stat.Nic.Skew"
FALSE [188] "png_png.high_F_stat.Nic.skew"	FALSE [1023] "gau_gau.low_F_stat.Nic.skew"
FALSE [189] "png_png.high_F_morph.surface"	FALSE [1024] "gau_gau.low_F_morph.surface"
FALSE [190] "png_png.high_F_morph.volume"	FALSE [1025] "gau_gau.low_F_morph.volume"
FALSE [191] "png_png.high_F_morph.av"	FALSE [1026] "gau_gau.low_F_morph.av"
FALSE [192] "png_png.high_F_morph.comp.1"	FALSE [1027] "gau_gau.low_F_morph.comp.1"
FALSE [193] "png_png.high_F_morph.comp.2"	FALSE [1028] "gau_gau.low_F_morph.comp.2"
FALSE [194] "png_png.high_F_morph.sph.dispr"	FALSE [1029] "gau_gau.low_F_morph.sph.dispr"
FALSE [195] "png_png.high_F_morph.sphericity"	FALSE [1030] "gau_gau.low_F_morph.sphericity"
FALSE [196] "png_png.high_F_morph.asphericity"	FALSE [1031] "gau_gau.low_F_morph.asphericity"
FALSE [197] "png_png.high_F_morph.com"	FALSE [1032] "gau_gau.low_F_morph.com"
FALSE [198] "png_png.high_L_major"	FALSE [1033] "gau_gau.low_L_major"
FALSE [199] "png_png.high_L_minor"	FALSE [1034] "gau_gau.low_L_minor"
FALSE [200] "png_png.high_L_least"	FALSE [1035] "gau_gau.low_L_least"
FALSE [201] "png_png.high_F_morph.pca.elongation"	FALSE [1036] "gau_gau.low_F_morph.pca.elongation"
FALSE [202] "png_png.high_F_morph.pca.flatness"	FALSE [1037] "gau_gau.low_F_morph.pca.flatness"

FALSE [203] "png_png.high_F_cm.joint.max"	FALSE [1038] "gau_gau.low_F_cm.joint.max"
FALSE [204] "png_png.high_F_cm.joint.avg"	FALSE [1039] "gau_gau.low_F_cm.joint.avg"
FALSE [205] "png_png.high_F_cm.joint.var"	FALSE [1040] "gau_gau.low_F_cm.joint.var"
FALSE [206] "png_png.high_F_cm.joint.entr"	FALSE [1041] "gau_gau.low_F_cm.joint.entr"
FALSE [207] "png_png.high_F_cm.diff.avg"	FALSE [1042] "gau_gau.low_F_cm.diff.avg"
FALSE [208] "png_png.high_F_cm.diff.var"	FALSE [1043] "gau_gau.low_F_cm.diff.var"
FALSE [209] "png_png.high_F_cm.diff.entr"	FALSE [1044] "gau_gau.low_F_cm.diff.entr"
FALSE [210] "png_png.high_F_cm.sum.avg"	FALSE [1045] "gau_gau.low_F_cm.sum.avg"
FALSE [211] "png_png.high_F_cm.sum.var"	FALSE [1046] "gau_gau.low_F_cm.sum.var"
FALSE [212] "png_png.high_F_cm.sum.entr"	FALSE [1047] "gau_gau.low_F_cm.sum.entr"
FALSE [213] "png_png.high_F_cm.energy"	FALSE [1048] "gau_gau.low_F_cm.energy"
FALSE [214] "png_png.high_F_cm.contrast"	FALSE [1049] "gau_gau.low_F_cm.contrast"
FALSE [215] "png_png.high_F_cm.dissimilarity"	FALSE [1050] "gau_gau.low_F_cm.dissimilarity"
FALSE [216] "png_png.high_F_cm.inv.diff"	FALSE [1051] "gau_gau.low_F_cm.inv.diff"
FALSE [217] "png_png.high_F_cm.inv.diff.norm"	FALSE [1052] "gau_gau.low_F_cm.inv.diff.norm"
FALSE [218] "png_png.high_F_cm.inv.diff.mom"	FALSE [1053] "gau_gau.low_F_cm.inv.diff.mom"
FALSE [219] "png_png.high_F_cm.inv.diff.mom.norm"	FALSE [1054] "gau_gau.low_F_cm.inv.diff.mom.norm"
FALSE [220] "png_png.high_F_cm.inv.var"	FALSE [1055] "gau_gau.low_F_cm.inv.var"
FALSE [221] "png_png.high_F_cm.corr"	FALSE [1056] "gau_gau.low_F_cm.corr"
FALSE [222] "png_png.high_F_cm.auto.corr"	FALSE [1057] "gau_gau.low_F_cm.auto.corr"
FALSE [223] "png_png.high_F_cm.clust.tend"	FALSE [1058] "gau_gau.low_F_cm.clust.tend"
FALSE [224] "png_png.high_F_cm.clust.shade"	FALSE [1059] "gau_gau.low_F_cm.clust.shade"
FALSE [225] "png_png.high_F_cm.clust.prom"	FALSE [1060] "gau_gau.low_F_cm.clust.prom"
FALSE [226] "png_png.high_F_cm.info.corr.1"	FALSE [1061] "gau_gau.low_F_cm.info.corr.1"
FALSE [227] "png_png.high_F_cm.info.corr.2"	FALSE [1062] "gau_gau.low_F_cm.info.corr.2"
FALSE [228] "png_png.high_F_szm.sze"	FALSE [1063] "gau_gau.low_F_szm.sze"
FALSE [229] "png_png.high_F_szm.lze"	FALSE [1064] "gau_gau.low_F_szm.lze"
FALSE [230] "png_png.high_F_szm.lgze"	FALSE [1065] "gau_gau.low_F_szm.lgze"
FALSE [231] "png_png.high_F_szm.hgze"	FALSE [1066] "gau_gau.low_F_szm.hgze"
FALSE [232] "png_png.high_F_szm.szlge"	FALSE [1067] "gau_gau.low_F_szm.szlge"
FALSE [233] "png_png.high_F_szm.szhge"	FALSE [1068] "gau_gau.low_F_szm.szhge"
FALSE [234] "png_png.high_F_szm.lzlge"	FALSE [1069] "gau_gau.low_F_szm.lzlge"
FALSE [235] "png_png.high_F_szm.lzhge"	FALSE [1070] "gau_gau.low_F_szm.lzhge"
FALSE [236] "png_png.high_F_szm.glnu"	FALSE [1071] "gau_gau.low_F_szm.glnu"
FALSE [237] "png_png.high_F_szm.glnu.norm"	FALSE [1072] "gau_gau.low_F_szm.glnu.norm"
FALSE [238] "png_png.high_F_szm.zsnu"	FALSE [1073] "gau_gau.low_F_szm.zsnu"
FALSE [239] "png_png.high_F_szm.zsnu.norm"	FALSE [1074] "gau_gau.low_F_szm.zsnu.norm"
FALSE [240] "png_png.high_F_zsm.z.perc"	FALSE [1075] "gau_gau.low_F_zsm.z.perc"
FALSE [241] "png_png.high_F_szm.gl.var"	FALSE [1076] "gau_gau.low_F_szm.gl.var"
FALSE [242] "png_png.high_F_szm.zs.var"	FALSE [1077] "gau_gau.low_F_szm.zs.var"
FALSE [243] "png_png.high_F_szm.z.entr"	FALSE [1078] "gau_gau.low_F_szm.z.entr"
FALSE [244] "png_png.high_F_cm_2.5D.joint.max"	FALSE [1079] "gau_gau.low_F_cm_2.5D.joint.max"
FALSE [245] "png_png.high_F_cm_2.5D.joint.avg"	FALSE [1080] "gau_gau.low_F_cm_2.5D.joint.avg"
FALSE [246] "png_png.high_F_cm_2.5D.joint.var"	FALSE [1081] "gau_gau.low_F_cm_2.5D.joint.var"
FALSE [247] "png_png.high_F_cm_2.5D.joint.entr"	FALSE [1082] "gau_gau.low_F_cm_2.5D.joint.entr"
FALSE [248] "png_png.high_F_cm_2.5D.diff.avg"	FALSE [1083] "gau_gau.low_F_cm_2.5D.diff.avg"
FALSE [249] "png_png.high_F_cm_2.5D.diff.var"	FALSE [1084] "gau_gau.low_F_cm_2.5D.diff.var"
FALSE [250] "png_png.high_F_cm_2.5D.diff.entr"	FALSE [1085] "gau_gau.low_F_cm_2.5D.diff.entr"
FALSE [251] "png_png.high_F_cm_2.5D.sum.avg"	FALSE [1086] "gau_gau.low_F_cm_2.5D.sum.avg"
FALSE [252] "png_png.high_F_cm_2.5D.sum.var"	FALSE [1087] "gau_gau.low_F_cm_2.5D.sum.var"
FALSE [253] "png_png.high_F_cm_2.5D.sum.entr"	FALSE [1088] "gau_gau.low_F_cm_2.5D.sum.entr"
FALSE [254] "png_png.high_F_cm_2.5D.energy"	FALSE [1089] "gau_gau.low_F_cm_2.5D.energy"
FALSE [255] "png_png.high_F_cm_2.5D.contrast"	FALSE [1090] "gau_gau.low_F_cm_2.5D.contrast"
FALSE [256] "png_png.high_F_cm_2.5D.dissimilarity"	FALSE [1091] "gau_gau.low_F_cm_2.5D.dissimilarity"
FALSE [257] "png_png.high_F_cm_2.5D.inv.diff"	FALSE [1092] "gau_gau.low_F_cm_2.5D.inv.diff"

FALSE [258] "png_png.high_F_cm_2.5D.inv.diff.norm"	FALSE [1093] "gau_gau.low_F_cm_2.5D.inv.diff.norm"
FALSE [259] "png_png.high_F_cm_2.5D.inv.diff.mom"	FALSE [1094] "gau_gau.low_F_cm_2.5D.inv.diff.mom"
FALSE [260] "png_png.high_F_cm_2.5D.inv.diff.mom.norm"	FALSE [1095] "gau_gau.low_F_cm_2.5D.inv.diff.mom.norm"
FALSE [261] "png_png.high_F_cm_2.5D.inv.var"	FALSE [1096] "gau_gau.low_F_cm_2.5D.inv.var"
FALSE [262] "png_png.high_F_cm_2.5D.corr"	FALSE [1097] "gau_gau.low_F_cm_2.5D.corr"
FALSE [263] "png_png.high_F_cm_2.5D.auto.corr"	FALSE [1098] "gau_gau.low_F_cm_2.5D.auto.corr"
FALSE [264] "png_png.high_F_cm_2.5D.clust.tend"	FALSE [1099] "gau_gau.low_F_cm_2.5D.clust.tend"
FALSE [265] "png_png.high_F_cm_2.5D.clust.shade"	FALSE [1100] "gau_gau.low_F_cm_2.5D.clust.shade"
FALSE [266] "png_png.high_F_cm_2.5D.clust.prom"	FALSE [1101] "gau_gau.low_F_cm_2.5D.clust.prom"
FALSE [267] "png_png.high_F_cm_2.5D.info.corr.1"	FALSE [1102] "gau_gau.low_F_cm_2.5D.info.corr.1"
FALSE [268] "png_png.high_F_cm_2.5D.info.corr.2"	FALSE [1103] "gau_gau.low_F_cm_2.5D.info.corr.2"
FALSE [269] "png_png.high_F_cm_merged.joint.max"	FALSE [1104] "gau_gau.low_F_cm_merged.joint.max"
FALSE [270] "png_png.high_F_cm_merged.joint.avg"	FALSE [1105] "gau_gau.low_F_cm_merged.joint.avg"
FALSE [271] "png_png.high_F_cm_merged.joint.var"	FALSE [1106] "gau_gau.low_F_cm_merged.joint.var"
FALSE [272] "png_png.high_F_cm_merged.joint.entr"	FALSE [1107] "gau_gau.low_F_cm_merged.joint.entr"
FALSE [273] "png_png.high_F_cm_merged.diff.avg"	FALSE [1108] "gau_gau.low_F_cm_merged.diff.avg"
FALSE [274] "png_png.high_F_cm_merged.diff.var"	FALSE [1109] "gau_gau.low_F_cm_merged.diff.var"
FALSE [275] "png_png.high_F_cm_merged.diff.entr"	FALSE [1110] "gau_gau.low_F_cm_merged.diff.entr"
FALSE [276] "png_png.high_F_cm_merged.sum.avg"	FALSE [1111] "gau_gau.low_F_cm_merged.sum.avg"
FALSE [277] "png_png.high_F_cm_merged.sum.var"	FALSE [1112] "gau_gau.low_F_cm_merged.sum.var"
FALSE [278] "png_png.high_F_cm_merged.sum.entr"	FALSE [1113] "gau_gau.low_F_cm_merged.sum.entr"
FALSE [279] "png_png.high_F_cm_merged.energy"	FALSE [1114] "gau_gau.low_F_cm_merged.energy"
FALSE [280] "png_png.high_F_cm_merged.contrast"	FALSE [1115] "gau_gau.low_F_cm_merged.contrast"
FALSE [281] "png_png.high_F_cm_merged.dissimilarity"	FALSE [1116] "gau_gau.low_F_cm_merged.dissimilarity"
FALSE [282] "png_png.high_F_cm_merged.inv.diff"	FALSE [1117] "gau_gau.low_F_cm_merged.inv.diff"
FALSE [283] "png_png.high_F_cm_merged.inv.diff.norm"	FALSE [1118] "gau_gau.low_F_cm_merged.inv.diff.norm"
FALSE [284] "png_png.high_F_cm_merged.inv.diff.mom"	FALSE [1119] "gau_gau.low_F_cm_merged.inv.diff.mom"
FALSE [285] "png_png.high_F_cm_merged.inv.diff.mom.norm"	FALSE [1120] "gau_gau.low_F_cm_merged.inv.diff.mom.norm"
FALSE [286] "png_png.high_F_cm_merged.inv.var"	FALSE [1121] "gau_gau.low_F_cm_merged.inv.var"
FALSE [287] "png_png.high_F_cm_merged.corr"	FALSE [1122] "gau_gau.low_F_cm_merged.corr"
FALSE [288] "png_png.high_F_cm_merged.auto.corr"	FALSE [1123] "gau_gau.low_F_cm_merged.auto.corr"
FALSE [289] "png_png.high_F_cm_merged.clust.tend"	FALSE [1124] "gau_gau.low_F_cm_merged.clust.tend"
FALSE [290] "png_png.high_F_cm_merged.clust.shade"	FALSE [1125] "gau_gau.low_F_cm_merged.clust.shade"
FALSE [291] "png_png.high_F_cm_merged.clust.prom"	FALSE [1126] "gau_gau.low_F_cm_merged.clust.prom"
FALSE [292] "png_png.high_F_cm_merged.info.corr.1"	FALSE [1127] "gau_gau.low_F_cm_merged.info.corr.1"
FALSE [293] "png_png.high_F_cm_merged.info.corr.2"	FALSE [1128] "gau_gau.low_F_cm_merged.info.corr.2"
FALSE [294] "png_png.high_F_szm_2.5D.sze"	FALSE [1129] "gau_gau.low_F_szm_2.5D.sze"
FALSE [295] "png_png.high_F_szm_2.5D.lze"	FALSE [1130] "gau_gau.low_F_szm_2.5D.lze"
FALSE [296] "png_png.high_F_szm_2.5D.lgze"	FALSE [1131] "gau_gau.low_F_szm_2.5D.lgze"
FALSE [297] "png_png.high_F_szm_2.5D.hgze"	FALSE [1132] "gau_gau.low_F_szm_2.5D.hgze"
FALSE [298] "png_png.high_F_szm_2.5D.szlge"	FALSE [1133] "gau_gau.low_F_szm_2.5D.szlge"
FALSE [299] "png_png.high_F_szm_2.5D.szhge"	FALSE [1134] "gau_gau.low_F_szm_2.5D.szhge"
FALSE [300] "png_png.high_F_szm_2.5D.lzlge"	FALSE [1135] "gau_gau.low_F_szm_2.5D.lzlge"
FALSE [301] "png_png.high_F_szm_2.5D.lzhge"	FALSE [1136] "gau_gau.low_F_szm_2.5D.lzhge"
FALSE [302] "png_png.high_F_szm_2.5D.glnu"	FALSE [1137] "gau_gau.low_F_szm_2.5D.glnu"
FALSE [303] "png_png.high_F_szm_2.5D.glnu.norm"	FALSE [1138] "gau_gau.low_F_szm_2.5D.glnu.norm"
FALSE [304] "png_png.high_F_szm_2.5D.zsnu"	FALSE [1139] "gau_gau.low_F_szm_2.5D.zsnu"
FALSE [305] "png_png.high_F_szm_2.5D.zsnu.norm"	FALSE [1140] "gau_gau.low_F_szm_2.5D.zsnu.norm"
FALSE [306] "png_png.high_F_zsm_2.5D.z.perc"	FALSE [1141] "gau_gau.low_F_zsm_2.5D.z.perc"
FALSE [307] "png_png.high_F_szm_2.5D.gl.var"	FALSE [1142] "gau_gau.low_F_szm_2.5D.gl.var"
FALSE [308] "png_png.high_F_szm_2.5D.zs.var"	FALSE [1143] "gau_gau.low_F_szm_2.5D.zs.var"
FALSE [309] "png_png.high_F_szm_2.5D.z.entr"	FALSE [1144] "gau_gau.low_F_szm_2.5D.z.entr"
FALSE [310] "png_png.high_F_cm.2.5Dmerged.joint.max"	FALSE [1145] "gau_gau.low_F_cm.2.5Dmerged.joint.max"
FALSE [311] "png_png.high_F_cm.2.5Dmerged.joint.avg"	FALSE [1146] "gau_gau.low_F_cm.2.5Dmerged.joint.avg"
FALSE [312] "png_png.high_F_cm.2.5Dmerged.joint.var"	FALSE [1147] "gau_gau.low_F_cm.2.5Dmerged.joint.var"

FALSE [313] "png_png.high_F_cm.2.5Dmerged.joint.entr"	FALSE [1148] "gau_gau.low_F_cm.2.5Dmerged.joint.entr"
FALSE [314] "png_png.high_F_cm.2.5Dmerged.diff.avg"	FALSE [1149] "gau_gau.low_F_cm.2.5Dmerged.diff.avg"
FALSE [315] "png_png.high_F_cm.2.5Dmerged.diff.var"	FALSE [1150] "gau_gau.low_F_cm.2.5Dmerged.diff.var"
FALSE [316] "png_png.high_F_cm.2.5Dmerged.diff.entr"	FALSE [1151] "gau_gau.low_F_cm.2.5Dmerged.diff.entr"
FALSE [317] "png_png.high_F_cm.2.5Dmerged.sum.avg"	FALSE [1152] "gau_gau.low_F_cm.2.5Dmerged.sum.avg"
FALSE [318] "png_png.high_F_cm.2.5Dmerged.sum.var"	FALSE [1153] "gau_gau.low_F_cm.2.5Dmerged.sum.var"
FALSE [319] "png_png.high_F_cm.2.5Dmerged.sum.entr"	FALSE [1154] "gau_gau.low_F_cm.2.5Dmerged.sum.entr"
FALSE [320] "png_png.high_F_cm.2.5Dmerged.energy"	FALSE [1155] "gau_gau.low_F_cm.2.5Dmerged.energy"
FALSE [321] "png_png.high_F_cm.2.5Dmerged.contrast"	FALSE [1156] "gau_gau.low_F_cm.2.5Dmerged.contrast"
FALSE [322] "png_png.high_F_cm.2.5Dmerged.dissimilarity"	FALSE [1157] "gau_gau.low_F_cm.2.5Dmerged.dissimilarity"
FALSE [323] "png_png.high_F_cm.2.5Dmerged.inv.diff"	FALSE [1158] "gau_gau.low_F_cm.2.5Dmerged.inv.diff"
FALSE [324] "png_png.high_F_cm.2.5Dmerged.inv.diff.norm"	FALSE [1159] "gau_gau.low_F_cm.2.5Dmerged.inv.diff.norm"
FALSE [325] "png_png.high_F_cm.2.5Dmerged.inv.diff.mom"	FALSE [1160] "gau_gau.low_F_cm.2.5Dmerged.inv.diff.mom"
FALSE [326] "png_png.high_F_cm.2.5Dmerged.inv.diff.mom.norm"	FALSE [1161] "gau_gau.low_F_cm.2.5Dmerged.inv.diff.mom.norm"
FALSE [327] "png_png.high_F_cm.2.5Dmerged.inv.var"	FALSE [1162] "gau_gau.low_F_cm.2.5Dmerged.inv.var"
FALSE [328] "png_png.high_F_cm.2.5Dmerged.corr"	FALSE [1163] "gau_gau.low_F_cm.2.5Dmerged.corr"
FALSE [329] "png_png.high_F_cm.2.5Dmerged.auto.corr"	FALSE [1164] "gau_gau.low_F_cm.2.5Dmerged.auto.corr"
FALSE [330] "png_png.high_F_cm.2.5Dmerged.clust.tend"	FALSE [1165] "gau_gau.low_F_cm.2.5Dmerged.clust.tend"
FALSE [331] "png_png.high_F_cm.2.5Dmerged.clust.shade"	FALSE [1166] "gau_gau.low_F_cm.2.5Dmerged.clust.shade"
FALSE [332] "png_png.high_F_cm.2.5Dmerged.clust.prom"	FALSE [1167] "gau_gau.low_F_cm.2.5Dmerged.clust.prom"
FALSE [333] "png_png.high_F_cm.2.5Dmerged.info.corr.1"	FALSE [1168] "gau_gau.low_F_cm.2.5Dmerged.info.corr.1"
FALSE [334] "png_png.high_F_cm.2.5Dmerged.info.corr.2"	FALSE [1169] "gau_gau.low_F_cm.2.5Dmerged.info.corr.2"
FALSE [335] "png_log.low_F_stat.mean"	FALSE [1170] "gau_gau.high_F_stat.mean"
FALSE [336] "png_log.low_F_stat.var"	FALSE [1171] "gau_gau.high_F_stat.var"
FALSE [337] "png_log.low_F_stat.skew"	FALSE [1172] "gau_gau.high_F_stat.skew"
FALSE [338] "png_log.low_F_stat.kurt"	FALSE [1173] "gau_gau.high_F_stat.kurt"
FALSE [339] "png_log.low_F_stat.median"	FALSE [1174] "gau_gau.high_F_stat.median"
FALSE [340] "png_log.low_F_stat.min"	FALSE [1175] "gau_gau.high_F_stat.min"
FALSE [341] "png_log.low_F_stat.10thpercentile"	FALSE [1176] "gau_gau.high_F_stat.10thpercentile"
FALSE [342] "png_log.low_F_stat.90thpercentile"	FALSE [1177] "gau_gau.high_F_stat.90thpercentile"
FALSE [343] "png_log.low_F_stat.max"	FALSE [1178] "gau_gau.high_F_stat.max"
FALSE [344] "png_log.low_F_stat.iqr"	FALSE [1179] "gau_gau.high_F_stat.iqr"
FALSE [345] "png_log.low_F_stat.range"	FALSE [1180] "gau_gau.high_F_stat.range"
FALSE [346] "png_log.low_F_stat.mad"	FALSE [1181] "gau_gau.high_F_stat.mad"
FALSE [347] "png_log.low_F_stat.rmad"	FALSE [1182] "gau_gau.high_F_stat.rmad"
FALSE [348] "png_log.low_F_stat.energy"	FALSE [1183] "gau_gau.high_F_stat.energy"
FALSE [349] "png_log.low_F_stat.rms"	FALSE [1184] "gau_gau.high_F_stat.rms"
FALSE [350] "png_log.low_F_stat.entropy"	FALSE [1185] "gau_gau.high_F_stat.entropy"
FALSE [351] "png_log.low_F_stat.uniformity"	FALSE [1186] "gau_gau.high_F_stat.uniformity"
FALSE [352] "png_log.low_F_stat.Nic.entropy"	FALSE [1187] "gau_gau.high_F_stat.Nic.entropy"
FALSE [353] "png_log.low_F_stat.Nic.kurt"	FALSE [1188] "gau_gau.high_F_stat.Nic.kurt"
FALSE [354] "png_log.low_F_stat.Nic.Skew"	FALSE [1189] "gau_gau.high_F_stat.Nic.Skew"
FALSE [355] "png_log.low_F_stat.Nic.skew"	FALSE [1190] "gau_gau.high_F_stat.Nic.skew"
FALSE [356] "png_log.low_F_morph.surface"	FALSE [1191] "gau_gau.high_F_morph.surface"
FALSE [357] "png_log.low_F_morph.volume"	FALSE [1192] "gau_gau.high_F_morph.volume"
FALSE [358] "png_log.low_F_morph.av"	FALSE [1193] "gau_gau.high_F_morph.av"
FALSE [359] "png_log.low_F_morph.comp.1"	FALSE [1194] "gau_gau.high_F_morph.comp.1"
FALSE [360] "png_log.low_F_morph.comp.2"	FALSE [1195] "gau_gau.high_F_morph.comp.2"
FALSE [361] "png_log.low_F_morph.sph.dispr"	FALSE [1196] "gau_gau.high_F_morph.sph.dispr"
FALSE [362] "png_log.low_F_morph.sphericity"	FALSE [1197] "gau_gau.high_F_morph.sphericity"
FALSE [363] "png_log.low_F_morph.asphericity"	FALSE [1198] "gau_gau.high_F_morph.asphericity"
FALSE [364] "png_log.low_F_morph.com"	FALSE [1199] "gau_gau.high_F_morph.com"
FALSE [365] "png_log.low_L_major"	FALSE [1200] "gau_gau.high_L_major"
FALSE [366] "png_log.low_L_minor"	FALSE [1201] "gau_gau.high_L_minor"
FALSE [367] "png_log.low_L_least"	FALSE [1202] "gau_gau.high_L_least"

FALSE [368] "png_log.low_F_morph.pca.elongation"	FALSE [1203] "gau_gau.high_F_morph.pca.elongation"
FALSE [369] "png_log.low_F_morph.pca.flatness"	FALSE [1204] "gau_gau.high_F_morph.pca.flatness"
FALSE [370] "png_log.low_F_cm.joint.max"	FALSE [1205] "gau_gau.high_F_cm.joint.max"
FALSE [371] "png_log.low_F_cm.joint.avg"	FALSE [1206] "gau_gau.high_F_cm.joint.avg"
FALSE [372] "png_log.low_F_cm.joint.var"	FALSE [1207] "gau_gau.high_F_cm.joint.var"
FALSE [373] "png_log.low_F_cm.joint.entr"	FALSE [1208] "gau_gau.high_F_cm.joint.entr"
FALSE [374] "png_log.low_F_cm.diff.avg"	FALSE [1209] "gau_gau.high_F_cm.diff.avg"
FALSE [375] "png_log.low_F_cm.diff.var"	FALSE [1210] "gau_gau.high_F_cm.diff.var"
FALSE [376] "png_log.low_F_cm.diff.entr"	FALSE [1211] "gau_gau.high_F_cm.diff.entr"
FALSE [377] "png_log.low_F_cm.sum.avg"	FALSE [1212] "gau_gau.high_F_cm.sum.avg"
FALSE [378] "png_log.low_F_cm.sum.var"	FALSE [1213] "gau_gau.high_F_cm.sum.var"
FALSE [379] "png_log.low_F_cm.sum.entr"	FALSE [1214] "gau_gau.high_F_cm.sum.entr"
FALSE [380] "png_log.low_F_cm.energy"	FALSE [1215] "gau_gau.high_F_cm.energy"
FALSE [381] "png_log.low_F_cm.contrast"	FALSE [1216] "gau_gau.high_F_cm.contrast"
FALSE [382] "png_log.low_F_cm.dissimilarity"	FALSE [1217] "gau_gau.high_F_cm.dissimilarity"
FALSE [383] "png_log.low_F_cm.inv.diff"	FALSE [1218] "gau_gau.high_F_cm.inv.diff"
FALSE [384] "png_log.low_F_cm.inv.diff.norm"	FALSE [1219] "gau_gau.high_F_cm.inv.diff.norm"
FALSE [385] "png_log.low_F_cm.inv.diff.mom"	FALSE [1220] "gau_gau.high_F_cm.inv.diff.mom"
FALSE [386] "png_log.low_F_cm.inv.diff.mom.norm"	FALSE [1221] "gau_gau.high_F_cm.inv.diff.mom.norm"
FALSE [387] "png_log.low_F_cm.inv.var"	FALSE [1222] "gau_gau.high_F_cm.inv.var"
FALSE [388] "png_log.low_F_cm.corr"	FALSE [1223] "gau_gau.high_F_cm.corr"
FALSE [389] "png_log.low_F_cm.auto.corr"	FALSE [1224] "gau_gau.high_F_cm.auto.corr"
FALSE [390] "png_log.low_F_cm.clust.tend"	FALSE [1225] "gau_gau.high_F_cm.clust.tend"
FALSE [391] "png_log.low_F_cm.clust.shade"	FALSE [1226] "gau_gau.high_F_cm.clust.shade"
FALSE [392] "png_log.low_F_cm.clust.prom"	FALSE [1227] "gau_gau.high_F_cm.clust.prom"
FALSE [393] "png_log.low_F_cm.info.corr.1"	FALSE [1228] "gau_gau.high_F_cm.info.corr.1"
FALSE [394] "png_log.low_F_cm.info.corr.2"	FALSE [1229] "gau_gau.high_F_cm.info.corr.2"
FALSE [395] "png_log.low_F_szm.sze"	FALSE [1230] "gau_gau.high_F_szm.sze"
FALSE [396] "png_log.low_F_szm.lze"	FALSE [1231] "gau_gau.high_F_szm.lze"
FALSE [397] "png_log.low_F_szm.lgze"	FALSE [1232] "gau_gau.high_F_szm.lgze"
FALSE [398] "png_log.low_F_szm.hgze"	FALSE [1233] "gau_gau.high_F_szm.hgze"
FALSE [399] "png_log.low_F_szm.szlge"	FALSE [1234] "gau_gau.high_F_szm.szlge"
FALSE [400] "png_log.low_F_szm.szhge"	FALSE [1235] "gau_gau.high_F_szm.szhge"
FALSE [401] "png_log.low_F_szm.lzlge"	FALSE [1236] "gau_gau.high_F_szm.lzlge"
FALSE [402] "png_log.low_F_szm.lzhge"	FALSE [1237] "gau_gau.high_F_szm.lzhge"
FALSE [403] "png_log.low_F_szm.glnu"	FALSE [1238] "gau_gau.high_F_szm.glnu"
FALSE [404] "png_log.low_F_szm.glnu.norm"	FALSE [1239] "gau_gau.high_F_szm.glnu.norm"
FALSE [405] "png_log.low_F_szm.zsnu"	FALSE [1240] "gau_gau.high_F_szm.zsnu"
FALSE [406] "png_log.low_F_szm.zsnu.norm"	FALSE [1241] "gau_gau.high_F_szm.zsnu.norm"
FALSE [407] "png_log.low_F_zsm.z.perc"	FALSE [1242] "gau_gau.high_F_zsm.z.perc"
FALSE [408] "png_log.low_F_szm.gl.var"	FALSE [1243] "gau_gau.high_F_szm.gl.var"
FALSE [409] "png_log.low_F_szm.zs.var"	FALSE [1244] "gau_gau.high_F_szm.zs.var"
FALSE [410] "png_log.low_F_szm.z.entr"	FALSE [1245] "gau_gau.high_F_szm.z.entr"
FALSE [411] "png_log.low_F_cm_2.5D.joint.max"	FALSE [1246] "gau_gau.high_F_cm_2.5D.joint.max"
FALSE [412] "png_log.low_F_cm_2.5D.joint.avg"	FALSE [1247] "gau_gau.high_F_cm_2.5D.joint.avg"
FALSE [413] "png_log.low_F_cm_2.5D.joint.var"	FALSE [1248] "gau_gau.high_F_cm_2.5D.joint.var"
FALSE [414] "png_log.low_F_cm_2.5D.joint.entr"	FALSE [1249] "gau_gau.high_F_cm_2.5D.joint.entr"
FALSE [415] "png_log.low_F_cm_2.5D.diff.avg"	FALSE [1250] "gau_gau.high_F_cm_2.5D.diff.avg"
FALSE [416] "png_log.low_F_cm_2.5D.diff.var"	FALSE [1251] "gau_gau.high_F_cm_2.5D.diff.var"
FALSE [417] "png_log.low_F_cm_2.5D.diff.entr"	FALSE [1252] "gau_gau.high_F_cm_2.5D.diff.entr"
FALSE [418] "png_log.low_F_cm_2.5D.sum.avg"	FALSE [1253] "gau_gau.high_F_cm_2.5D.sum.avg"
FALSE [419] "png_log.low_F_cm_2.5D.sum.var"	FALSE [1254] "gau_gau.high_F_cm_2.5D.sum.var"
FALSE [420] "png_log.low_F_cm_2.5D.sum.entr"	FALSE [1255] "gau_gau.high_F_cm_2.5D.sum.entr"
FALSE [421] "png_log.low_F_cm_2.5D.energy"	FALSE [1256] "gau_gau.high_F_cm_2.5D.energy"
FALSE [422] "png_log.low_F_cm_2.5D.contrast"	FALSE [1257] "gau_gau.high_F_cm_2.5D.contrast"

FALSE [423] "png_log.low_F_cm_2.5D.dissimilarity"	FALSE [1258] "gau_gau.high_F_cm_2.5D.dissimilarity"
FALSE [424] "png_log.low_F_cm_2.5D.inv.diff"	FALSE [1259] "gau_gau.high_F_cm_2.5D.inv.diff"
FALSE [425] "png_log.low_F_cm_2.5D.inv.diff.norm"	FALSE [1260] "gau_gau.high_F_cm_2.5D.inv.diff.norm"
FALSE [426] "png_log.low_F_cm_2.5D.inv.diff.mom"	FALSE [1261] "gau_gau.high_F_cm_2.5D.inv.diff.mom"
FALSE [427] "png_log.low_F_cm_2.5D.inv.diff.mom.norm"	FALSE [1262] "gau_gau.high_F_cm_2.5D.inv.diff.mom.norm"
FALSE [428] "png_log.low_F_cm_2.5D.inv.var"	FALSE [1263] "gau_gau.high_F_cm_2.5D.inv.var"
FALSE [429] "png_log.low_F_cm_2.5D.corr"	FALSE [1264] "gau_gau.high_F_cm_2.5D.corr"
FALSE [430] "png_log.low_F_cm_2.5D.auto.corr"	FALSE [1265] "gau_gau.high_F_cm_2.5D.auto.corr"
FALSE [431] "png_log.low_F_cm_2.5D.clust.tend"	FALSE [1266] "gau_gau.high_F_cm_2.5D.clust.tend"
FALSE [432] "png_log.low_F_cm_2.5D.clust.shade"	FALSE [1267] "gau_gau.high_F_cm_2.5D.clust.shade"
FALSE [433] "png_log.low_F_cm_2.5D.clust.prom"	FALSE [1268] "gau_gau.high_F_cm_2.5D.clust.prom"
FALSE [434] "png_log.low_F_cm_2.5D.info.corr.1"	FALSE [1269] "gau_gau.high_F_cm_2.5D.info.corr.1"
FALSE [435] "png_log.low_F_cm_2.5D.info.corr.2"	FALSE [1270] "gau_gau.high_F_cm_2.5D.info.corr.2"
FALSE [436] "png_log.low_F_cm_merged.joint.max"	FALSE [1271] "gau_gau.high_F_cm_merged.joint.max"
FALSE [437] "png_log.low_F_cm_merged.joint.avg"	FALSE [1272] "gau_gau.high_F_cm_merged.joint.avg"
FALSE [438] "png_log.low_F_cm_merged.joint.var"	FALSE [1273] "gau_gau.high_F_cm_merged.joint.var"
FALSE [439] "png_log.low_F_cm_merged.joint.entr"	FALSE [1274] "gau_gau.high_F_cm_merged.joint.entr"
FALSE [440] "png_log.low_F_cm_merged.diff.avg"	FALSE [1275] "gau_gau.high_F_cm_merged.diff.avg"
FALSE [441] "png_log.low_F_cm_merged.diff.var"	FALSE [1276] "gau_gau.high_F_cm_merged.diff.var"
FALSE [442] "png_log.low_F_cm_merged.diff.entr"	FALSE [1277] "gau_gau.high_F_cm_merged.diff.entr"
FALSE [443] "png_log.low_F_cm_merged.sum.avg"	FALSE [1278] "gau_gau.high_F_cm_merged.sum.avg"
FALSE [444] "png_log.low_F_cm_merged.sum.var"	FALSE [1279] "gau_gau.high_F_cm_merged.sum.var"
FALSE [445] "png_log.low_F_cm_merged.sum.entr"	FALSE [1280] "gau_gau.high_F_cm_merged.sum.entr"
FALSE [446] "png_log.low_F_cm_merged.energy"	FALSE [1281] "gau_gau.high_F_cm_merged.energy"
FALSE [447] "png_log.low_F_cm_merged.contrast"	FALSE [1282] "gau_gau.high_F_cm_merged.contrast"
FALSE [448] "png_log.low_F_cm_merged.dissimilarity"	FALSE [1283] "gau_gau.high_F_cm_merged.dissimilarity"
FALSE [449] "png_log.low_F_cm_merged.inv.diff"	FALSE [1284] "gau_gau.high_F_cm_merged.inv.diff"
FALSE [450] "png_log.low_F_cm_merged.inv.diff.norm"	FALSE [1285] "gau_gau.high_F_cm_merged.inv.diff.norm"
FALSE [451] "png_log.low_F_cm_merged.inv.diff.mom"	FALSE [1286] "gau_gau.high_F_cm_merged.inv.diff.mom"
FALSE [452] "png_log.low_F_cm_merged.inv.diff.mom.norm"	FALSE [1287] "gau_gau.high_F_cm_merged.inv.diff.mom.norm"
FALSE [453] "png_log.low_F_cm_merged.inv.var"	FALSE [1288] "gau_gau.high_F_cm_merged.inv.var"
FALSE [454] "png_log.low_F_cm_merged.corr"	FALSE [1289] "gau_gau.high_F_cm_merged.corr"
FALSE [455] "png_log.low_F_cm_merged.auto.corr"	FALSE [1290] "gau_gau.high_F_cm_merged.auto.corr"
FALSE [456] "png_log.low_F_cm_merged.clust.tend"	FALSE [1291] "gau_gau.high_F_cm_merged.clust.tend"
FALSE [457] "png_log.low_F_cm_merged.clust.shade"	FALSE [1292] "gau_gau.high_F_cm_merged.clust.shade"
FALSE [458] "png_log.low_F_cm_merged.clust.prom"	FALSE [1293] "gau_gau.high_F_cm_merged.clust.prom"
FALSE [459] "png_log.low_F_cm_merged.info.corr.1"	FALSE [1294] "gau_gau.high_F_cm_merged.info.corr.1"
FALSE [460] "png_log.low_F_cm_merged.info.corr.2"	FALSE [1295] "gau_gau.high_F_cm_merged.info.corr.2"
FALSE [461] "png_log.low_F_szm_2.5D.sze"	FALSE [1296] "gau_gau.high_F_szm_2.5D.sze"
FALSE [462] "png_log.low_F_szm_2.5D.lze"	FALSE [1297] "gau_gau.high_F_szm_2.5D.lze"
FALSE [463] "png_log.low_F_szm_2.5D.lgze"	FALSE [1298] "gau_gau.high_F_szm_2.5D.lgze"
FALSE [464] "png_log.low_F_szm_2.5D.hgze"	FALSE [1299] "gau_gau.high_F_szm_2.5D.hgze"
FALSE [465] "png_log.low_F_szm_2.5D.szlge"	FALSE [1300] "gau_gau.high_F_szm_2.5D.szlge"
FALSE [466] "png_log.low_F_szm_2.5D.szhge"	FALSE [1301] "gau_gau.high_F_szm_2.5D.szhge"
FALSE [467] "png_log.low_F_szm_2.5D.lzlge"	FALSE [1302] "gau_gau.high_F_szm_2.5D.lzlge"
FALSE [468] "png_log.low_F_szm_2.5D.lzhge"	FALSE [1303] "gau_gau.high_F_szm_2.5D.lzhge"
FALSE [469] "png_log.low_F_szm_2.5D.glnu"	FALSE [1304] "gau_gau.high_F_szm_2.5D.glnu"
FALSE [470] "png_log.low_F_szm_2.5D.glnu.norm"	FALSE [1305] "gau_gau.high_F_szm_2.5D.glnu.norm"
FALSE [471] "png_log.low_F_szm_2.5D.zsnu"	FALSE [1306] "gau_gau.high_F_szm_2.5D.zsnu"
FALSE [472] "png_log.low_F_szm_2.5D.zsnu.norm"	FALSE [1307] "gau_gau.high_F_szm_2.5D.zsnu.norm"
FALSE [473] "png_log.low_F_zsm_2.5D.z.perc"	FALSE [1308] "gau_gau.high_F_zsm_2.5D.z.perc"
FALSE [474] "png_log.low_F_szm_2.5D.gl.var"	FALSE [1309] "gau_gau.high_F_szm_2.5D.gl.var"
FALSE [475] "png_log.low_F_szm_2.5D.zs.var"	FALSE [1310] "gau_gau.high_F_szm_2.5D.zs.var"
FALSE [476] "png_log.low_F_szm_2.5D.z.entr"	FALSE [1311] "gau_gau.high_F_szm_2.5D.z.entr"
FALSE [477] "png_log.low_F_cm.2.5Dmerged.joint.max"	FALSE [1312] "gau_gau.high_F_cm.2.5Dmerged.joint.max"

FALSE [478] "png_log.low_F_cm.2.5Dmerged.joint.avg"	FALSE [1313] "gau_gau.high_F_cm.2.5Dmerged.joint.avg"
FALSE [479] "png_log.low_F_cm.2.5Dmerged.joint.var"	FALSE [1314] "gau_gau.high_F_cm.2.5Dmerged.joint.var"
FALSE [480] "png_log.low_F_cm.2.5Dmerged.joint.entr"	FALSE [1315] "gau_gau.high_F_cm.2.5Dmerged.joint.entr"
FALSE [481] "png_log.low_F_cm.2.5Dmerged.diff.avg"	FALSE [1316] "gau_gau.high_F_cm.2.5Dmerged.diff.avg"
FALSE [482] "png_log.low_F_cm.2.5Dmerged.diff.var"	FALSE [1317] "gau_gau.high_F_cm.2.5Dmerged.diff.var"
FALSE [483] "png_log.low_F_cm.2.5Dmerged.diff.entr"	FALSE [1318] "gau_gau.high_F_cm.2.5Dmerged.diff.entr"
FALSE [484] "png_log.low_F_cm.2.5Dmerged.sum.avg"	FALSE [1319] "gau_gau.high_F_cm.2.5Dmerged.sum.avg"
FALSE [485] "png_log.low_F_cm.2.5Dmerged.sum.var"	FALSE [1320] "gau_gau.high_F_cm.2.5Dmerged.sum.var"
FALSE [486] "png_log.low_F_cm.2.5Dmerged.sum.entr"	FALSE [1321] "gau_gau.high_F_cm.2.5Dmerged.sum.entr"
FALSE [487] "png_log.low_F_cm.2.5Dmerged.energy"	FALSE [1322] "gau_gau.high_F_cm.2.5Dmerged.energy"
FALSE [488] "png_log.low_F_cm.2.5Dmerged.contrast"	FALSE [1323] "gau_gau.high_F_cm.2.5Dmerged.contrast"
FALSE [489] "png_log.low_F_cm.2.5Dmerged.dissimilarity"	FALSE [1324] "gau_gau.high_F_cm.2.5Dmerged.dissimilarity"
FALSE [490] "png_log.low_F_cm.2.5Dmerged.inv.diff"	FALSE [1325] "gau_gau.high_F_cm.2.5Dmerged.inv.diff"
FALSE [491] "png_log.low_F_cm.2.5Dmerged.inv.diff.norm"	FALSE [1326] "gau_gau.high_F_cm.2.5Dmerged.inv.diff.norm"
FALSE [492] "png_log.low_F_cm.2.5Dmerged.inv.diff.mom"	FALSE [1327] "gau_gau.high_F_cm.2.5Dmerged.inv.diff.mom"
FALSE [493] "png_log.low_F_cm.2.5Dmerged.inv.diff.mom.norm"	FALSE [1328] "gau_gau.high_F_cm.2.5Dmerged.inv.diff.mom.norm"
FALSE [494] "png_log.low_F_cm.2.5Dmerged.inv.var"	FALSE [1329] "gau_gau.high_F_cm.2.5Dmerged.inv.var"
FALSE [495] "png_log.low_F_cm.2.5Dmerged.corr"	FALSE [1330] "gau_gau.high_F_cm.2.5Dmerged.corr"
FALSE [496] "png_log.low_F_cm.2.5Dmerged.auto.corr"	FALSE [1331] "gau_gau.high_F_cm.2.5Dmerged.auto.corr"
FALSE [497] "png_log.low_F_cm.2.5Dmerged.clust.tend"	FALSE [1332] "gau_gau.high_F_cm.2.5Dmerged.clust.tend"
FALSE [498] "png_log.low_F_cm.2.5Dmerged.clust.shade"	FALSE [1333] "gau_gau.high_F_cm.2.5Dmerged.clust.shade"
FALSE [499] "png_log.low_F_cm.2.5Dmerged.clust.prom"	FALSE [1334] "gau_gau.high_F_cm.2.5Dmerged.clust.prom"
FALSE [500] "png_log.low_F_cm.2.5Dmerged.info.corr.1"	FALSE [1335] "gau_gau.high_F_cm.2.5Dmerged.info.corr.1"
FALSE [501] "png_log.low_F_cm.2.5Dmerged.info.corr.2"	FALSE [1336] "gau_gau.high_F_cm.2.5Dmerged.info.corr.2"
FALSE [502] "png_log.high_F_stat.mean"	FALSE [1337] "gau_mer.low_F_stat.mean"
FALSE [503] "png_log.high_F_stat.var"	FALSE [1338] "gau_mer.low_F_stat.var"
FALSE [504] "png_log.high_F_stat.skew"	FALSE [1339] "gau_mer.low_F_stat.skew"
FALSE [505] "png_log.high_F_stat.kurt"	FALSE [1340] "gau_mer.low_F_stat.kurt"
FALSE [506] "png_log.high_F_stat.median"	FALSE [1341] "gau_mer.low_F_stat.median"
FALSE [507] "png_log.high_F_stat.min"	FALSE [1342] "gau_mer.low_F_stat.min"
FALSE [508] "png_log.high_F_stat.10thpercentile"	FALSE [1343] "gau_mer.low_F_stat.10thpercentile"
FALSE [509] "png_log.high_F_stat.90thpercentile"	FALSE [1344] "gau_mer.low_F_stat.90thpercentile"
FALSE [510] "png_log.high_F_stat.max"	FALSE [1345] "gau_mer.low_F_stat.max"
FALSE [511] "png_log.high_F_stat.iqr"	FALSE [1346] "gau_mer.low_F_stat.iqr"
FALSE [512] "png_log.high_F_stat.range"	FALSE [1347] "gau_mer.low_F_stat.range"
FALSE [513] "png_log.high_F_stat.mad"	FALSE [1348] "gau_mer.low_F_stat.mad"
FALSE [514] "png_log.high_F_stat.rmad"	FALSE [1349] "gau_mer.low_F_stat.rmad"
FALSE [515] "png_log.high_F_stat.energy"	FALSE [1350] "gau_mer.low_F_stat.energy"
FALSE [516] "png_log.high_F_stat.rms"	FALSE [1351] "gau_mer.low_F_stat.rms"
FALSE [517] "png_log.high_F_stat.entropy"	FALSE [1352] "gau_mer.low_F_stat.entropy"
FALSE [518] "png_log.high_F_stat.uniformity"	FALSE [1353] "gau_mer.low_F_stat.uniformity"
FALSE [519] "png_log.high_F_stat.Nic.entropy"	FALSE [1354] "gau_mer.low_F_stat.Nic.entropy"
FALSE [520] "png_log.high_F_stat.Nic.kurt"	FALSE [1355] "gau_mer.low_F_stat.Nic.kurt"
FALSE [521] "png_log.high_F_stat.Nic.Skew"	FALSE [1356] "gau_mer.low_F_stat.Nic.Skew"
FALSE [522] "png_log.high_F_stat.Nic.skew"	FALSE [1357] "gau_mer.low_F_stat.Nic.skew"
FALSE [523] "png_log.high_F_morph.surface"	FALSE [1358] "gau_mer.low_F_morph.surface"
FALSE [524] "png_log.high_F_morph.volume"	FALSE [1359] "gau_mer.low_F_morph.volume"
FALSE [525] "png_log.high_F_morph.av"	FALSE [1360] "gau_mer.low_F_morph.av"
FALSE [526] "png_log.high_F_morph.comp.1"	FALSE [1361] "gau_mer.low_F_morph.comp.1"
FALSE [527] "png_log.high_F_morph.comp.2"	FALSE [1362] "gau_mer.low_F_morph.comp.2"
FALSE [528] "png_log.high_F_morph.sph.dispr"	FALSE [1363] "gau_mer.low_F_morph.sph.dispr"
FALSE [529] "png_log.high_F_morph.sphericity"	FALSE [1364] "gau_mer.low_F_morph.sphericity"
FALSE [530] "png_log.high_F_morph.asphericity"	FALSE [1365] "gau_mer.low_F_morph.asphericity"
FALSE [531] "png_log.high_F_morph.com"	FALSE [1366] "gau_mer.low_F_morph.com"
FALSE [532] "png_log.high_L_major"	FALSE [1367] "gau_mer.low_L_major"

FALSE [533] "png_log.high_L_minor"	FALSE [1368] "gau_mer.low_L_minor"
FALSE [534] "png_log.high_L_least"	FALSE [1369] "gau_mer.low_L_least"
FALSE [535] "png_log.high_F_morph.pca.elongation"	FALSE [1370] "gau_mer.low_F_morph.pca.elongation"
FALSE [536] "png_log.high_F_morph.pca.flatness"	FALSE [1371] "gau_mer.low_F_morph.pca.flatness"
FALSE [537] "png_log.high_F_cm.joint.max"	FALSE [1372] "gau_mer.low_F_cm.joint.max"
FALSE [538] "png_log.high_F_cm.joint.avg"	FALSE [1373] "gau_mer.low_F_cm.joint.avg"
FALSE [539] "png_log.high_F_cm.joint.var"	FALSE [1374] "gau_mer.low_F_cm.joint.var"
FALSE [540] "png_log.high_F_cm.joint.entr"	FALSE [1375] "gau_mer.low_F_cm.joint.entr"
FALSE [541] "png_log.high_F_cm.diff.avg"	FALSE [1376] "gau_mer.low_F_cm.diff.avg"
FALSE [542] "png_log.high_F_cm.diff.var"	FALSE [1377] "gau_mer.low_F_cm.diff.var"
FALSE [543] "png_log.high_F_cm.diff.entr"	FALSE [1378] "gau_mer.low_F_cm.diff.entr"
FALSE [544] "png_log.high_F_cm.sum.avg"	FALSE [1379] "gau_mer.low_F_cm.sum.avg"
FALSE [545] "png_log.high_F_cm.sum.var"	FALSE [1380] "gau_mer.low_F_cm.sum.var"
FALSE [546] "png_log.high_F_cm.sum.entr"	FALSE [1381] "gau_mer.low_F_cm.sum.entr"
FALSE [547] "png_log.high_F_cm.energy"	FALSE [1382] "gau_mer.low_F_cm.energy"
FALSE [548] "png_log.high_F_cm.contrast"	FALSE [1383] "gau_mer.low_F_cm.contrast"
FALSE [549] "png_log.high_F_cm.dissimilarity"	FALSE [1384] "gau_mer.low_F_cm.dissimilarity"
FALSE [550] "png_log.high_F_cm.inv.diff"	FALSE [1385] "gau_mer.low_F_cm.inv.diff"
FALSE [551] "png_log.high_F_cm.inv.diff.norm"	FALSE [1386] "gau_mer.low_F_cm.inv.diff.norm"
FALSE [552] "png_log.high_F_cm.inv.diff.mom"	FALSE [1387] "gau_mer.low_F_cm.inv.diff.mom"
FALSE [553] "png_log.high_F_cm.inv.diff.mom.norm"	FALSE [1388] "gau_mer.low_F_cm.inv.diff.mom.norm"
FALSE [554] "png_log.high_F_cm.inv.var"	FALSE [1389] "gau_mer.low_F_cm.inv.var"
FALSE [555] "png_log.high_F_cm.corr"	FALSE [1390] "gau_mer.low_F_cm.corr"
FALSE [556] "png_log.high_F_cm.auto.corr"	FALSE [1391] "gau_mer.low_F_cm.auto.corr"
FALSE [557] "png_log.high_F_cm.clust.tend"	FALSE [1392] "gau_mer.low_F_cm.clust.tend"
FALSE [558] "png_log.high_F_cm.clust.shade"	FALSE [1393] "gau_mer.low_F_cm.clust.shade"
FALSE [559] "png_log.high_F_cm.clust.prom"	FALSE [1394] "gau_mer.low_F_cm.clust.prom"
FALSE [560] "png_log.high_F_cm.info.corr.1"	FALSE [1395] "gau_mer.low_F_cm.info.corr.1"
FALSE [561] "png_log.high_F_cm.info.corr.2"	FALSE [1396] "gau_mer.low_F_cm.info.corr.2"
FALSE [562] "png_log.high_F_szm.sze"	FALSE [1397] "gau_mer.low_F_szm.sze"
FALSE [563] "png_log.high_F_szm.lze"	FALSE [1398] "gau_mer.low_F_szm.lze"
FALSE [564] "png_log.high_F_szm.lgze"	FALSE [1399] "gau_mer.low_F_szm.lgze"
FALSE [565] "png_log.high_F_szm.hgze"	FALSE [1400] "gau_mer.low_F_szm.hgze"
FALSE [566] "png_log.high_F_szm.szlge"	FALSE [1401] "gau_mer.low_F_szm.szlge"
FALSE [567] "png_log.high_F_szm.szhge"	FALSE [1402] "gau_mer.low_F_szm.szhge"
FALSE [568] "png_log.high_F_szm.lzlge"	FALSE [1403] "gau_mer.low_F_szm.lzlge"
FALSE [569] "png_log.high_F_szm.lzhge"	FALSE [1404] "gau_mer.low_F_szm.lzhge"
FALSE [570] "png_log.high_F_szm.glnu"	FALSE [1405] "gau_mer.low_F_szm.glnu"
FALSE [571] "png_log.high_F_szm.glnu.norm"	FALSE [1406] "gau_mer.low_F_szm.glnu.norm"
FALSE [572] "png_log.high_F_szm.zsnu"	FALSE [1407] "gau_mer.low_F_szm.zsnu"
FALSE [573] "png_log.high_F_szm.zsnu.norm"	FALSE [1408] "gau_mer.low_F_szm.zsnu.norm"
FALSE [574] "png_log.high_F_zsm.z.perc"	FALSE [1409] "gau_mer.low_F_zsm.z.perc"
FALSE [575] "png_log.high_F_szm.gl.var"	FALSE [1410] "gau_mer.low_F_szm.gl.var"
FALSE [576] "png_log.high_F_szm.zs.var"	FALSE [1411] "gau_mer.low_F_szm.zs.var"
FALSE [577] "png_log.high_F_szm.z.entr"	FALSE [1412] "gau_mer.low_F_szm.z.entr"
FALSE [578] "png_log.high_F_cm_2.5D.joint.max"	FALSE [1413] "gau_mer.low_F_cm_2.5D.joint.max"
FALSE [579] "png_log.high_F_cm_2.5D.joint.avg"	FALSE [1414] "gau_mer.low_F_cm_2.5D.joint.avg"
FALSE [580] "png_log.high_F_cm_2.5D.joint.var"	FALSE [1415] "gau_mer.low_F_cm_2.5D.joint.var"
FALSE [581] "png_log.high_F_cm_2.5D.joint.entr"	FALSE [1416] "gau_mer.low_F_cm_2.5D.joint.entr"
FALSE [582] "png_log.high_F_cm_2.5D.diff.avg"	FALSE [1417] "gau_mer.low_F_cm_2.5D.diff.avg"
FALSE [583] "png_log.high_F_cm_2.5D.diff.var"	FALSE [1418] "gau_mer.low_F_cm_2.5D.diff.var"
FALSE [584] "png_log.high_F_cm_2.5D.diff.entr"	FALSE [1419] "gau_mer.low_F_cm_2.5D.diff.entr"
FALSE [585] "png_log.high_F_cm_2.5D.sum.avg"	FALSE [1420] "gau_mer.low_F_cm_2.5D.sum.avg"
FALSE [586] "png_log.high_F_cm_2.5D.sum.var"	FALSE [1421] "gau_mer.low_F_cm_2.5D.sum.var"
FALSE [587] "png_log.high_F_cm_2.5D.sum.entr"	FALSE [1422] "gau_mer.low_F_cm_2.5D.sum.entr"

FALSE [588] "png_log.high_F_cm_2.5D.energy"	FALSE [1423] "gau_mer.low_F_cm_2.5D.energy"
FALSE [589] "png_log.high_F_cm_2.5D.contrast"	FALSE [1424] "gau_mer.low_F_cm_2.5D.contrast"
FALSE [590] "png_log.high_F_cm_2.5D.dissimilarity"	FALSE [1425] "gau_mer.low_F_cm_2.5D.dissimilarity"
FALSE [591] "png_log.high_F_cm_2.5D.inv.diff"	FALSE [1426] "gau_mer.low_F_cm_2.5D.inv.diff"
FALSE [592] "png_log.high_F_cm_2.5D.inv.diff.norm"	FALSE [1427] "gau_mer.low_F_cm_2.5D.inv.diff.norm"
FALSE [593] "png_log.high_F_cm_2.5D.inv.diff.mom"	FALSE [1428] "gau_mer.low_F_cm_2.5D.inv.diff.mom"
FALSE [594] "png_log.high_F_cm_2.5D.inv.diff.mom.norm"	FALSE [1429] "gau_mer.low_F_cm_2.5D.inv.diff.mom.norm"
FALSE [595] "png_log.high_F_cm_2.5D.inv.var"	FALSE [1430] "gau_mer.low_F_cm_2.5D.inv.var"
FALSE [596] "png_log.high_F_cm_2.5D.corr"	FALSE [1431] "gau_mer.low_F_cm_2.5D.corr"
FALSE [597] "png_log.high_F_cm_2.5D.auto.corr"	FALSE [1432] "gau_mer.low_F_cm_2.5D.auto.corr"
FALSE [598] "png_log.high_F_cm_2.5D.clust.tend"	FALSE [1433] "gau_mer.low_F_cm_2.5D.clust.tend"
FALSE [599] "png_log.high_F_cm_2.5D.clust.shade"	FALSE [1434] "gau_mer.low_F_cm_2.5D.clust.shade"
FALSE [600] "png_log.high_F_cm_2.5D.clust.prom"	FALSE [1435] "gau_mer.low_F_cm_2.5D.clust.prom"
FALSE [601] "png_log.high_F_cm_2.5D.info.corr.1"	FALSE [1436] "gau_mer.low_F_cm_2.5D.info.corr.1"
FALSE [602] "png_log.high_F_cm_2.5D.info.corr.2"	FALSE [1437] "gau_mer.low_F_cm_2.5D.info.corr.2"
FALSE [603] "png_log.high_F_cm_merged.joint.max"	FALSE [1438] "gau_mer.low_F_cm_merged.joint.max"
FALSE [604] "png_log.high_F_cm_merged.joint.avg"	FALSE [1439] "gau_mer.low_F_cm_merged.joint.avg"
FALSE [605] "png_log.high_F_cm_merged.joint.var"	FALSE [1440] "gau_mer.low_F_cm_merged.joint.var"
FALSE [606] "png_log.high_F_cm_merged.joint.entr"	FALSE [1441] "gau_mer.low_F_cm_merged.joint.entr"
FALSE [607] "png_log.high_F_cm_merged.diff.avg"	FALSE [1442] "gau_mer.low_F_cm_merged.diff.avg"
FALSE [608] "png_log.high_F_cm_merged.diff.var"	FALSE [1443] "gau_mer.low_F_cm_merged.diff.var"
FALSE [609] "png_log.high_F_cm_merged.diff.entr"	FALSE [1444] "gau_mer.low_F_cm_merged.diff.entr"
FALSE [610] "png_log.high_F_cm_merged.sum.avg"	FALSE [1445] "gau_mer.low_F_cm_merged.sum.avg"
FALSE [611] "png_log.high_F_cm_merged.sum.var"	FALSE [1446] "gau_mer.low_F_cm_merged.sum.var"
FALSE [612] "png_log.high_F_cm_merged.sum.entr"	FALSE [1447] "gau_mer.low_F_cm_merged.sum.entr"
FALSE [613] "png_log.high_F_cm_merged.energy"	FALSE [1448] "gau_mer.low_F_cm_merged.energy"
FALSE [614] "png_log.high_F_cm_merged.contrast"	FALSE [1449] "gau_mer.low_F_cm_merged.contrast"
FALSE [615] "png_log.high_F_cm_merged.dissimilarity"	FALSE [1450] "gau_mer.low_F_cm_merged.dissimilarity"
FALSE [616] "png_log.high_F_cm_merged.inv.diff"	FALSE [1451] "gau_mer.low_F_cm_merged.inv.diff"
FALSE [617] "png_log.high_F_cm_merged.inv.diff.norm"	FALSE [1452] "gau_mer.low_F_cm_merged.inv.diff.norm"
FALSE [618] "png_log.high_F_cm_merged.inv.diff.mom"	FALSE [1453] "gau_mer.low_F_cm_merged.inv.diff.mom"
FALSE [619] "png_log.high_F_cm_merged.inv.diff.mom.norm"	FALSE [1454] "gau_mer.low_F_cm_merged.inv.diff.mom.norm"
FALSE [620] "png_log.high_F_cm_merged.inv.var"	FALSE [1455] "gau_mer.low_F_cm_merged.inv.var"
FALSE [621] "png_log.high_F_cm_merged.corr"	FALSE [1456] "gau_mer.low_F_cm_merged.corr"
FALSE [622] "png_log.high_F_cm_merged.auto.corr"	FALSE [1457] "gau_mer.low_F_cm_merged.auto.corr"
FALSE [623] "png_log.high_F_cm_merged.clust.tend"	FALSE [1458] "gau_mer.low_F_cm_merged.clust.tend"
FALSE [624] "png_log.high_F_cm_merged.clust.shade"	FALSE [1459] "gau_mer.low_F_cm_merged.clust.shade"
FALSE [625] "png_log.high_F_cm_merged.clust.prom"	FALSE [1460] "gau_mer.low_F_cm_merged.clust.prom"
FALSE [626] "png_log.high_F_cm_merged.info.corr.1"	FALSE [1461] "gau_mer.low_F_cm_merged.info.corr.1"
FALSE [627] "png_log.high_F_cm_merged.info.corr.2"	FALSE [1462] "gau_mer.low_F_cm_merged.info.corr.2"
FALSE [628] "png_log.high_F_szm_2.5D.sze"	FALSE [1463] "gau_mer.low_F_szm_2.5D.sze"
FALSE [629] "png_log.high_F_szm_2.5D.lze"	FALSE [1464] "gau_mer.low_F_szm_2.5D.lze"
FALSE [630] "png_log.high_F_szm_2.5D.lgze"	FALSE [1465] "gau_mer.low_F_szm_2.5D.lgze"
FALSE [631] "png_log.high_F_szm_2.5D.hgze"	FALSE [1466] "gau_mer.low_F_szm_2.5D.hgze"
FALSE [632] "png_log.high_F_szm_2.5D.szlge"	FALSE [1467] "gau_mer.low_F_szm_2.5D.szlge"
FALSE [633] "png_log.high_F_szm_2.5D.szhge"	FALSE [1468] "gau_mer.low_F_szm_2.5D.szhge"
FALSE [634] "png_log.high_F_szm_2.5D.lzlge"	FALSE [1469] "gau_mer.low_F_szm_2.5D.lzlge"
FALSE [635] "png_log.high_F_szm_2.5D.lzhge"	FALSE [1470] "gau_mer.low_F_szm_2.5D.lzhge"
FALSE [636] "png_log.high_F_szm_2.5D.glnu"	FALSE [1471] "gau_mer.low_F_szm_2.5D.glnu"
FALSE [637] "png_log.high_F_szm_2.5D.glnu.norm"	FALSE [1472] "gau_mer.low_F_szm_2.5D.glnu.norm"
FALSE [638] "png_log.high_F_szm_2.5D.zsnu"	FALSE [1473] "gau_mer.low_F_szm_2.5D.zsnu"
FALSE [639] "png_log.high_F_szm_2.5D.zsnu.norm"	FALSE [1474] "gau_mer.low_F_szm_2.5D.zsnu.norm"
FALSE [640] "png_log.high_F_zsm_2.5D.z.perc"	FALSE [1475] "gau_mer.low_F_zsm_2.5D.z.perc"
FALSE [641] "png_log.high_F_szm_2.5D.gl.var"	FALSE [1476] "gau_mer.low_F_szm_2.5D.gl.var"
FALSE [642] "png_log.high_F_szm_2.5D.zs.var"	FALSE [1477] "gau_mer.low_F_szm_2.5D.zs.var"

FALSE [643] "png_log.high_F_szm_2.5D.z.entr"	FALSE [1478] "gau_mer.low_F_szm_2.5D.z.entr"
FALSE [644] "png_log.high_F_cm.2.5Dmerged.joint.max"	FALSE [1479] "gau_mer.low_F_cm.2.5Dmerged.joint.max"
FALSE [645] "png_log.high_F_cm.2.5Dmerged.joint.avg"	FALSE [1480] "gau_mer.low_F_cm.2.5Dmerged.joint.avg"
FALSE [646] "png_log.high_F_cm.2.5Dmerged.joint.var"	FALSE [1481] "gau_mer.low_F_cm.2.5Dmerged.joint.var"
FALSE [647] "png_log.high_F_cm.2.5Dmerged.joint.entr"	FALSE [1482] "gau_mer.low_F_cm.2.5Dmerged.joint.entr"
FALSE [648] "png_log.high_F_cm.2.5Dmerged.diff.avg"	FALSE [1483] "gau_mer.low_F_cm.2.5Dmerged.diff.avg"
FALSE [649] "png_log.high_F_cm.2.5Dmerged.diff.var"	FALSE [1484] "gau_mer.low_F_cm.2.5Dmerged.diff.var"
FALSE [650] "png_log.high_F_cm.2.5Dmerged.diff.entr"	FALSE [1485] "gau_mer.low_F_cm.2.5Dmerged.diff.entr"
FALSE [651] "png_log.high_F_cm.2.5Dmerged.sum.avg"	FALSE [1486] "gau_mer.low_F_cm.2.5Dmerged.sum.avg"
FALSE [652] "png_log.high_F_cm.2.5Dmerged.sum.var"	FALSE [1487] "gau_mer.low_F_cm.2.5Dmerged.sum.var"
FALSE [653] "png_log.high_F_cm.2.5Dmerged.sum.entr"	FALSE [1488] "gau_mer.low_F_cm.2.5Dmerged.sum.entr"
FALSE [654] "png_log.high_F_cm.2.5Dmerged.energy"	FALSE [1489] "gau_mer.low_F_cm.2.5Dmerged.energy"
FALSE [655] "png_log.high_F_cm.2.5Dmerged.contrast"	FALSE [1490] "gau_mer.low_F_cm.2.5Dmerged.contrast"
FALSE [656] "png_log.high_F_cm.2.5Dmerged.dissimilarity"	FALSE [1491] "gau_mer.low_F_cm.2.5Dmerged.dissimilarity"
FALSE [657] "png_log.high_F_cm.2.5Dmerged.inv.diff"	FALSE [1492] "gau_mer.low_F_cm.2.5Dmerged.inv.diff"
FALSE [658] "png_log.high_F_cm.2.5Dmerged.inv.diff.norm"	FALSE [1493] "gau_mer.low_F_cm.2.5Dmerged.inv.diff.norm"
FALSE [659] "png_log.high_F_cm.2.5Dmerged.inv.diff.mom"	FALSE [1494] "gau_mer.low_F_cm.2.5Dmerged.inv.diff.mom"
FALSE [660] "png_log.high_F_cm.2.5Dmerged.inv.diff.mom.norm"	FALSE [1495] "gau_mer.low_F_cm.2.5Dmerged.inv.diff.mom.norm"
FALSE [661] "png_log.high_F_cm.2.5Dmerged.inv.var"	FALSE [1496] "gau_mer.low_F_cm.2.5Dmerged.inv.var"
FALSE [662] "png_log.high_F_cm.2.5Dmerged.corr"	FALSE [1497] "gau_mer.low_F_cm.2.5Dmerged.corr"
FALSE [663] "png_log.high_F_cm.2.5Dmerged.auto.corr"	FALSE [1498] "gau_mer.low_F_cm.2.5Dmerged.auto.corr"
FALSE [664] "png_log.high_F_cm.2.5Dmerged.clust.tend"	FALSE [1499] "gau_mer.low_F_cm.2.5Dmerged.clust.tend"
FALSE [665] "png_log.high_F_cm.2.5Dmerged.clust.shade"	FALSE [1500] "gau_mer.low_F_cm.2.5Dmerged.clust.shade"
FALSE [666] "png_log.high_F_cm.2.5Dmerged.clust.prom"	FALSE [1501] "gau_mer.low_F_cm.2.5Dmerged.clust.prom"
FALSE [667] "png_log.high_F_cm.2.5Dmerged.info.corr.1"	FALSE [1502] "gau_mer.low_F_cm.2.5Dmerged.info.corr.1"
FALSE [668] "png_log.high_F_cm.2.5Dmerged.info.corr.2"	FALSE [1503] "gau_mer.low_F_cm.2.5Dmerged.info.corr.2"
FALSE [669] "png_gau.low_F_stat.mean"	FALSE [1504] "gau_mer.high_F_stat.mean"
FALSE [670] "png_gau.low_F_stat.var"	FALSE [1505] "gau_mer.high_F_stat.var"
FALSE [671] "png_gau.low_F_stat.skew"	FALSE [1506] "gau_mer.high_F_stat.skew"
FALSE [672] "png_gau.low_F_stat.kurt"	FALSE [1507] "gau_mer.high_F_stat.kurt"
FALSE [673] "png_gau.low_F_stat.median"	FALSE [1508] "gau_mer.high_F_stat.median"
FALSE [674] "png_gau.low_F_stat.min"	FALSE [1509] "gau_mer.high_F_stat.min"
FALSE [675] "png_gau.low_F_stat.10thpercentile"	FALSE [1510] "gau_mer.high_F_stat.10thpercentile"
FALSE [676] "png_gau.low_F_stat.90thpercentile"	FALSE [1511] "gau_mer.high_F_stat.90thpercentile"
FALSE [677] "png_gau.low_F_stat.max"	FALSE [1512] "gau_mer.high_F_stat.max"
FALSE [678] "png_gau.low_F_stat.iqr"	FALSE [1513] "gau_mer.high_F_stat.iqr"
FALSE [679] "png_gau.low_F_stat.range"	FALSE [1514] "gau_mer.high_F_stat.range"
FALSE [680] "png_gau.low_F_stat.mad"	FALSE [1515] "gau_mer.high_F_stat.mad"
FALSE [681] "png_gau.low_F_stat.rmad"	FALSE [1516] "gau_mer.high_F_stat.rmad"
FALSE [682] "png_gau.low_F_stat.energy"	FALSE [1517] "gau_mer.high_F_stat.energy"
FALSE [683] "png_gau.low_F_stat.rms"	FALSE [1518] "gau_mer.high_F_stat.rms"
FALSE [684] "png_gau.low_F_stat.entropy"	FALSE [1519] "gau_mer.high_F_stat.entropy"
FALSE [685] "png_gau.low_F_stat.uniformity"	FALSE [1520] "gau_mer.high_F_stat.uniformity"
FALSE [686] "png_gau.low_F_stat.Nic.entropy"	FALSE [1521] "gau_mer.high_F_stat.Nic.entropy"
FALSE [687] "png_gau.low_F_stat.Nic.kurt"	FALSE [1522] "gau_mer.high_F_stat.Nic.kurt"
FALSE [688] "png_gau.low_F_stat.Nic.Skew"	FALSE [1523] "gau_mer.high_F_stat.Nic.Skew"
FALSE [689] "png_gau.low_F_stat.Nic.skew"	FALSE [1524] "gau_mer.high_F_stat.Nic.skew"
FALSE [690] "png_gau.low_F_morph.surface"	FALSE [1525] "gau_mer.high_F_morph.surface"
FALSE [691] "png_gau.low_F_morph.volume"	FALSE [1526] "gau_mer.high_F_morph.volume"
FALSE [692] "png_gau.low_F_morph.av"	FALSE [1527] "gau_mer.high_F_morph.av"
FALSE [693] "png_gau.low_F_morph.comp.1"	FALSE [1528] "gau_mer.high_F_morph.comp.1"
FALSE [694] "png_gau.low_F_morph.comp.2"	FALSE [1529] "gau_mer.high_F_morph.comp.2"
FALSE [695] "png_gau.low_F_morph.sph.dispr"	FALSE [1530] "gau_mer.high_F_morph.sph.dispr"
FALSE [696] "png_gau.low_F_morph.sphericity"	FALSE [1531] "gau_mer.high_F_morph.sphericity"
FALSE [697] "png_gau.low_F_morph.asphericity"	FALSE [1532] "gau_mer.high_F_morph.asphericity"

FALSE [698] "png_gau.low_F_morph.com"	FALSE [1533] "gau_mer.high_F_morph.com"
FALSE [699] "png_gau.low_L_major"	FALSE [1534] "gau_mer.high_L_major"
FALSE [700] "png_gau.low_L_minor"	FALSE [1535] "gau_mer.high_L_minor"
FALSE [701] "png_gau.low_L_least"	FALSE [1536] "gau_mer.high_L_least"
FALSE [702] "png_gau.low_F_morph.pca.elongation"	FALSE [1537] "gau_mer.high_F_morph.pca.elongation"
FALSE [703] "png_gau.low_F_morph.pca.flatness"	FALSE [1538] "gau_mer.high_F_morph.pca.flatness"
FALSE [704] "png_gau.low_F_cm.joint.max"	FALSE [1539] "gau_mer.high_F_cm.joint.max"
FALSE [705] "png_gau.low_F_cm.joint.avg"	FALSE [1540] "gau_mer.high_F_cm.joint.avg"
FALSE [706] "png_gau.low_F_cm.joint.var"	FALSE [1541] "gau_mer.high_F_cm.joint.var"
FALSE [707] "png_gau.low_F_cm.joint.entr"	FALSE [1542] "gau_mer.high_F_cm.joint.entr"
FALSE [708] "png_gau.low_F_cm.diff.avg"	FALSE [1543] "gau_mer.high_F_cm.diff.avg"
FALSE [709] "png_gau.low_F_cm.diff.var"	FALSE [1544] "gau_mer.high_F_cm.diff.var"
FALSE [710] "png_gau.low_F_cm.diff.entr"	FALSE [1545] "gau_mer.high_F_cm.diff.entr"
FALSE [711] "png_gau.low_F_cm.sum.avg"	FALSE [1546] "gau_mer.high_F_cm.sum.avg"
FALSE [712] "png_gau.low_F_cm.sum.var"	FALSE [1547] "gau_mer.high_F_cm.sum.var"
FALSE [713] "png_gau.low_F_cm.sum.entr"	FALSE [1548] "gau_mer.high_F_cm.sum.entr"
FALSE [714] "png_gau.low_F_cm.energy"	FALSE [1549] "gau_mer.high_F_cm.energy"
FALSE [715] "png_gau.low_F_cm.contrast"	FALSE [1550] "gau_mer.high_F_cm.contrast"
FALSE [716] "png_gau.low_F_cm.dissimilarity"	FALSE [1551] "gau_mer.high_F_cm.dissimilarity"
FALSE [717] "png_gau.low_F_cm.inv.diff"	FALSE [1552] "gau_mer.high_F_cm.inv.diff"
FALSE [718] "png_gau.low_F_cm.inv.diff.norm"	FALSE [1553] "gau_mer.high_F_cm.inv.diff.norm"
FALSE [719] "png_gau.low_F_cm.inv.diff.mom"	FALSE [1554] "gau_mer.high_F_cm.inv.diff.mom"
FALSE [720] "png_gau.low_F_cm.inv.diff.mom.norm"	FALSE [1555] "gau_mer.high_F_cm.inv.diff.mom.norm"
FALSE [721] "png_gau.low_F_cm.inv.var"	FALSE [1556] "gau_mer.high_F_cm.inv.var"
FALSE [722] "png_gau.low_F_cm.corr"	FALSE [1557] "gau_mer.high_F_cm.corr"
FALSE [723] "png_gau.low_F_cm.auto.corr"	FALSE [1558] "gau_mer.high_F_cm.auto.corr"
FALSE [724] "png_gau.low_F_cm.clust.tend"	FALSE [1559] "gau_mer.high_F_cm.clust.tend"
FALSE [725] "png_gau.low_F_cm.clust.shade"	FALSE [1560] "gau_mer.high_F_cm.clust.shade"
FALSE [726] "png_gau.low_F_cm.clust.prom"	FALSE [1561] "gau_mer.high_F_cm.clust.prom"
FALSE [727] "png_gau.low_F_cm.info.corr.1"	FALSE [1562] "gau_mer.high_F_cm.info.corr.1"
FALSE [728] "png_gau.low_F_cm.info.corr.2"	FALSE [1563] "gau_mer.high_F_cm.info.corr.2"
FALSE [729] "png_gau.low_F_szm.sze"	FALSE [1564] "gau_mer.high_F_szm.sze"
FALSE [730] "png_gau.low_F_szm.lze"	FALSE [1565] "gau_mer.high_F_szm.lze"
FALSE [731] "png_gau.low_F_szm.lgze"	FALSE [1566] "gau_mer.high_F_szm.lgze"
FALSE [732] "png_gau.low_F_szm.hgze"	FALSE [1567] "gau_mer.high_F_szm.hgze"
FALSE [733] "png_gau.low_F_szm.szlge"	FALSE [1568] "gau_mer.high_F_szm.szlge"
FALSE [734] "png_gau.low_F_szm.szhge"	FALSE [1569] "gau_mer.high_F_szm.szhge"
FALSE [735] "png_gau.low_F_szm.lzlge"	FALSE [1570] "gau_mer.high_F_szm.lzlge"
FALSE [736] "png_gau.low_F_szm.lzhge"	FALSE [1571] "gau_mer.high_F_szm.lzhge"
FALSE [737] "png_gau.low_F_szm.glnu"	FALSE [1572] "gau_mer.high_F_szm.glnu"
FALSE [738] "png_gau.low_F_szm.glnu.norm"	FALSE [1573] "gau_mer.high_F_szm.glnu.norm"
FALSE [739] "png_gau.low_F_szm.zsnu"	FALSE [1574] "gau_mer.high_F_szm.zsnu"
FALSE [740] "png_gau.low_F_szm.zsnu.norm"	FALSE [1575] "gau_mer.high_F_szm.zsnu.norm"
FALSE [741] "png_gau.low_F_zsm.z.perc"	FALSE [1576] "gau_mer.high_F_zsm.z.perc"
FALSE [742] "png_gau.low_F_szm.gl.var"	FALSE [1577] "gau_mer.high_F_szm.gl.var"
FALSE [743] "png_gau.low_F_szm.zs.var"	FALSE [1578] "gau_mer.high_F_szm.zs.var"
FALSE [744] "png_gau.low_F_szm.z.entr"	FALSE [1579] "gau_mer.high_F_szm.z.entr"
FALSE [745] "png_gau.low_F_cm_2.5D.joint.max"	FALSE [1580] "gau_mer.high_F_cm_2.5D.joint.max"
FALSE [746] "png_gau.low_F_cm_2.5D.joint.avg"	FALSE [1581] "gau_mer.high_F_cm_2.5D.joint.avg"
FALSE [747] "png_gau.low_F_cm_2.5D.joint.var"	FALSE [1582] "gau_mer.high_F_cm_2.5D.joint.var"
FALSE [748] "png_gau.low_F_cm_2.5D.joint.entr"	FALSE [1583] "gau_mer.high_F_cm_2.5D.joint.entr"
FALSE [749] "png_gau.low_F_cm_2.5D.diff.avg"	FALSE [1584] "gau_mer.high_F_cm_2.5D.diff.avg"
FALSE [750] "png_gau.low_F_cm_2.5D.diff.var"	FALSE [1585] "gau_mer.high_F_cm_2.5D.diff.var"
FALSE [751] "png_gau.low_F_cm_2.5D.diff.entr"	FALSE [1586] "gau_mer.high_F_cm_2.5D.diff.entr"
FALSE [752] "png_gau.low_F_cm_2.5D.sum.avg"	FALSE [1587] "gau_mer.high_F_cm_2.5D.sum.avg"

FALSE [753] "png_gau.low_F_cm_2.5D.sum.var"	FALSE [1588] "gau_mer.high_F_cm_2.5D.sum.var"
FALSE [754] "png_gau.low_F_cm_2.5D.sum.entr"	FALSE [1589] "gau_mer.high_F_cm_2.5D.sum.entr"
FALSE [755] "png_gau.low_F_cm_2.5D.energy"	FALSE [1590] "gau_mer.high_F_cm_2.5D.energy"
FALSE [756] "png_gau.low_F_cm_2.5D.contrast"	FALSE [1591] "gau_mer.high_F_cm_2.5D.contrast"
FALSE [757] "png_gau.low_F_cm_2.5D.dissimilarity"	FALSE [1592] "gau_mer.high_F_cm_2.5D.dissimilarity"
FALSE [758] "png_gau.low_F_cm_2.5D.inv.diff"	FALSE [1593] "gau_mer.high_F_cm_2.5D.inv.diff"
FALSE [759] "png_gau.low_F_cm_2.5D.inv.diff.norm"	FALSE [1594] "gau_mer.high_F_cm_2.5D.inv.diff.norm"
FALSE [760] "png_gau.low_F_cm_2.5D.inv.diff.mom"	FALSE [1595] "gau_mer.high_F_cm_2.5D.inv.diff.mom"
FALSE [761] "png_gau.low_F_cm_2.5D.inv.diff.mom.norm"	FALSE [1596] "gau_mer.high_F_cm_2.5D.inv.diff.mom.norm"
FALSE [762] "png_gau.low_F_cm_2.5D.inv.var"	FALSE [1597] "gau_mer.high_F_cm_2.5D.inv.var"
FALSE [763] "png_gau.low_F_cm_2.5D.corr"	FALSE [1598] "gau_mer.high_F_cm_2.5D.corr"
FALSE [764] "png_gau.low_F_cm_2.5D.auto.corr"	FALSE [1599] "gau_mer.high_F_cm_2.5D.auto.corr"
FALSE [765] "png_gau.low_F_cm_2.5D.clust.tend"	FALSE [1600] "gau_mer.high_F_cm_2.5D.clust.tend"
FALSE [766] "png_gau.low_F_cm_2.5D.clust.shade"	FALSE [1601] "gau_mer.high_F_cm_2.5D.clust.shade"
FALSE [767] "png_gau.low_F_cm_2.5D.clust.prom"	FALSE [1602] "gau_mer.high_F_cm_2.5D.clust.prom"
FALSE [768] "png_gau.low_F_cm_2.5D.info.corr.1"	FALSE [1603] "gau_mer.high_F_cm_2.5D.info.corr.1"
FALSE [769] "png_gau.low_F_cm_2.5D.info.corr.2"	FALSE [1604] "gau_mer.high_F_cm_2.5D.info.corr.2"
FALSE [770] "png_gau.low_F_cm_merged.joint.max"	FALSE [1605] "gau_mer.high_F_cm_merged.joint.max"
FALSE [771] "png_gau.low_F_cm_merged.joint.avg"	FALSE [1606] "gau_mer.high_F_cm_merged.joint.avg"
FALSE [772] "png_gau.low_F_cm_merged.joint.var"	FALSE [1607] "gau_mer.high_F_cm_merged.joint.var"
FALSE [773] "png_gau.low_F_cm_merged.joint.entr"	FALSE [1608] "gau_mer.high_F_cm_merged.joint.entr"
FALSE [774] "png_gau.low_F_cm_merged.diff.avg"	FALSE [1609] "gau_mer.high_F_cm_merged.diff.avg"
FALSE [775] "png_gau.low_F_cm_merged.diff.var"	FALSE [1610] "gau_mer.high_F_cm_merged.diff.var"
FALSE [776] "png_gau.low_F_cm_merged.diff.entr"	FALSE [1611] "gau_mer.high_F_cm_merged.diff.entr"
FALSE [777] "png_gau.low_F_cm_merged.sum.avg"	FALSE [1612] "gau_mer.high_F_cm_merged.sum.avg"
FALSE [778] "png_gau.low_F_cm_merged.sum.var"	FALSE [1613] "gau_mer.high_F_cm_merged.sum.var"
FALSE [779] "png_gau.low_F_cm_merged.sum.entr"	FALSE [1614] "gau_mer.high_F_cm_merged.sum.entr"
FALSE [780] "png_gau.low_F_cm_merged.energy"	FALSE [1615] "gau_mer.high_F_cm_merged.energy"
FALSE [781] "png_gau.low_F_cm_merged.contrast"	FALSE [1616] "gau_mer.high_F_cm_merged.contrast"
FALSE [782] "png_gau.low_F_cm_merged.dissimilarity"	FALSE [1617] "gau_mer.high_F_cm_merged.dissimilarity"
FALSE [783] "png_gau.low_F_cm_merged.inv.diff"	FALSE [1618] "gau_mer.high_F_cm_merged.inv.diff"
FALSE [784] "png_gau.low_F_cm_merged.inv.diff.norm"	FALSE [1619] "gau_mer.high_F_cm_merged.inv.diff.norm"
FALSE [785] "png_gau.low_F_cm_merged.inv.diff.mom"	FALSE [1620] "gau_mer.high_F_cm_merged.inv.diff.mom"
FALSE [786] "png_gau.low_F_cm_merged.inv.diff.mom.norm"	FALSE [1621] "gau_mer.high_F_cm_merged.inv.diff.mom.norm"
FALSE [787] "png_gau.low_F_cm_merged.inv.var"	FALSE [1622] "gau_mer.high_F_cm_merged.inv.var"
FALSE [788] "png_gau.low_F_cm_merged.corr"	FALSE [1623] "gau_mer.high_F_cm_merged.corr"
FALSE [789] "png_gau.low_F_cm_merged.auto.corr"	FALSE [1624] "gau_mer.high_F_cm_merged.auto.corr"
FALSE [790] "png_gau.low_F_cm_merged.clust.tend"	FALSE [1625] "gau_mer.high_F_cm_merged.clust.tend"
FALSE [791] "png_gau.low_F_cm_merged.clust.shade"	FALSE [1626] "gau_mer.high_F_cm_merged.clust.shade"
FALSE [792] "png_gau.low_F_cm_merged.clust.prom"	FALSE [1627] "gau_mer.high_F_cm_merged.clust.prom"
FALSE [793] "png_gau.low_F_cm_merged.info.corr.1"	FALSE [1628] "gau_mer.high_F_cm_merged.info.corr.1"
FALSE [794] "png_gau.low_F_cm_merged.info.corr.2"	FALSE [1629] "gau_mer.high_F_cm_merged.info.corr.2"
FALSE [795] "png_gau.low_F_szm_2.5D.sze"	FALSE [1630] "gau_mer.high_F_szm_2.5D.sze"
FALSE [796] "png_gau.low_F_szm_2.5D.lze"	FALSE [1631] "gau_mer.high_F_szm_2.5D.lze"
FALSE [797] "png_gau.low_F_szm_2.5D.lgze"	FALSE [1632] "gau_mer.high_F_szm_2.5D.lgze"
FALSE [798] "png_gau.low_F_szm_2.5D.hgze"	FALSE [1633] "gau_mer.high_F_szm_2.5D.hgze"
FALSE [799] "png_gau.low_F_szm_2.5D.szlge"	FALSE [1634] "gau_mer.high_F_szm_2.5D.szlge"
FALSE [800] "png_gau.low_F_szm_2.5D.szhge"	FALSE [1635] "gau_mer.high_F_szm_2.5D.szhge"
FALSE [801] "png_gau.low_F_szm_2.5D.lzlge"	FALSE [1636] "gau_mer.high_F_szm_2.5D.lzlge"
FALSE [802] "png_gau.low_F_szm_2.5D.lzhge"	FALSE [1637] "gau_mer.high_F_szm_2.5D.lzhge"
FALSE [803] "png_gau.low_F_szm_2.5D.glnu"	FALSE [1638] "gau_mer.high_F_szm_2.5D.glnu"
FALSE [804] "png_gau.low_F_szm_2.5D.glnu.norm"	FALSE [1639] "gau_mer.high_F_szm_2.5D.glnu.norm"
FALSE [805] "png_gau.low_F_szm_2.5D.zsnu"	FALSE [1640] "gau_mer.high_F_szm_2.5D.zsnu"
FALSE [806] "png_gau.low_F_szm_2.5D.zsnu.norm"	FALSE [1641] "gau_mer.high_F_szm_2.5D.zsnu.norm"
FALSE [807] "png_gau.low_F_zsm_2.5D.z.perc"	FALSE [1642] "gau_mer.high_F_zsm_2.5D.z.perc"

FALSE [808] "png_gau.low_F_szm_2.5D.gl.var"	FALSE [1643] "gau_mer.high_F_szm_2.5D.gl.var"
FALSE [809] "png_gau.low_F_szm_2.5D.zs.var"	FALSE [1644] "gau_mer.high_F_szm_2.5D.zs.var"
FALSE [810] "png_gau.low_F_szm_2.5D.z.entr"	FALSE [1645] "gau_mer.high_F_szm_2.5D.z.entr"
FALSE [811] "png_gau.low_F_cm.2.5Dmerged.joint.max"	FALSE [1646] "gau_mer.high_F_cm.2.5Dmerged.joint.max"
FALSE [812] "png_gau.low_F_cm.2.5Dmerged.joint.avg"	FALSE [1647] "gau_mer.high_F_cm.2.5Dmerged.joint.avg"
FALSE [813] "png_gau.low_F_cm.2.5Dmerged.joint.var"	FALSE [1648] "gau_mer.high_F_cm.2.5Dmerged.joint.var"
FALSE [814] "png_gau.low_F_cm.2.5Dmerged.joint.entr"	FALSE [1649] "gau_mer.high_F_cm.2.5Dmerged.joint.entr"
FALSE [815] "png_gau.low_F_cm.2.5Dmerged.diff.avg"	FALSE [1650] "gau_mer.high_F_cm.2.5Dmerged.diff.avg"
FALSE [816] "png_gau.low_F_cm.2.5Dmerged.diff.var"	FALSE [1651] "gau_mer.high_F_cm.2.5Dmerged.diff.var"
FALSE [817] "png_gau.low_F_cm.2.5Dmerged.diff.entr"	FALSE [1652] "gau_mer.high_F_cm.2.5Dmerged.diff.entr"
FALSE [818] "png_gau.low_F_cm.2.5Dmerged.sum.avg"	FALSE [1653] "gau_mer.high_F_cm.2.5Dmerged.sum.avg"
FALSE [819] "png_gau.low_F_cm.2.5Dmerged.sum.var"	FALSE [1654] "gau_mer.high_F_cm.2.5Dmerged.sum.var"
FALSE [820] "png_gau.low_F_cm.2.5Dmerged.sum.entr"	FALSE [1655] "gau_mer.high_F_cm.2.5Dmerged.sum.entr"
FALSE [821] "png_gau.low_F_cm.2.5Dmerged.energy"	FALSE [1656] "gau_mer.high_F_cm.2.5Dmerged.energy"
FALSE [822] "png_gau.low_F_cm.2.5Dmerged.contrast"	FALSE [1657] "gau_mer.high_F_cm.2.5Dmerged.contrast"
FALSE [823] "png_gau.low_F_cm.2.5Dmerged.dissimilarity"	FALSE [1658] "gau_mer.high_F_cm.2.5Dmerged.dissimilarity"
FALSE [824] "png_gau.low_F_cm.2.5Dmerged.inv.diff"	FALSE [1659] "gau_mer.high_F_cm.2.5Dmerged.inv.diff"
FALSE [825] "png_gau.low_F_cm.2.5Dmerged.inv.diff.norm"	FALSE [1660] "gau_mer.high_F_cm.2.5Dmerged.inv.diff.norm"
FALSE [826] "png_gau.low_F_cm.2.5Dmerged.inv.diff.mom"	FALSE [1661] "gau_mer.high_F_cm.2.5Dmerged.inv.diff.mom"
FALSE [827] "png_gau.low_F_cm.2.5Dmerged.inv.diff.mom.norm"	FALSE [1662] "gau_mer.high_F_cm.2.5Dmerged.inv.diff.mom.norm"
FALSE [828] "png_gau.low_F_cm.2.5Dmerged.inv.var"	FALSE [1663] "gau_mer.high_F_cm.2.5Dmerged.inv.var"
FALSE [829] "png_gau.low_F_cm.2.5Dmerged.corr"	FALSE [1664] "gau_mer.high_F_cm.2.5Dmerged.corr"
FALSE [830] "png_gau.low_F_cm.2.5Dmerged.auto.corr"	FALSE [1665] "gau_mer.high_F_cm.2.5Dmerged.auto.corr"
FALSE [831] "png_gau.low_F_cm.2.5Dmerged.clust.tend"	FALSE [1666] "gau_mer.high_F_cm.2.5Dmerged.clust.tend"
FALSE [832] "png_gau.low_F_cm.2.5Dmerged.clust.shade"	FALSE [1667] "gau_mer.high_F_cm.2.5Dmerged.clust.shade"
FALSE [833] "png_gau.low_F_cm.2.5Dmerged.clust.prom"	FALSE [1668] "gau_mer.high_F_cm.2.5Dmerged.clust.prom"
FALSE [834] "png_gau.low_F_cm.2.5Dmerged.info.corr.1"	FALSE [1669] "gau_mer.high_F_cm.2.5Dmerged.info.corr.1"
FALSE [835] "png_gau.low_F_cm.2.5Dmerged.info.corr.2"	FALSE [1670] "gau_mer.high_F_cm.2.5Dmerged.info.corr.2"

Table 7. Candidate biomarkers extracted.

Png_png : window from PNG image, extracted from cluster built on unfiltered image

Png_gau : window from PNG image, extracted from cluster built on Gaussian filter

Png_log : window from PNG image, extracted from cluster built on LOG (Laplacian of Gaussian) filter

Gau_gau : window from Gaussian image, extracted from cluster built on Gaussian filter

Gau_mer : window from Gaussian image, extracted from cluster built on merged LOG/Gaussian filter.

127 variables showed a statistically significant p-value on univariate testing:

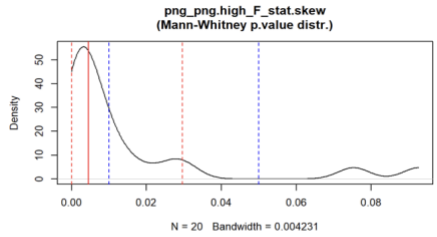
png_png.high_F_stat.skew
(Mann-Whitney p.value distr.)
Density
N = 20 Bandwidth = 0.004231

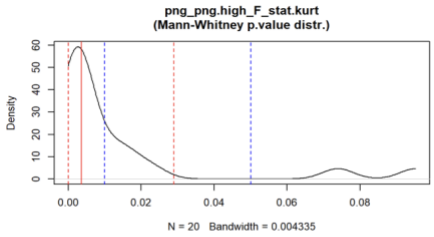
png_png.high_F_stat.kurt
(Mann-Whitney p.value distr.)
Density
N = 20 Bandwidth = 0.004335

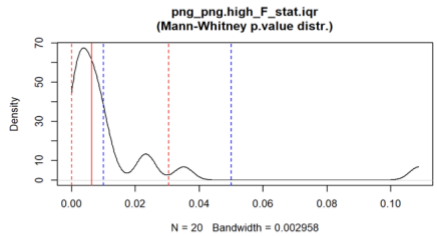
png_png.high_F_stat.iqr
(Mann-Whitney p.value distr.)
Density
N = 20 Bandwidth = 0.002958

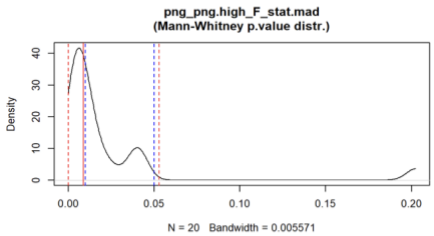
png_png.high_F_stat.mad
(Mann-Whitney p.value distr.)
Density
N = 20 Bandwidth = 0.005571

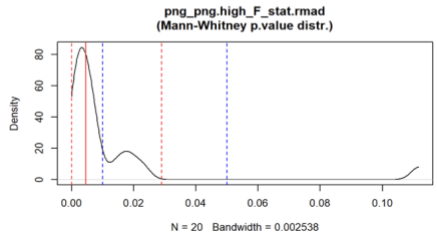
png_png.high_F_stat.rmad
(Mann-Whitney p.value distr.)
Density
N = 20 Bandwidth = 0.002538

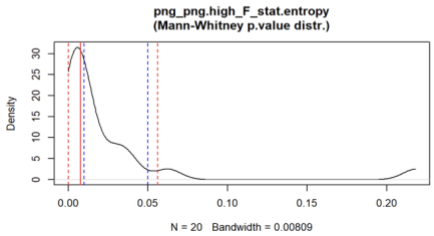
png_png.high_F_stat.entropy
(Mann-Whitney p.value distr.)
Density
N = 20 Bandwidth = 0.00809

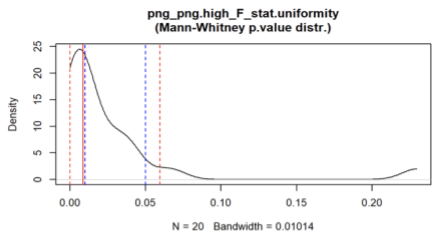
png_png.high_F_stat.uniformity
(Mann-Whitney p.value distr.)
Density
N = 20 Bandwidth = 0.01014

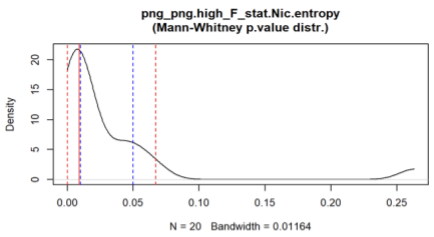
png_png.high_F_stat.Nic.entropy
(Mann-Whitney p.value distr.)
Density
N = 20 Bandwidth = 0.01164

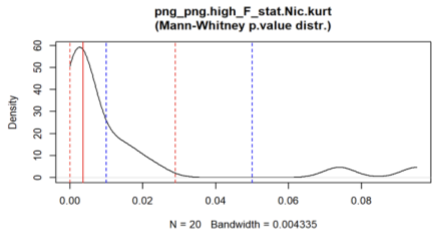
png_png.high_F_stat.Nic.kurt
(Mann-Whitney p.value distr.)
Density
N = 20 Bandwidth = 0.004335

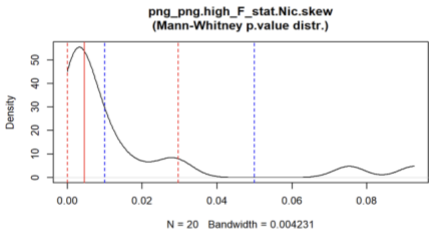
png_png.high_F_stat.Nic.skew
(Mann-Whitney p.value distr.)
Density
N = 20 Bandwidth = 0.004231

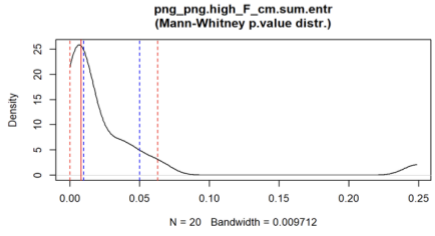
png_png.high_F_cm.sum.entr
(Mann-Whitney p.value distr.)
Density
N = 20 Bandwidth = 0.009712

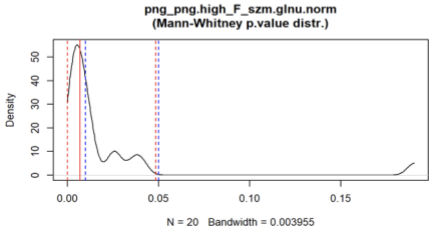
png_png.high_F_szm.glnu.norm
(Mann-Whitney p.value distr.)
Density
N = 20 Bandwidth = 0.003955

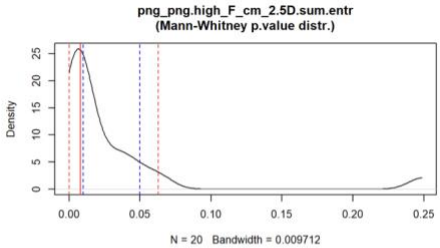
png_png.high_F_cm_2.5D.sum.entr
(Mann-Whitney p.value distr.)
Density
N = 20 Bandwidth = 0.009712

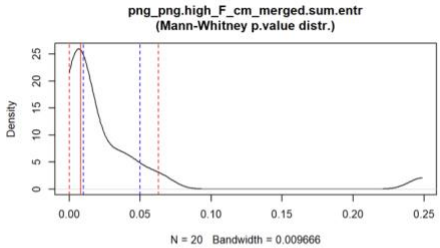
png_png.high_F_cm_merged.sum.entr
(Mann-Whitney p.value distr.)
Density
N = 20 Bandwidth = 0.009666

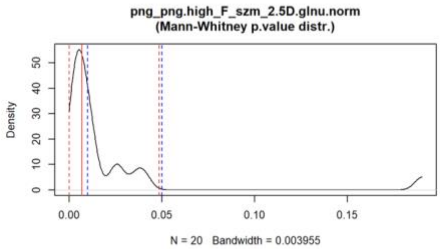
png_png.high_F_szm_2.5D.glnu.norm
(Mann-Whitney p.value distr.)
Density
N = 20 Bandwidth = 0.003955

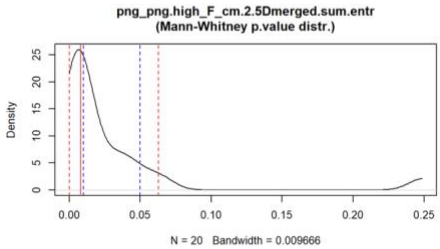
png_png.high_F_cm.2.5Dmerged.sum.entr
(Mann-Whitney p.value distr.)
Density
N = 20 Bandwidth = 0.009666

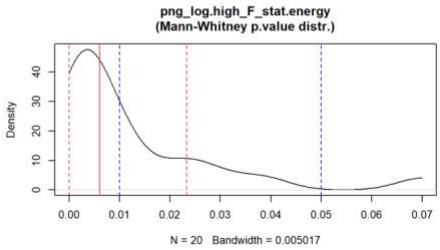
png_log.high_F_stat.energy
(Mann-Whitney p.value distr.)
Density
N = 20 Bandwidth = 0.005017

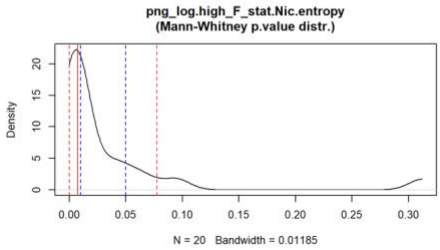
png_log.high_F_stat.Nic.entropy
(Mann-Whitney p.value distr.)
Density
N = 20 Bandwidth = 0.01185

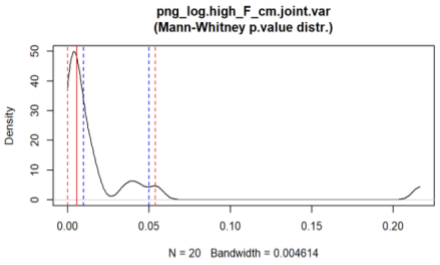
png_log.high_F_cm.joint.var
(Mann-Whitney p.value distr.)
Density
N = 20 Bandwidth = 0.004614

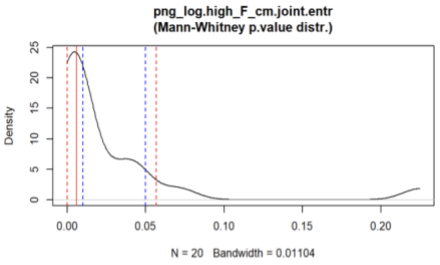
png_log.high_F_cm.joint.entr
(Mann-Whitney p.value distr.)
Density
N = 20 Bandwidth = 0.01104

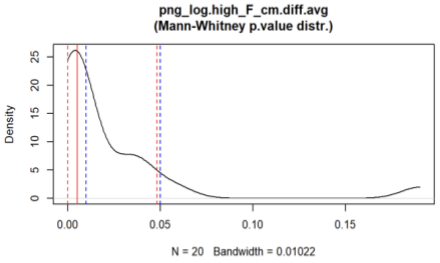
png_log.high_F_cm.diff.avg
(Mann-Whitney p.value distr.)
Density
N = 20 Bandwidth = 0.01022

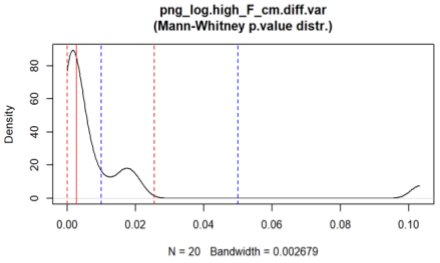
png_log.high_F_cm.diff.var
(Mann-Whitney p.value distr.)
Density
N = 20 Bandwidth = 0.002679

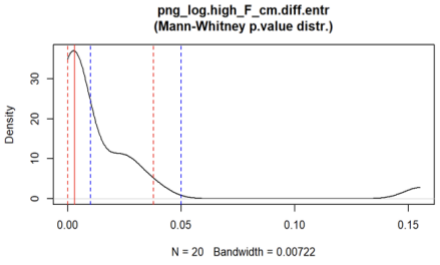
png_log.high_F_cm.diff.entr
(Mann-Whitney p.value distr.)
Density
N = 20 Bandwidth = 0.00722

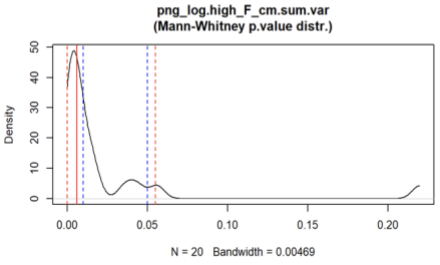
png_log.high_F_cm.sum.var
(Mann-Whitney p.value distr.)
Density
N = 20 Bandwidth = 0.00469

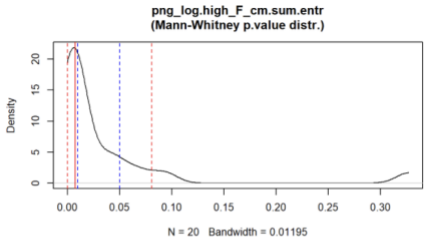
png_log.high_F_cm.sum.entr
(Mann-Whitney p.value distr.)
Density
N = 20 Bandwidth = 0.01195

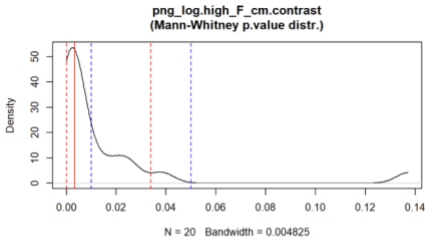
png_log.high_F_cm.contrast
(Mann-Whitney p.value distr.)
Density
N = 20 Bandwidth = 0.004825

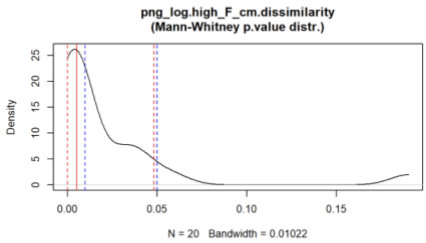
png_log.high_F_cm.dissimilarity
(Mann-Whitney p.value distr.)
Density
N = 20 Bandwidth = 0.01022

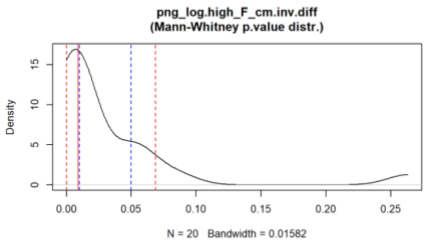
png_log.high_F_cm.inv.diff
(Mann-Whitney p.value distr.)
Density
N = 20 Bandwidth = 0.01582

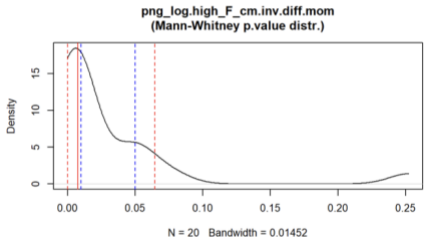
png_log.high_F_cm.inv.diff.mom
(Mann-Whitney p.value distr.)
Density
N = 20 Bandwidth = 0.01452

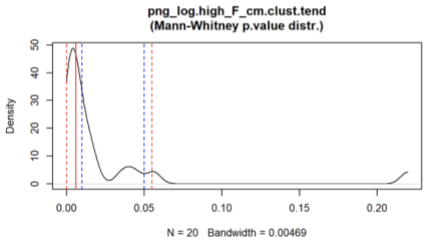
png_log.high_F_cm.clust.tend
(Mann-Whitney p.value distr.)
Density
N = 20 Bandwidth = 0.00469

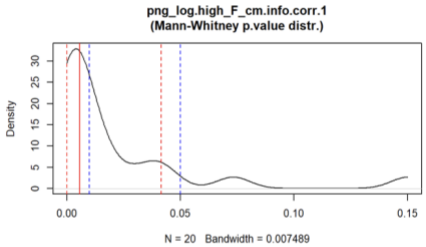
png_log.high_F_cm.info.corr.1
(Mann-Whitney p.value distr.)
Density
N = 20 Bandwidth = 0.007489

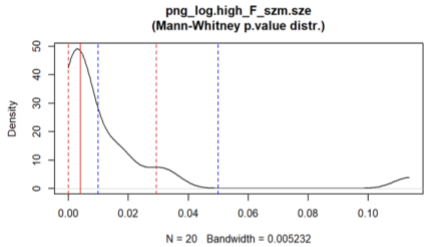
png_log.high_F_szm.sze
(Mann-Whitney p.value distr.)
Density
N = 20 Bandwidth = 0.005232

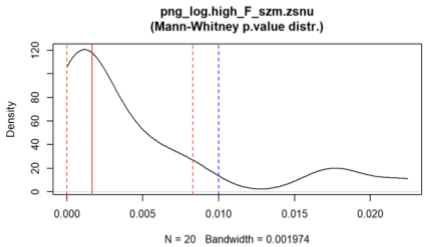
png_log.high_F_szm.zsnu
(Mann-Whitney p.value distr.)
Density
N = 20 Bandwidth = 0.001974

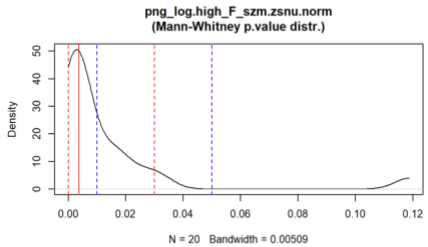
png_log.high_F_szm.zsnu.norm
(Mann-Whitney p.value distr.)
Density
N = 20 Bandwidth = 0.00509

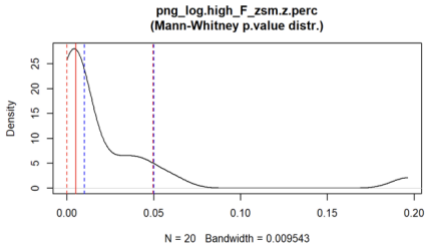
png_log.high_F_zsm.z.perc
(Mann-Whitney p.value distr.)
Density
N = 20 Bandwidth = 0.009543

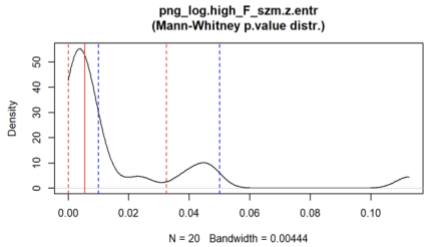
png_log.high_F_szm.z.entr
(Mann-Whitney p.value distr.)
Density
N = 20 Bandwidth = 0.00444

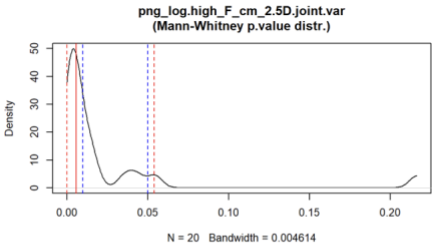
png_log.high_F_cm_2.5D.joint.var
(Mann-Whitney p.value distr.)
Density
N = 20 Bandwidth = 0.004614

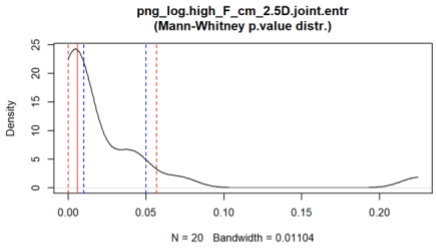
png_log.high_F_cm_2.5D.joint.entr
(Mann-Whitney p.value distr.)
Density
N = 20 Bandwidth = 0.01104

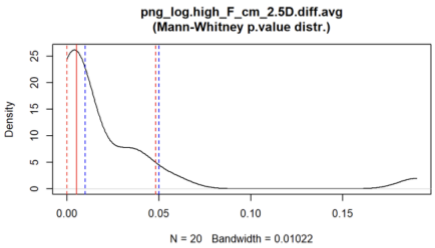
png_log.high_F_cm_2.5D.diff.avg
(Mann-Whitney p.value distr.)
Density
N = 20 Bandwidth = 0.01022

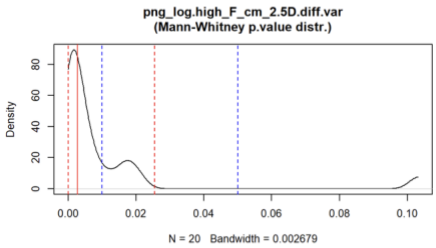
png_log.high_F_cm_2.5D.diff.var
(Mann-Whitney p.value distr.)
Density
N = 20 Bandwidth = 0.002679

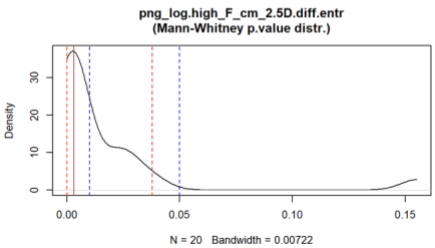
png_log.high_F_cm_2.5D.diff.entr
(Mann-Whitney p.value distr.)
Density
N = 20 Bandwidth = 0.00722

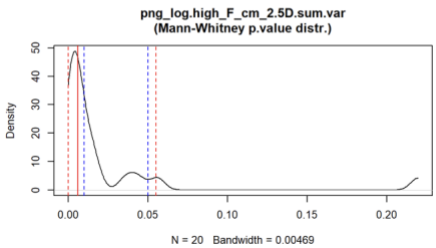
png_log.high_F_cm_2.5D.sum.var
(Mann-Whitney p.value distr.)
Density
N = 20 Bandwidth = 0.00469

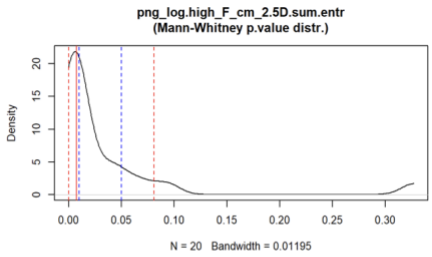
png_log.high_F_cm_2.5D.sum.entr
(Mann-Whitney p.value distr.)
Density
N = 20 Bandwidth = 0.01195

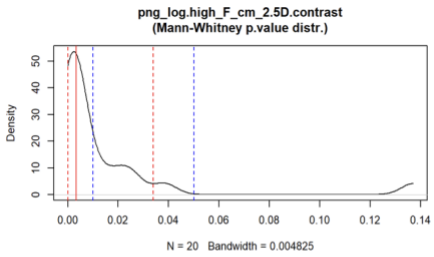
png_log.high_F_cm_2.5D.contrast
(Mann-Whitney p.value distr.)
Density
N = 20 Bandwidth = 0.004825

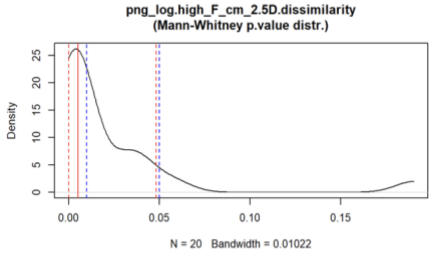
png_log.high_F_cm_2.5D.dissimilarity
(Mann-Whitney p.value distr.)
Density
N = 20 Bandwidth = 0.01022

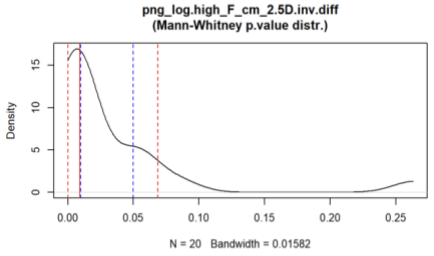
png_log.high_F_cm_2.5D.inv.diff
(Mann-Whitney p.value distr.)
Density
N = 20 Bandwidth = 0.01582

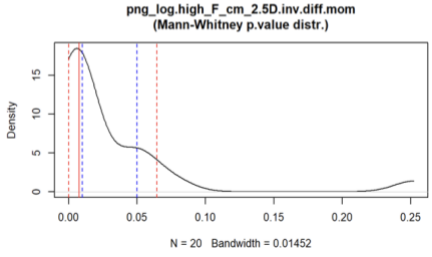
png_log.high_F_cm_2.5D.inv.diff.mom
(Mann-Whitney p.value distr.)
Density
N = 20 Bandwidth = 0.01452

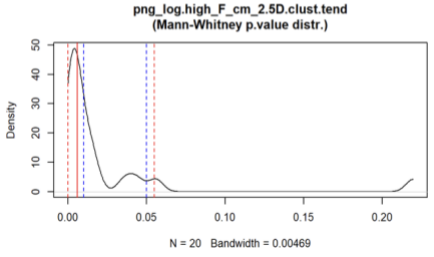
png_log.high_F_cm_2.5D.clust.tend
(Mann-Whitney p.value distr.)
Density
N = 20 Bandwidth = 0.00469

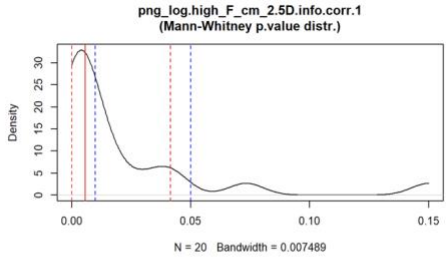
png_log.high_F_cm_2.5D.info.corr.1
(Mann-Whitney p.value distr.)
Density
N = 20 Bandwidth = 0.007489

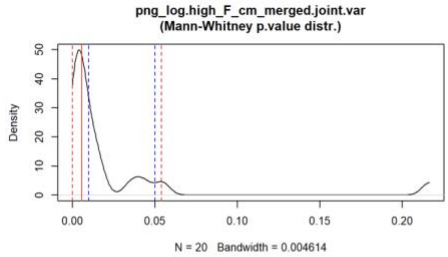
png_log.high_F_cm_merged.joint.var
(Mann-Whitney p.value distr.)
Density
N = 20 Bandwidth = 0.004614

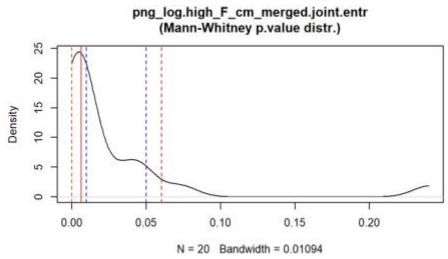
png_log.high_F_cm_merged.joint.entr
(Mann-Whitney p.value distr.)
Density
N = 20 Bandwidth = 0.01094

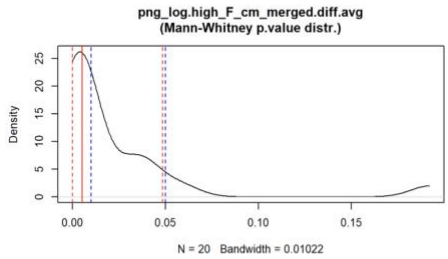
png_log.high_F_cm_merged.diff.avg
(Mann-Whitney p.value distr.)
Density
N = 20 Bandwidth = 0.01022

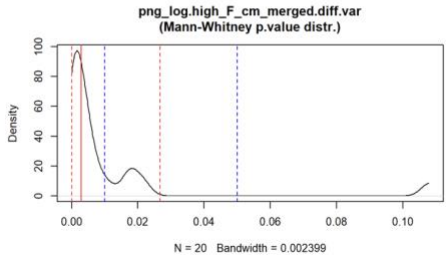
png_log.high_F_cm_merged.diff.var
(Mann-Whitney p.value distr.)
Density
N = 20 Bandwidth = 0.002399

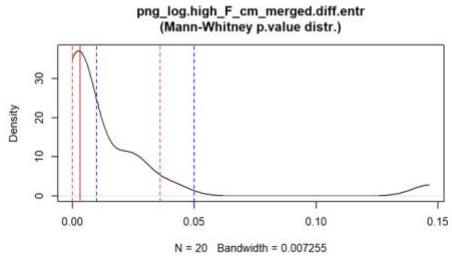
png_log.high_F_cm_merged.diff.entr
(Mann-Whitney p.value distr.)
Density
N = 20 Bandwidth = 0.007255

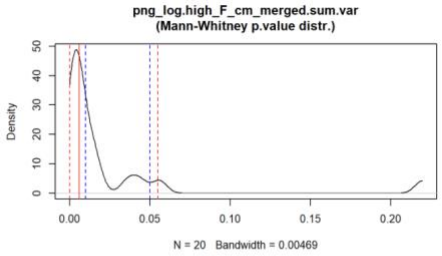
png_log.high_F_cm_merged.sum.var
(Mann-Whitney p.value distr.)
Density
N = 20 Bandwidth = 0.00469

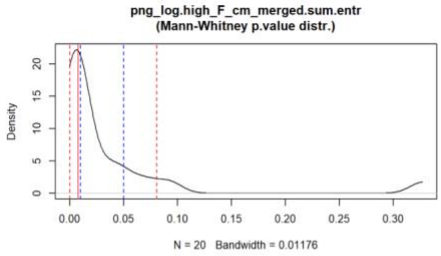
png_log.high_F_cm_merged.sum.entr
(Mann-Whitney p.value distr.)
Density
N = 20 Bandwidth = 0.01176

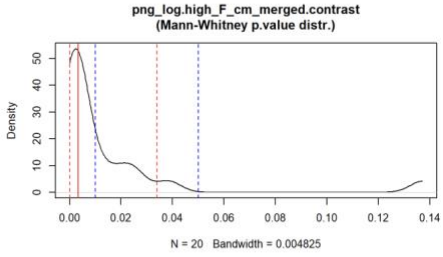
png_log.high_F_cm_merged.contrast
(Mann-Whitney p.value distr.)
Density
N = 20 Bandwidth = 0.004825

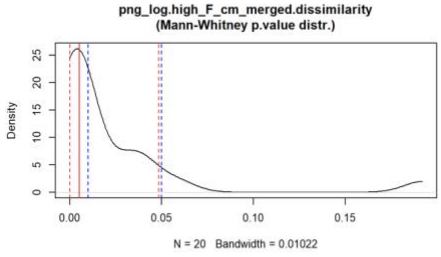
png_log.high_F_cm_merged.dissimilarity
(Mann-Whitney p.value distr.)
Density
N = 20 Bandwidth = 0.01022

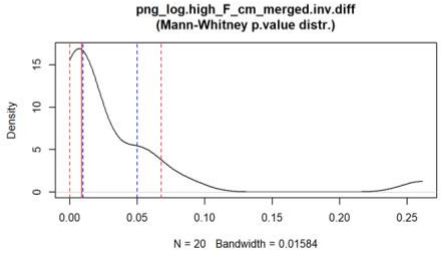
png_log.high_F_cm_merged.inv.diff
(Mann-Whitney p.value distr.)
Density
N = 20 Bandwidth = 0.01584

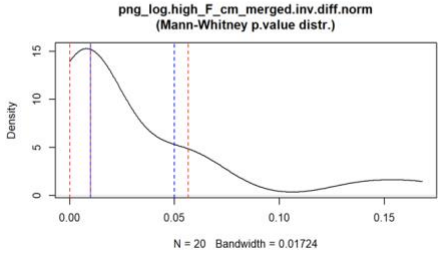
png_log.high_F_cm_merged.inv.diff.norm
(Mann-Whitney p.value distr.)
Density
N = 20 Bandwidth = 0.01724

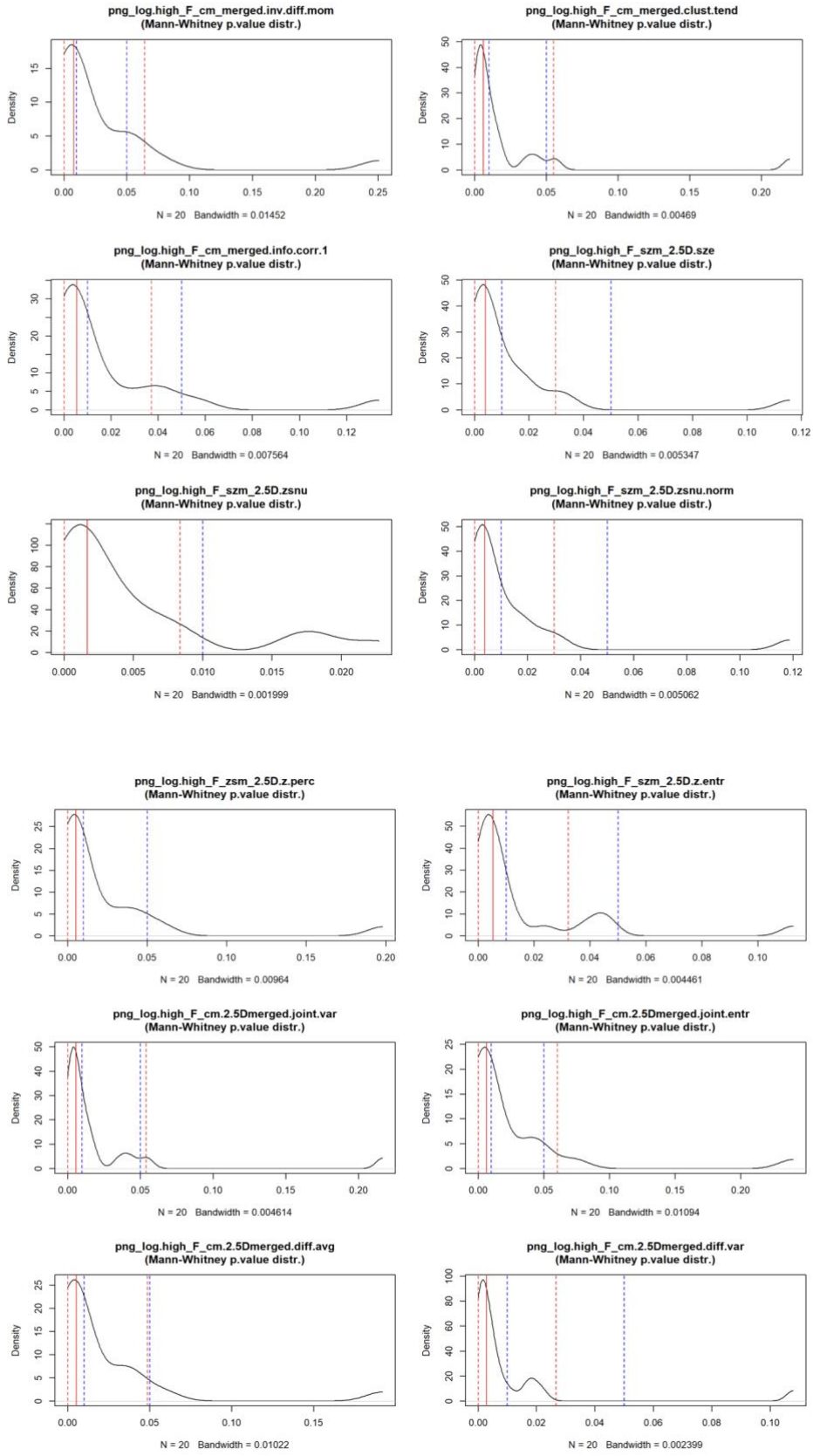
png_log.high_F_cm_merged.inv.diff.mom
(Mann-Whitney p.value distr.)
Density
N = 20 Bandwidth = 0.01452
png_log.high_F_cm_merged.clust.tend
(Mann-Whitney p.value distr.)
Density
N = 20 Bandwidth = 0.00469
png_log.high_F_cm_merged.info.corr.1
(Mann-Whitney p.value distr.)
Density
N = 20 Bandwidth = 0.007564
png_log.high_F_szm_2.5D.sze
(Mann-Whitney p.value distr.)
Density
N = 20 Bandwidth = 0.005347
png_log.high_F_szm_2.5D.zsnu
(Mann-Whitney p.value distr.)
Density
N = 20 Bandwidth = 0.001999
png_log.high_F_szm_2.5D.zsnu.norm
(Mann-Whitney p.value distr.)
Density
N = 20 Bandwidth = 0.005062
png_log.high_F_zsm_2.5D.z.perc
(Mann-Whitney p.value distr.)
Density
N = 20 Bandwidth = 0.00964
png_log.high_F_szm_2.5D.z.entr
(Mann-Whitney p.value distr.)
Density
N = 20 Bandwidth = 0.004461
png_log.high_F_cm.2.5Dmerged.joint.var
(Mann-Whitney p.value distr.)
Density
N = 20 Bandwidth = 0.004614
png_log.high_F_cm.2.5Dmerged.joint.entr
(Mann-Whitney p.value distr.)
Density
N = 20 Bandwidth = 0.01094
png_log.high_F_cm.2.5Dmerged.diff.avg
(Mann-Whitney p.value distr.)
Density
N = 20 Bandwidth = 0.01022
png_log.high_F_cm.2.5Dmerged.diff.var
(Mann-Whitney p.value distr.)
Density
N = 20 Bandwidth = 0.002399

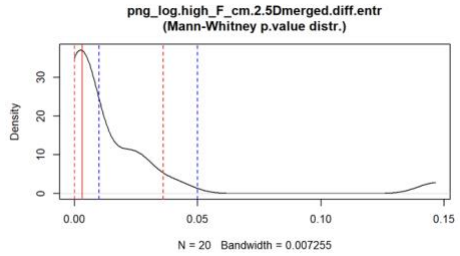
png_log.high_F_cm.2.5Dmerged.diff.entr
(Mann-Whitney p.value distr.)
Density
N = 20 Bandwidth = 0.007255

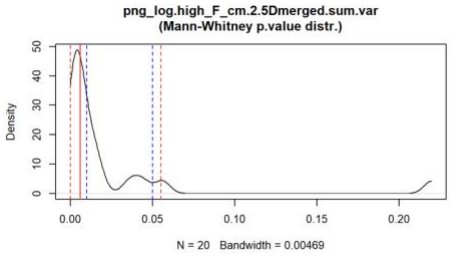
png_log.high_F_cm.2.5Dmerged.sum.var
(Mann-Whitney p.value distr.)
Density
N = 20 Bandwidth = 0.00469

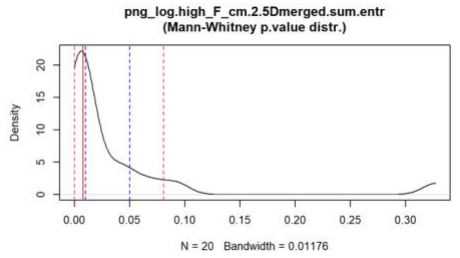
png_log.high_F_cm.2.5Dmerged.sum.entr
(Mann-Whitney p.value distr.)
Density
N = 20 Bandwidth = 0.01176

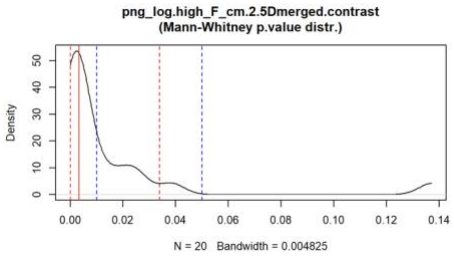
png_log.high_F_cm.2.5Dmerged.contrast
(Mann-Whitney p.value distr.)
Density
N = 20 Bandwidth = 0.004825

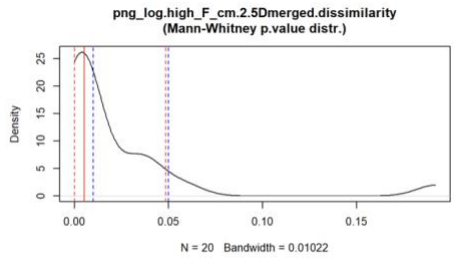
png_log.high_F_cm.2.5Dmerged.dissimilarity
(Mann-Whitney p.value distr.)
Density
N = 20 Bandwidth = 0.01022

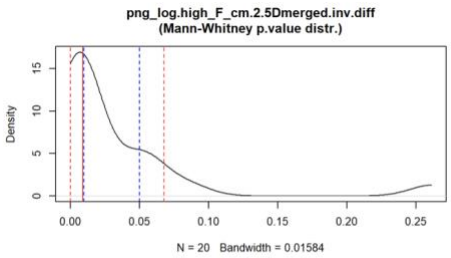
png_log.high_F_cm.2.5Dmerged.inv.diff
(Mann-Whitney p.value distr.)
Density
N = 20 Bandwidth = 0.01584

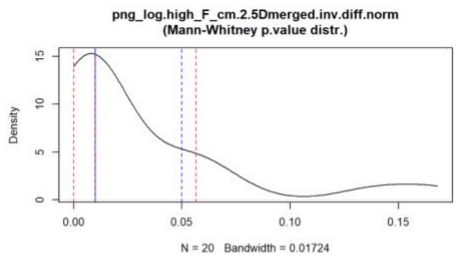
png_log.high_F_cm.2.5Dmerged.inv.diff.norm
(Mann-Whitney p.value distr.)
Density
N = 20 Bandwidth = 0.01724

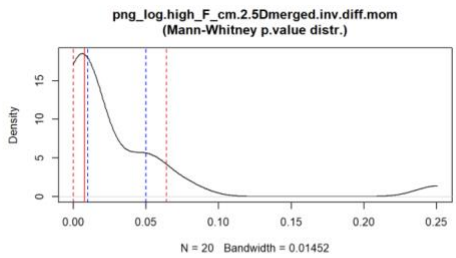
png_log.high_F_cm.2.5Dmerged.inv.diff.mom
(Mann-Whitney p.value distr.)
Density
N = 20 Bandwidth = 0.01452

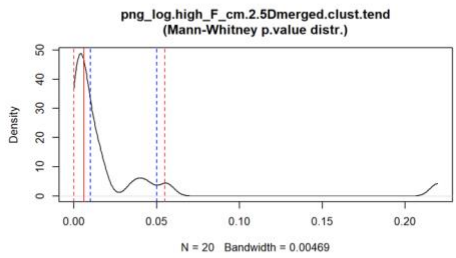
png_log.high_F_cm.2.5Dmerged.clust.tend
(Mann-Whitney p.value distr.)
Density
N = 20 Bandwidth = 0.00469

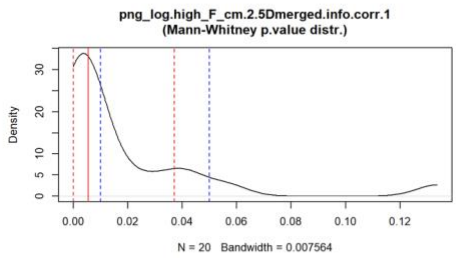
png_log.high_F_cm.2.5Dmerged.info.corr.1
(Mann-Whitney p.value distr.)
Density
N = 20 Bandwidth = 0.007564

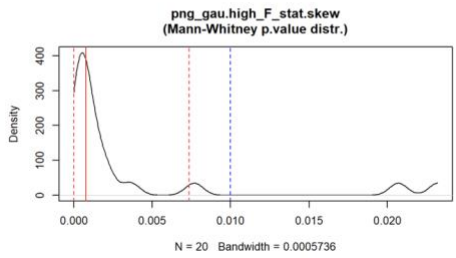
png_gau.high_F_stat.skew
(Mann-Whitney p.value distr.)
Density
N = 20 Bandwidth = 0.0005736

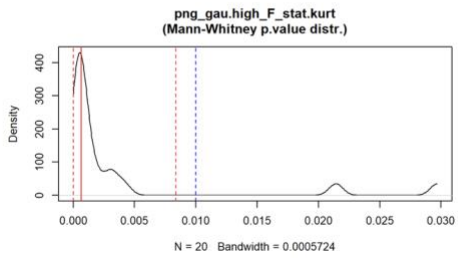
png_gau.high_F_stat.kurt
(Mann-Whitney p.value distr.)
Density
N = 20 Bandwidth = 0.0005724

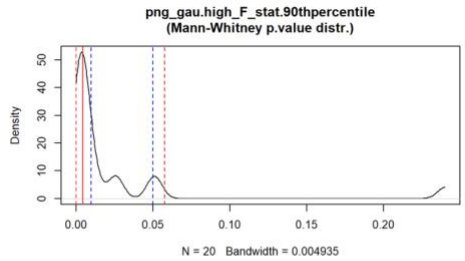
png_gau.high_F_stat.90thpercentile
(Mann-Whitney p.value distr.)
Density
N = 20 Bandwidth = 0.004935

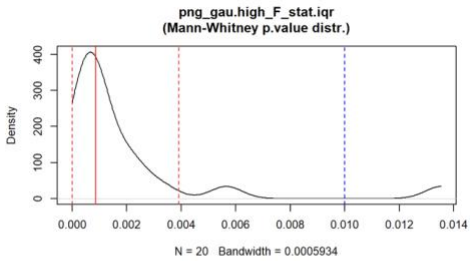
png_gau.high_F_stat.iqr
(Mann-Whitney p.value distr.)
Density
N = 20 Bandwidth = 0.0005934

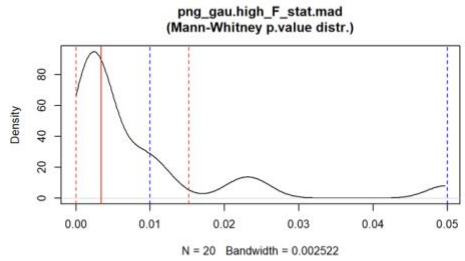
png_gau.high_F_stat.mad
(Mann-Whitney p.value distr.)
Density
N = 20 Bandwidth = 0.002522

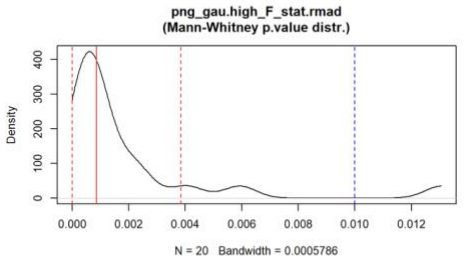
png_gau.high_F_stat.rmad
(Mann-Whitney p.value distr.)
Density
N = 20 Bandwidth = 0.0005786

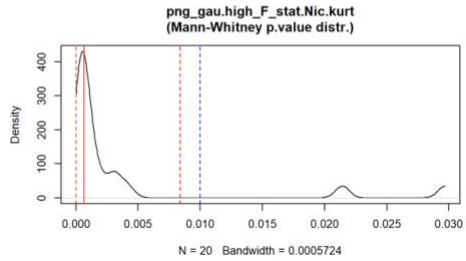
png_gau.high_F_stat.Nic.kurt
(Mann-Whitney p.value distr.)
Density
N = 20 Bandwidth = 0.0005724

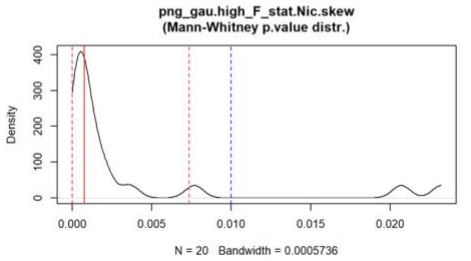
png_gau.high_F_stat.Nic.skew
(Mann-Whitney p.value distr.)
Density
N = 20 Bandwidth = 0.0005736

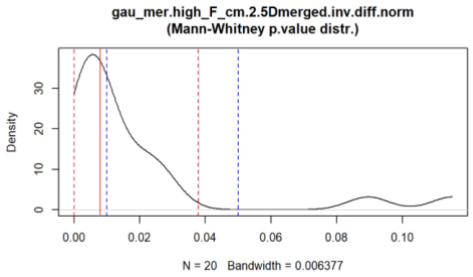
gau_mer.high_F_cm.2.5Dmerged.inv.diff.norm
(Mann-Whitney p.value distr.)
Density
N = 20 Bandwidth = 0.006377

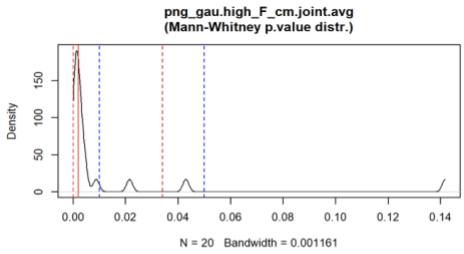
png_gau.high_F_cm.joint.avg
(Mann-Whitney p.value distr.)
Density
N = 20 Bandwidth = 0.001161

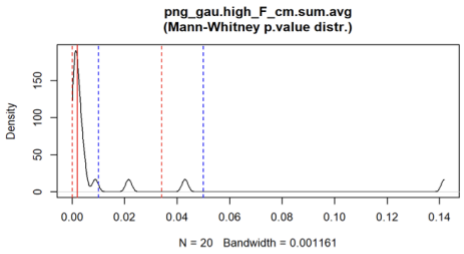
png_gau.high_F_cm.sum.avg
(Mann-Whitney p.value distr.)
Density
N = 20 Bandwidth = 0.001161

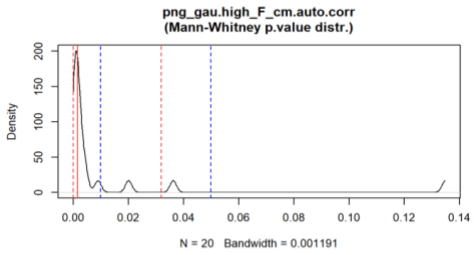
png_gau.high_F_cm.auto.corr
(Mann-Whitney p.value distr.)
Density
N = 20 Bandwidth = 0.001191

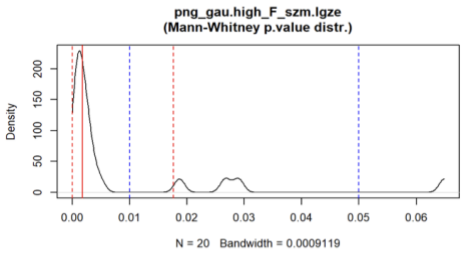
png_gau.high_F_szm.lgze
(Mann-Whitney p.value distr.)
Density
N = 20 Bandwidth = 0.0009119

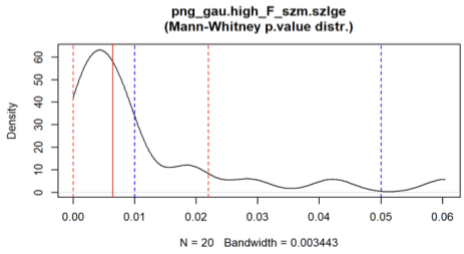
png_gau.high_F_szm.szlge
(Mann-Whitney p.value distr.)
Density
N = 20 Bandwidth = 0.003443

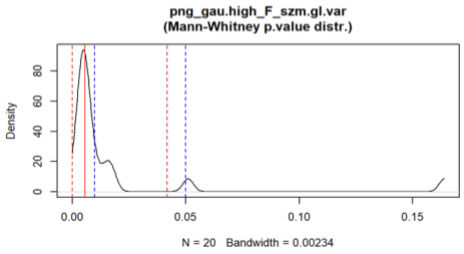
png_gau.high_F_szm.gl.var
(Mann-Whitney p.value distr.)
Density
N = 20 Bandwidth = 0.00234

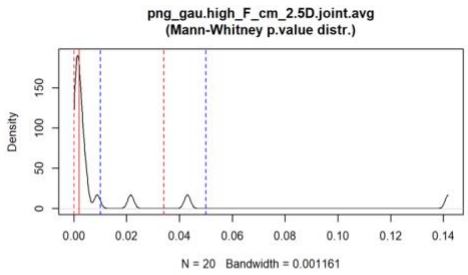
png_gau.high_F_cm_2.5D.joint.avg
(Mann-Whitney p.value distr.)
Density
N = 20 Bandwidth = 0.001161

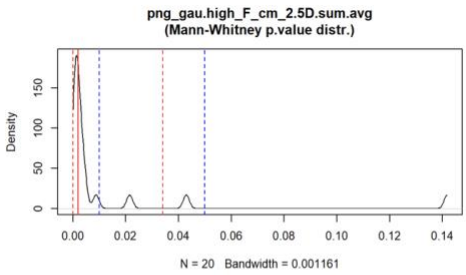
png_gau.high_F_cm_2.5D.sum.avg
(Mann-Whitney p.value distr.)
Density
N = 20 Bandwidth = 0.001161

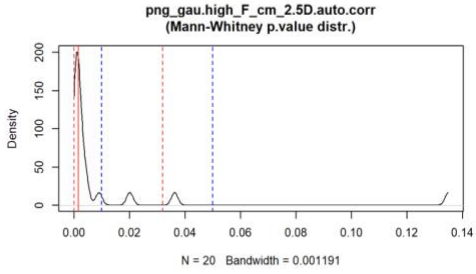
png_gau.high_F_cm_2.5D.auto.corr
(Mann-Whitney p.value distr.)
Density
N = 20 Bandwidth = 0.001191

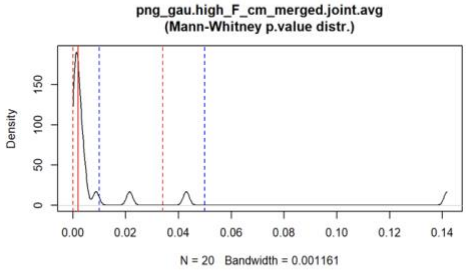
png_gau.high_F_cm_merged.joint.avg
(Mann-Whitney p.value distr.)
Density
N = 20 Bandwidth = 0.001161

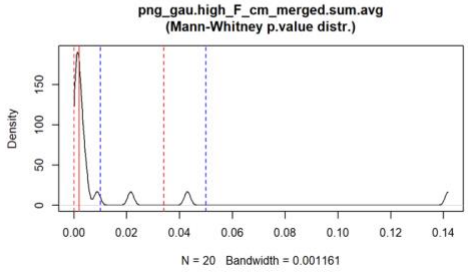
png_gau.high_F_cm_merged.sum.avg
(Mann-Whitney p.value distr.)
Density
N = 20 Bandwidth = 0.001161

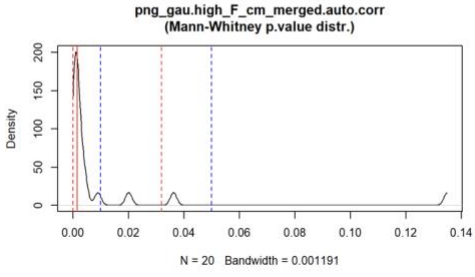
png_gau.high_F_cm_merged.auto.corr
(Mann-Whitney p.value distr.)
Density
N = 20 Bandwidth = 0.001191

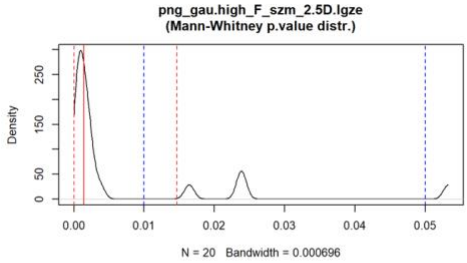
png_gau.high_F_szm_2.5D.lgze
(Mann-Whitney p.value distr.)
Density
N = 20 Bandwidth = 0.000696

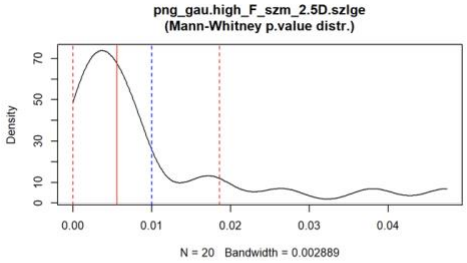
png_gau.high_F_szm_2.5D.szlge
(Mann-Whitney p.value distr.)
Density
N = 20 Bandwidth = 0.002889

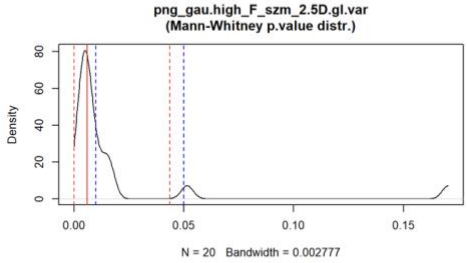
png_gau.high_F_szm_2.5D.gl.var
(Mann-Whitney p.value distr.)
Density
N = 20 Bandwidth = 0.002777

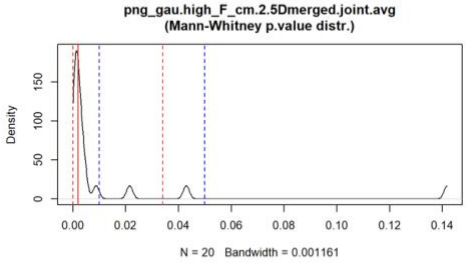
png_gau.high_F_cm.2.5Dmerged.joint.avg
(Mann-Whitney p.value distr.)
Density
N = 20 Bandwidth = 0.001161

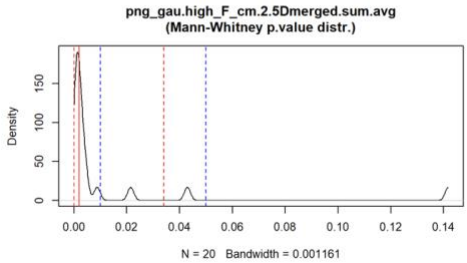
png_gau.high_F_cm.2.5Dmerged.sum.avg
(Mann-Whitney p.value distr.)
Density
N = 20 Bandwidth = 0.001161

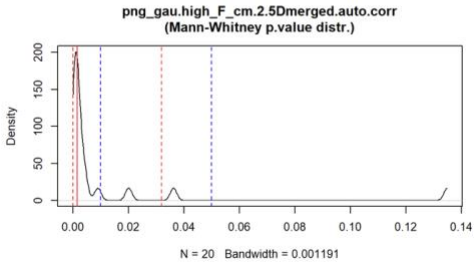
png_gau.high_F_cm.2.5Dmerged.auto.corr
(Mann-Whitney p.value distr.)
Density
N = 20 Bandwidth = 0.001191

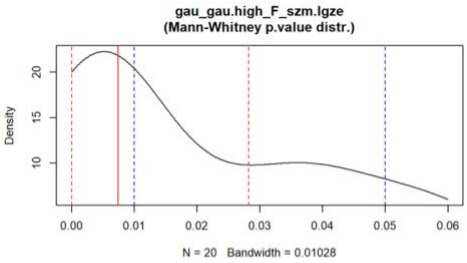
gau_gau.high_F_szm.lgze
(Mann-Whitney p.value distr.)
Density
N = 20 Bandwidth = 0.01028

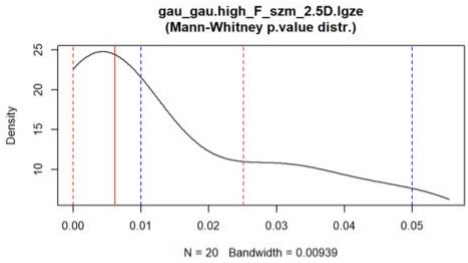
gau_gau.high_F_szm_2.5D.lgze
(Mann-Whitney p.value distr.)
Density
N = 20 Bandwidth = 0.00939

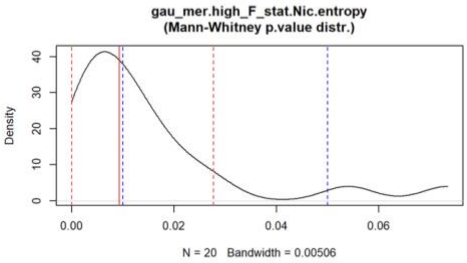
gau_mer.high_F_stat.Nic.entropy
(Mann-Whitney p.value distr.)
Density
N = 20 Bandwidth = 0.00506

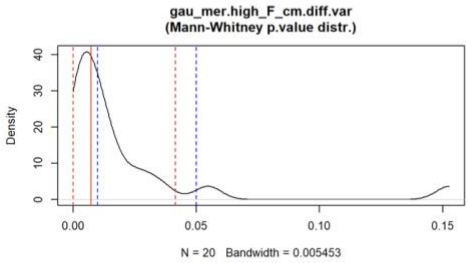
gau_mer.high_F_cm.diff.var
(Mann-Whitney p.value distr.)
Density
N = 20 Bandwidth = 0.005453

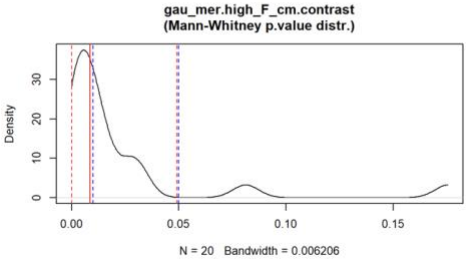
gau_mer.high_F_cm.contrast
(Mann-Whitney p.value distr.)
Density
N = 20 Bandwidth = 0.006206

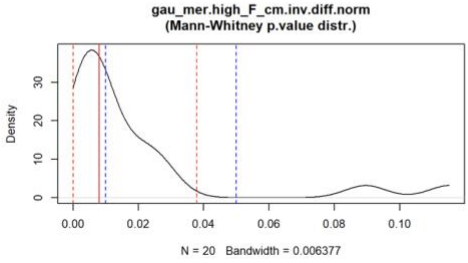
gau_mer.high_F_cm.inv.diff.norm
(Mann-Whitney p.value distr.)
Density
N = 20 Bandwidth = 0.006377

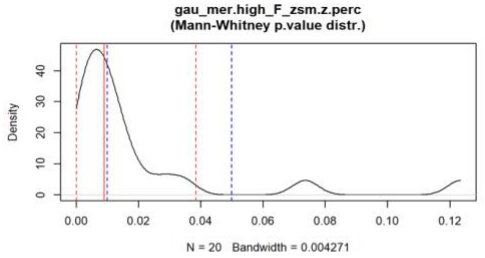
gau_mer.high_F_zsm.z.perc
(Mann-Whitney p.value distr.)
Density
N = 20 Bandwidth = 0.004271

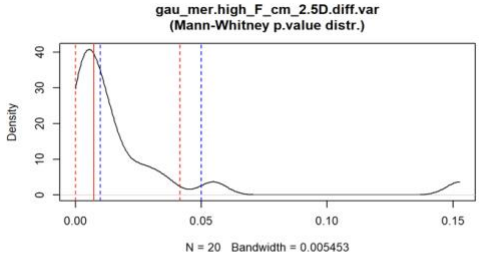
gau_mer.high_F_cm_2.5D.diff.var
(Mann-Whitney p.value distr.)
Density
N = 20 Bandwidth = 0.005453

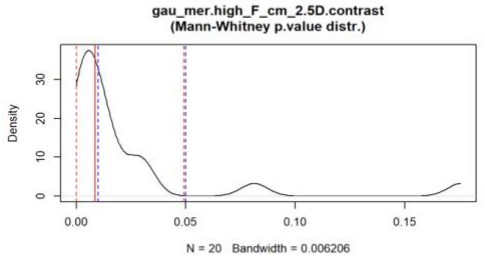
gau_mer.high_F_cm_2.5D.contrast
(Mann-Whitney p.value distr.)
Density
N = 20 Bandwidth = 0.006206

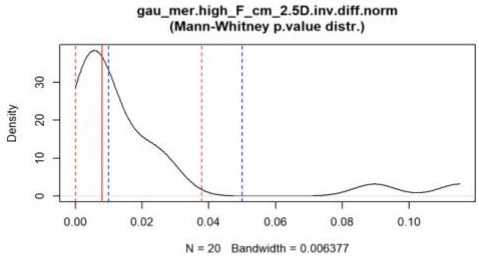
gau_mer.high_F_cm_2.5D.inv.diff.norm
(Mann-Whitney p.value distr.)
Density
N = 20 Bandwidth = 0.006377

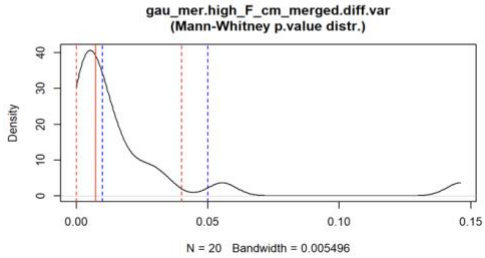
gau_mer.high_F_cm_merged.diff.var
(Mann-Whitney p.value distr.)
Density
N = 20 Bandwidth = 0.005496

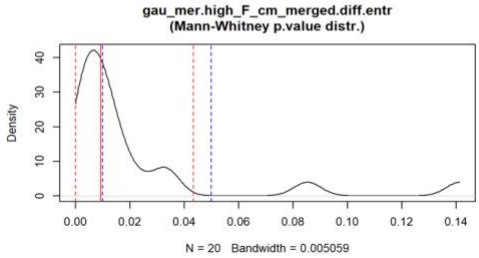
gau_mer.high_F_cm_merged.diff.entr
(Mann-Whitney p.value distr.)
Density
N = 20 Bandwidth = 0.005059

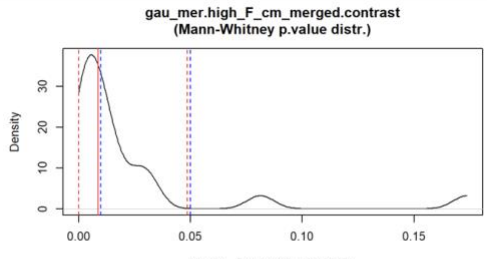
gau_mer.high_F_cm_merged.contrast
(Mann-Whitney p.value distr.)
Density
N = 20 Bandwidth = 0.006181

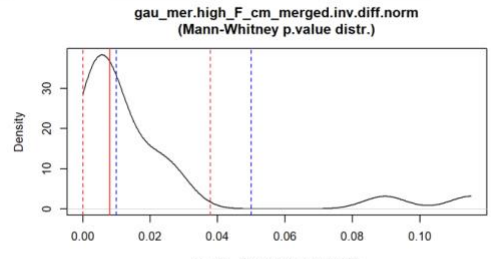
gau_mer.high_F_cm_merged.inv.diff.norm
(Mann-Whitney p.value distr.)
Density
N = 20 Bandwidth = 0.006377

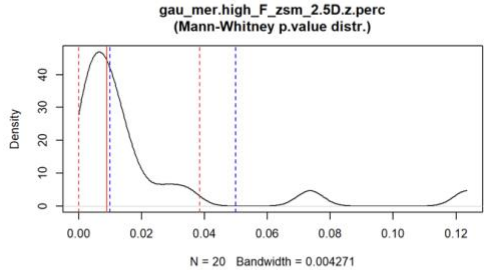
gau_mer.high_F_zsm_2.5D.z.perc
(Mann-Whitney p.value distr.)
Density
N = 20 Bandwidth = 0.004271

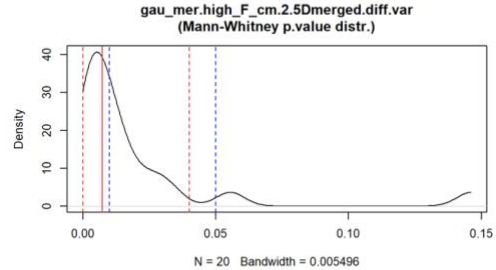
gau_mer.high_F_cm.2.5Dmerged.diff.var
(Mann-Whitney p.value distr.)
Density
N = 20 Bandwidth = 0.005496

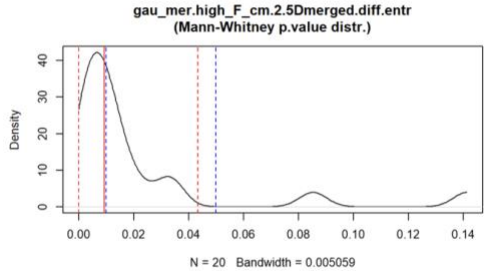
gau_mer.high_F_cm.2.5Dmerged.diff.entr
(Mann-Whitney p.value distr.)
Density
N = 20 Bandwidth = 0.005059

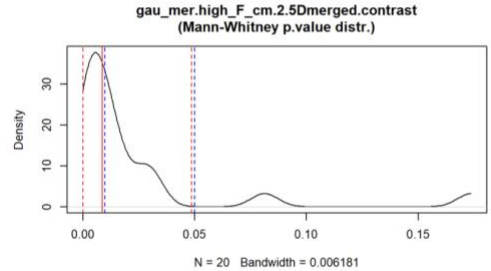
gau_mer.high_F_cm.2.5Dmerged.contrast
(Mann-Whitney p.value distr.)
Density
N = 20 Bandwidth = 0.006181

The performance matrices on the training set and on the testing set for the bivariate investigation are as follows. They are ordered, from left to right, by pairs of variables with higher AUC at the training set (in blue) and the corresponding AUC values at the testing set (in red):

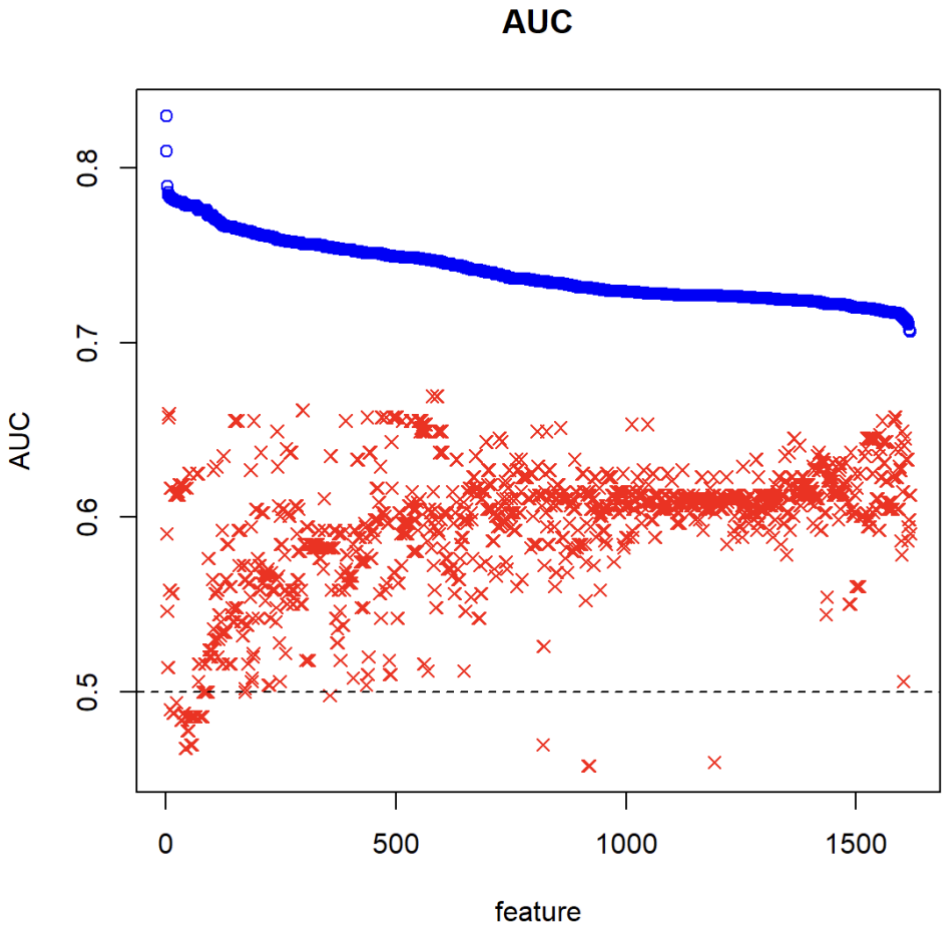

The best performing bivariate models can be plotted as follows (melanomas in red, dysplastic nevi in blue):

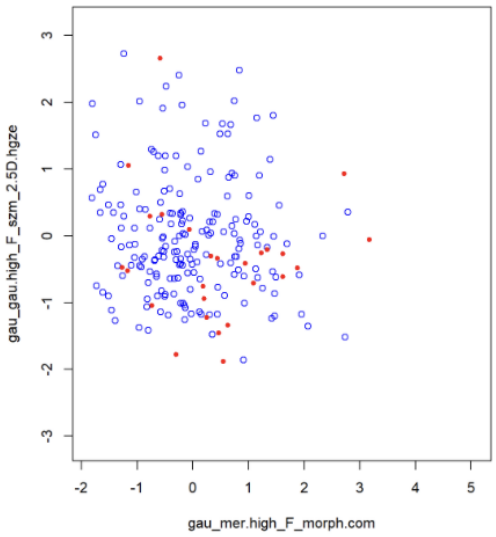
gau_gau.high_F_szm_2.5D.hgze
gau_mer.high_F_morph.com

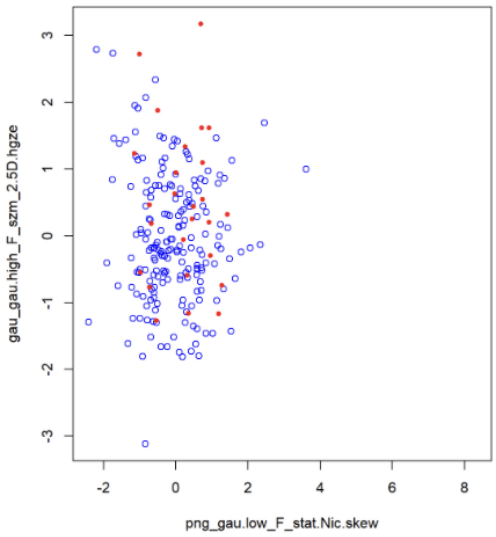
gau_gau.high_F_szm_2.5D.hgze
png_gau.low_F_stat.Nic.skew

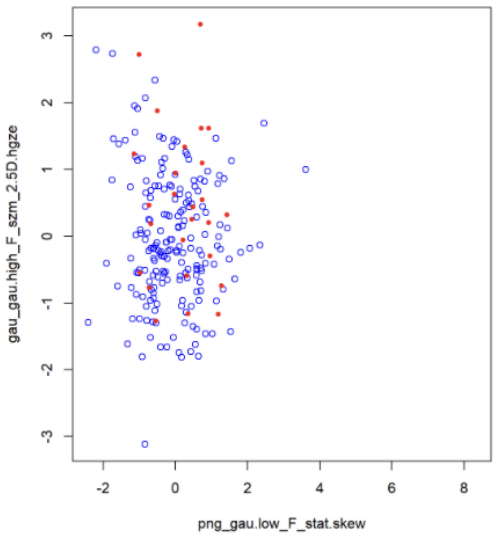
gau_gau.high_F_szm_2.5D.hgze
png_gau.low_F_stat.skew

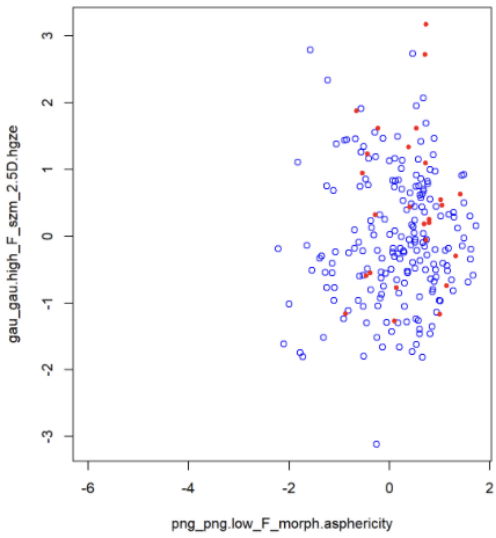
gau_gau.high_F_szm_2.5D.hgze
png_png.low_F_morph.asphericity

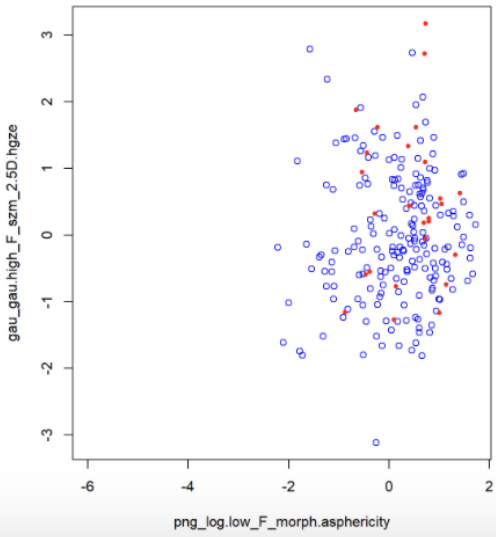
gau_gau.high_F_szm_2.5D.hgze
png_log.low_F_morph.asphericity

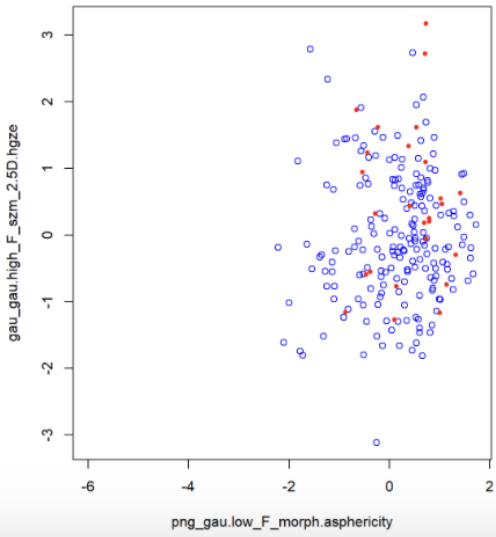
gau_gau.high_F_szm_2.5D.hgze
png_gau.low_F_morph.asphericity

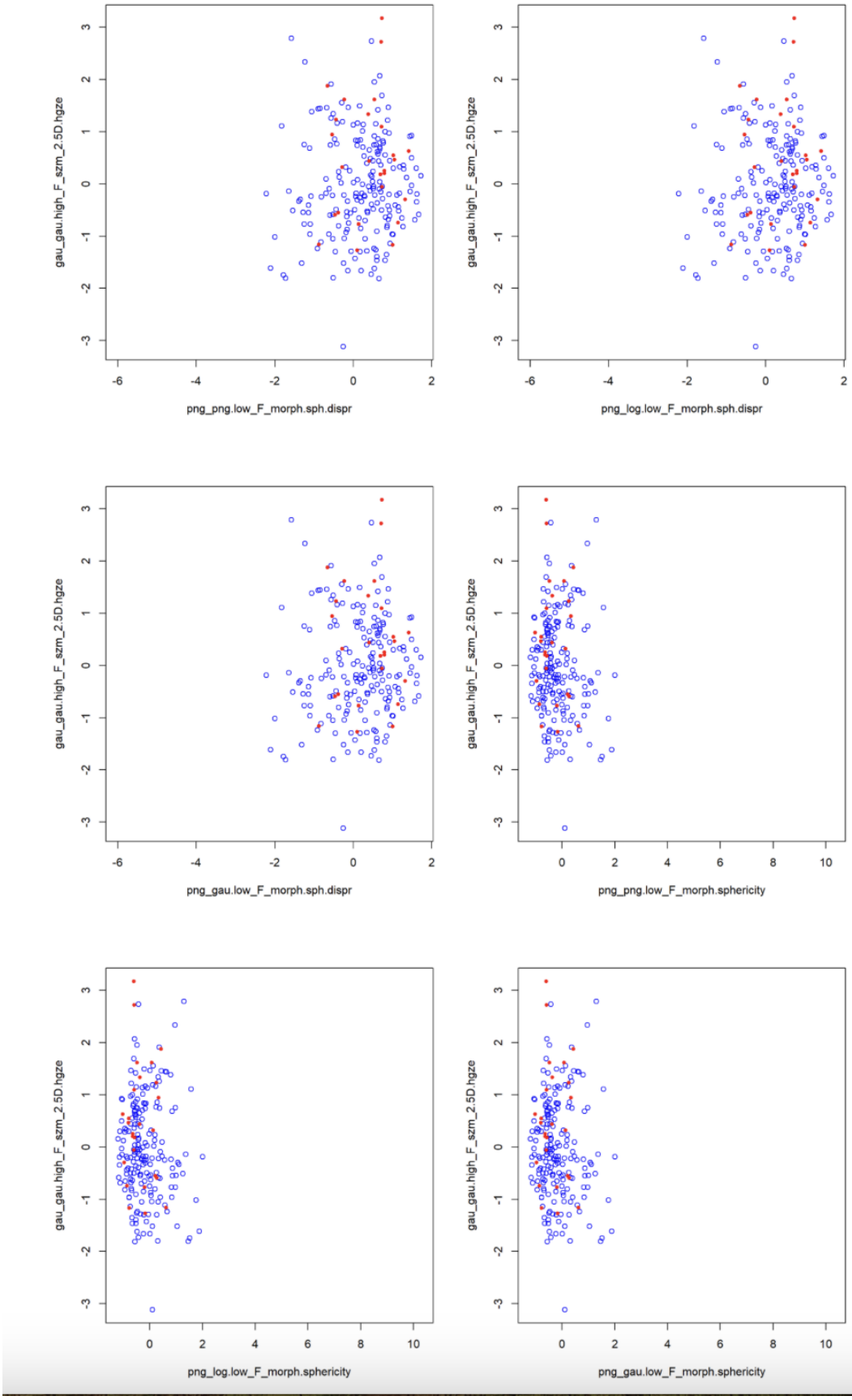
gau_gau.high_F_szm_2.5D.hgze
png_png.low_F_morph.sph.dispr
gau_gau.high_F_szm_2.5D.hgze
png_log.low_F_morph.sph.dispr
gau_gau.high_F_szm_2.5D.hgze
png_gau.low_F_morph.sph.dispr
gau_gau.high_F_szm_2.5D.hgze
png_png.low_F_morph.sphericity
gau_gau.high_F_szm_2.5D.hgze
png_log.low_F_morph.sphericity
gau_gau.high_F_szm_2.5D.hgze
png_gau.low_F_morph.sphericity

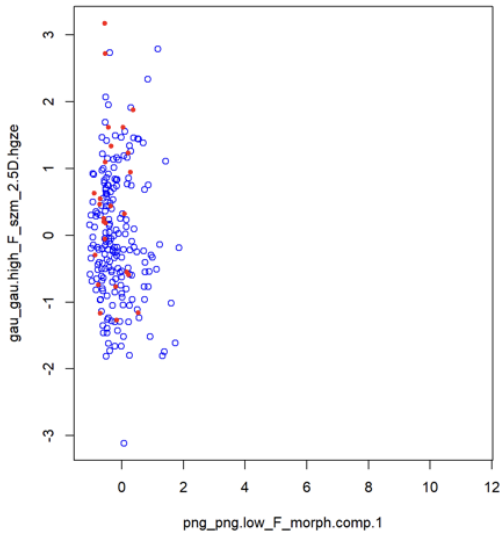
gau_gau.high_F_szm_2.5D.hgze
png_png.low_F_morph.comp.1

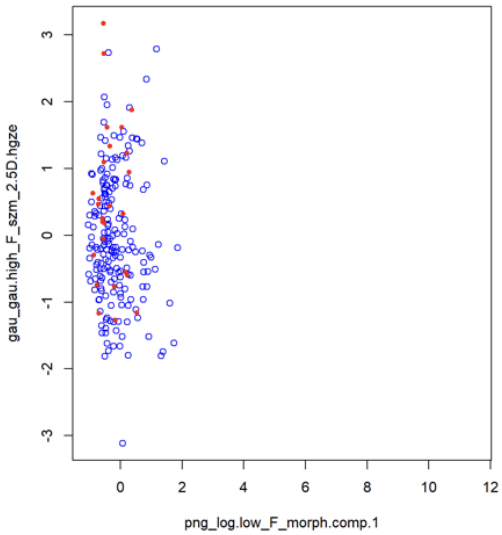
gau_gau.high_F_szm_2.5D.hgze
png_log.low_F_morph.comp.1

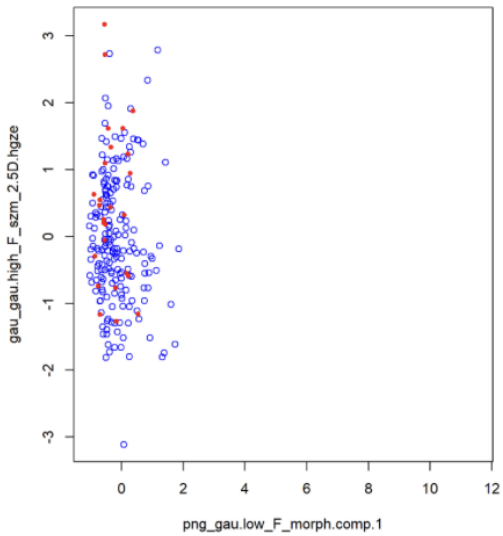
gau_gau.high_F_szm_2.5D.hgze
png_gau.low_F_morph.comp.1

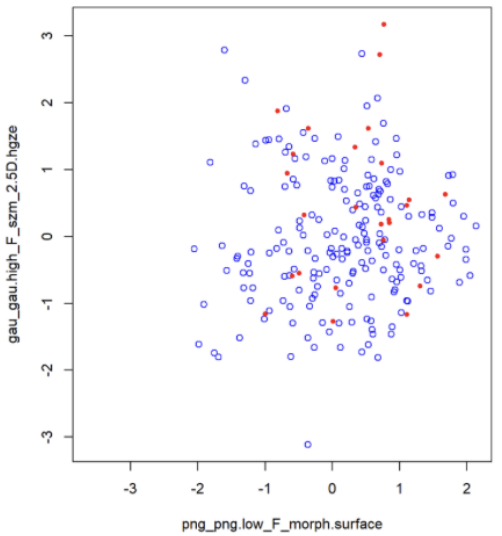
gau_gau.high_F_szm_2.5D.hgze
png_png.low_F_morph.surface

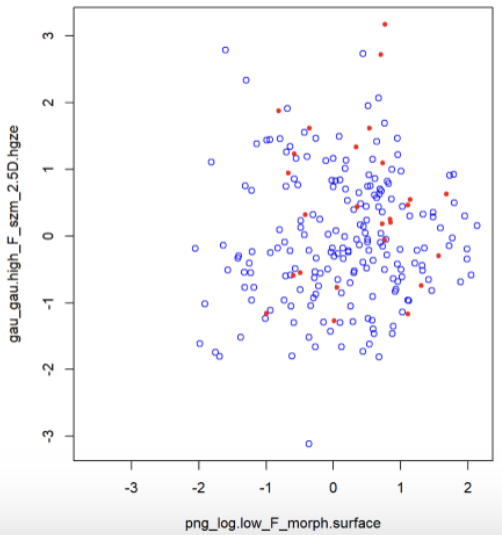
gau_gau.high_F_szm_2.5D.hgze
png_log.low_F_morph.surface

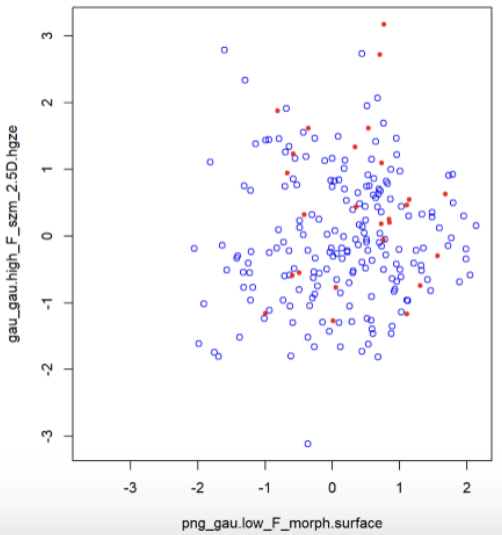
gau_gau.high_F_szm_2.5D.hgze
png_gau.low_F_morph.surface

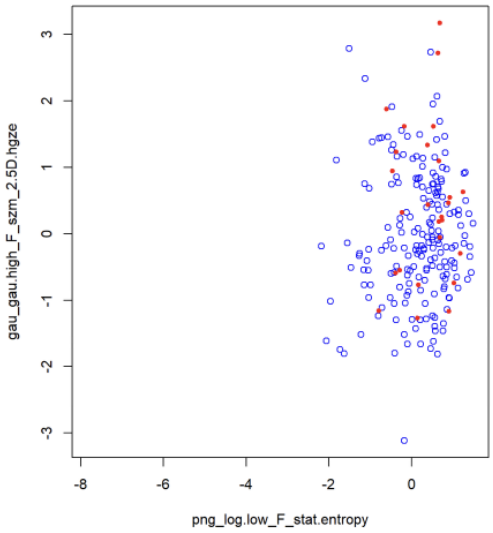
gau_gau.high_F_szm_2.5D.hgze
png_log.low_F_stat.entropy

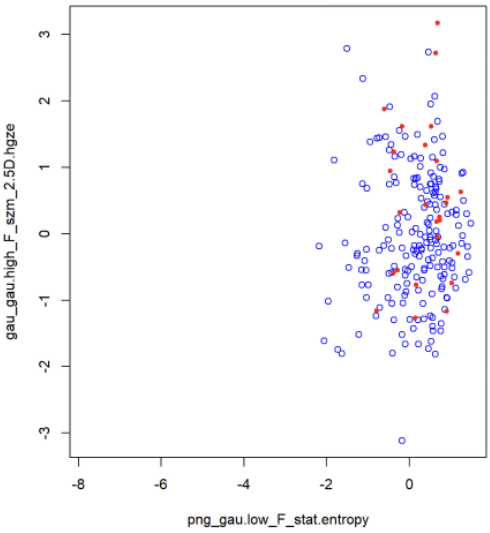
gau_gau.high_F_szm_2.5D.hgze
png_gau.low_F_stat.entropy

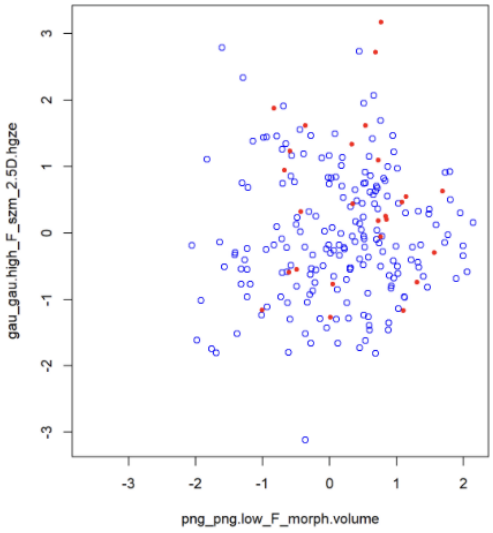
gau_gau.high_F_szm_2.5D.hgze
png_png.low_F_morph.volume

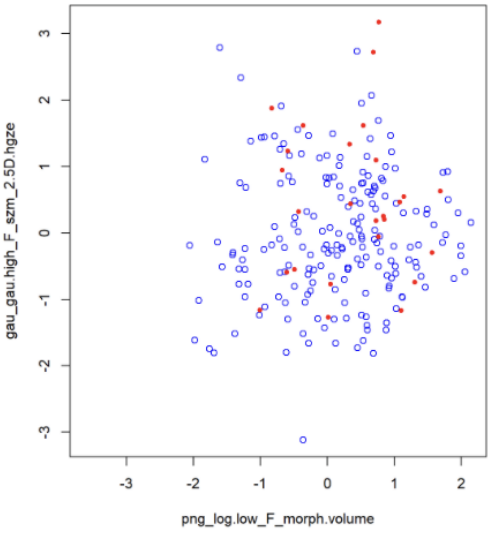
gau_gau.high_F_szm_2.5D.hgze
png_log.low_F_morph.volume

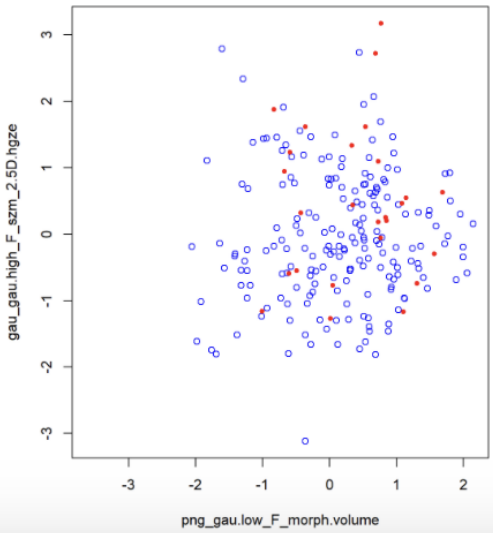
gau_gau.high_F_szm_2.5D.hgze
png_gau.low_F_morph.volume

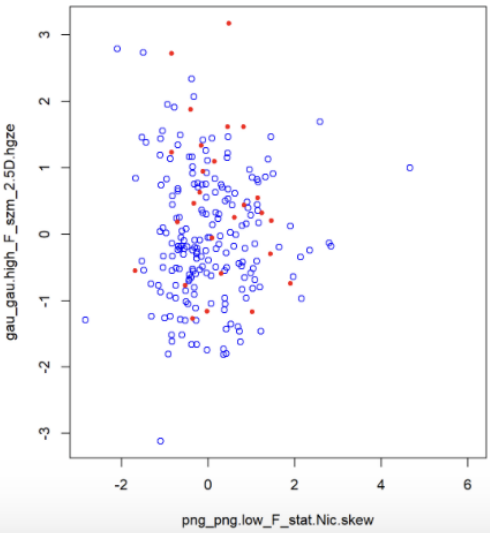
gau_gau.high_F_szm_2.5D.hgze
png_png.low_F_stat.Nic.skew

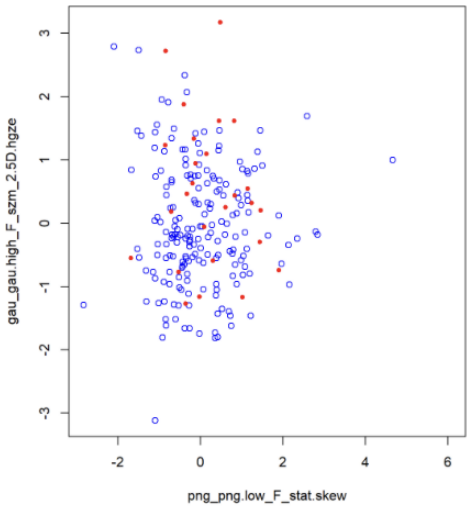
gau_gau.high_F_szm_2.5D.hgze
png_png.low_F_stat.skew

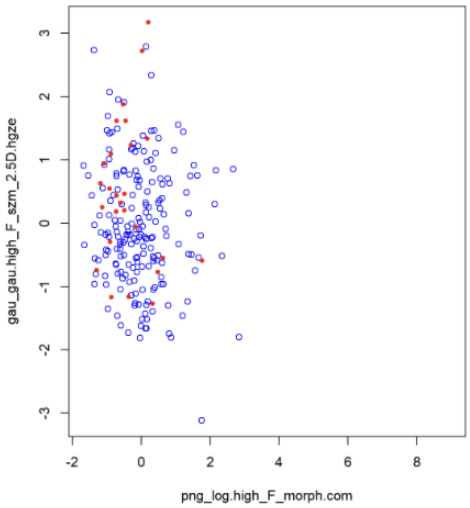
gau_gau.high_F_szm_2.5D.hgze
png_log.high_F_morph.com

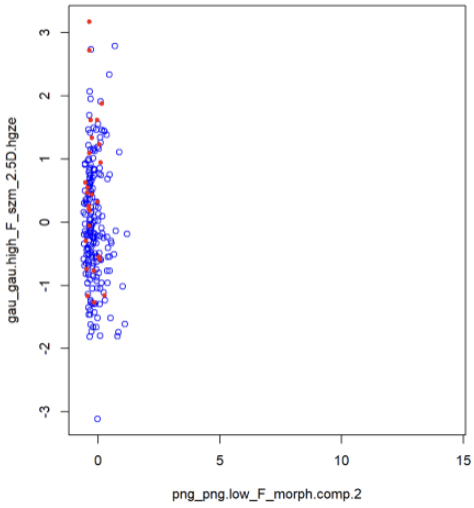
gau_gau.high_F_szm_2.5D.hgze
png_png.low_F_morph.comp.2

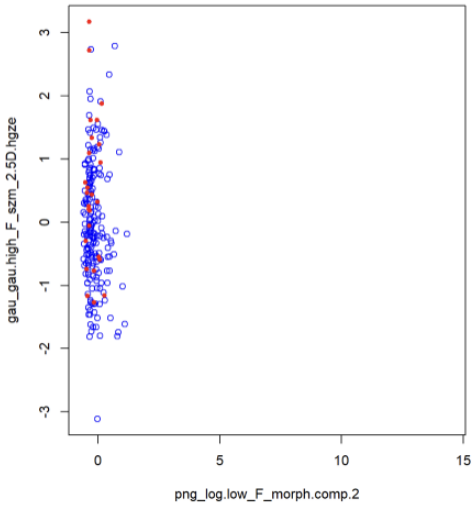
gau_gau.high_F_szm_2.5D.hgze
png_log.low_F_morph.comp.2

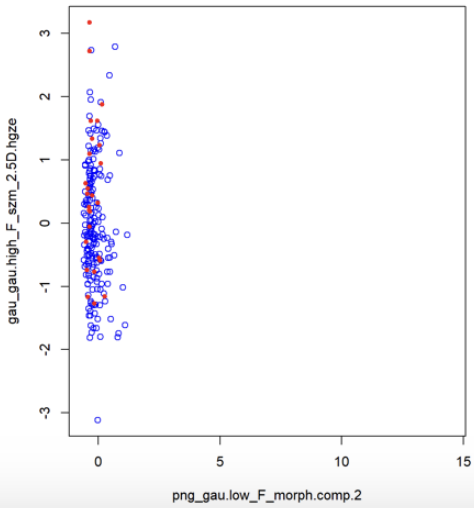
gau_gau.high_F_szm_2.5D.hgze
png_gau.low_F_morph.comp.2

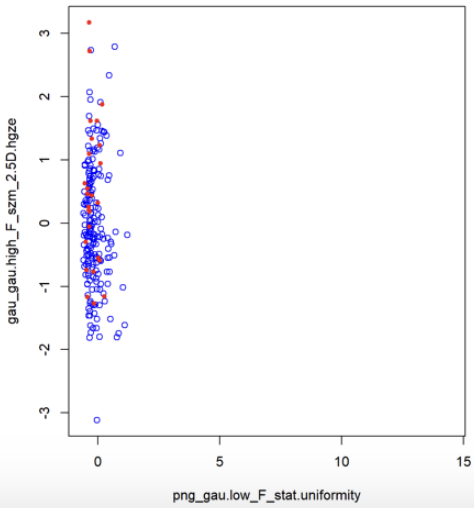
gau_gau.high_F_szm_2.5D.hgze
png_gau.low_F_stat.uniformity

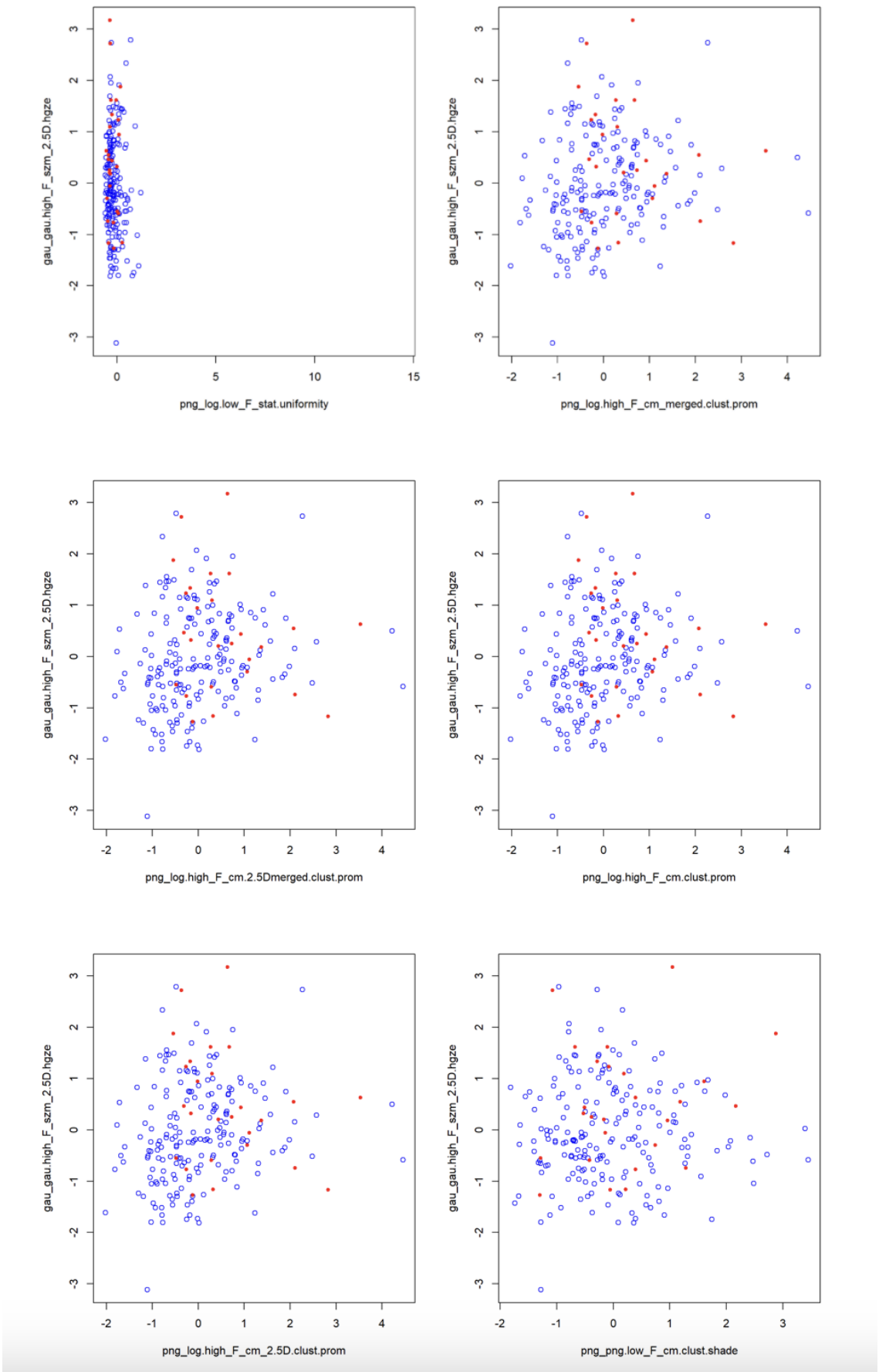
gau_gau.high_F_szm_2.5D.hgze
png_log.low_F_stat.uniformity
gau_gau.high_F_szm_2.5D.hgze
png_log.high_F_cm_merged.clust.prom
gau_gau.high_F_szm_2.5D.hgze
png_log.high_F_cm.2.5Dmerged.clust.prom
gau_gau.high_F_szm_2.5D.hgze
png_log.high_F_cm.clust.prom
gau_gau.high_F_szm_2.5D.hgze
png_log.high_F_cm_2.5D.clust.prom
gau_gau.high_F_szm_2.5D.hgze
png_png.low_F_cm.clust.shade

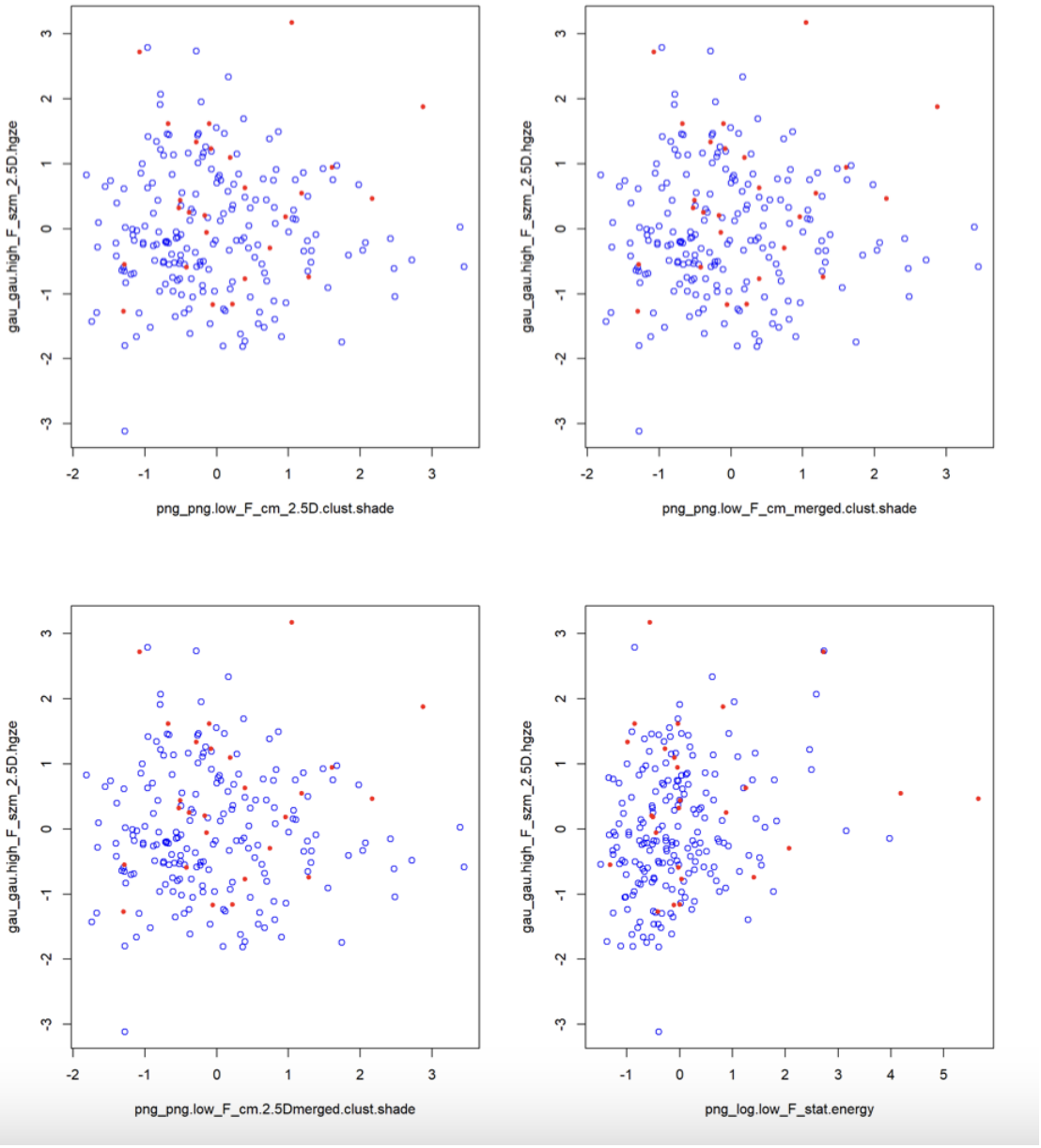
gau_gau.high_F_szm_2.5D.hgze
png_png.low_F_cm_2.5D.clust.shade
gau_gau.high_F_szm_2.5D.hgze
png_png.low_F_cm_merged.clust.shade
gau_gau.high_F_szm_2.5D.hgze
png_png.low_F_cm.2.5Dmerged.clust.shade
gau_gau.high_F_szm_2.5D.hgze
png_log.low_F_stat.energy

Regarding the decision tree, the KDE of PPV and NPV are, in the training set:

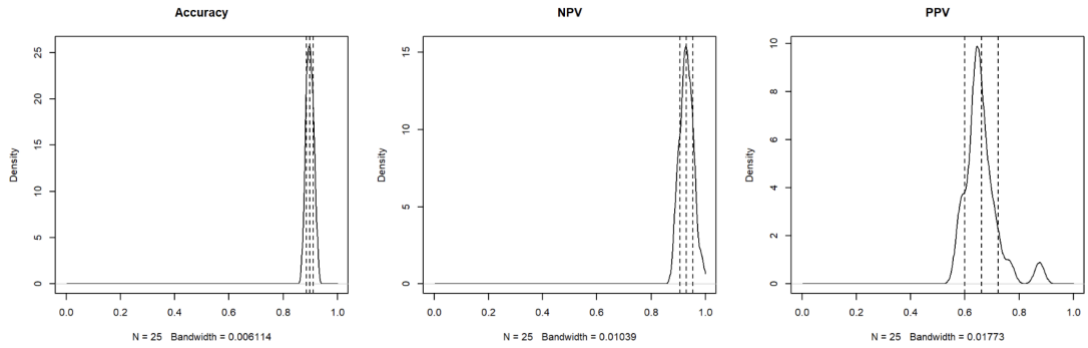

With a mean (accuracy) of 0.8981622, a mean (NPV) of 0.9303623 and a mean (PPV) of 0.6610516.

The KDE of PPV and NPV are instead, in the testing set:

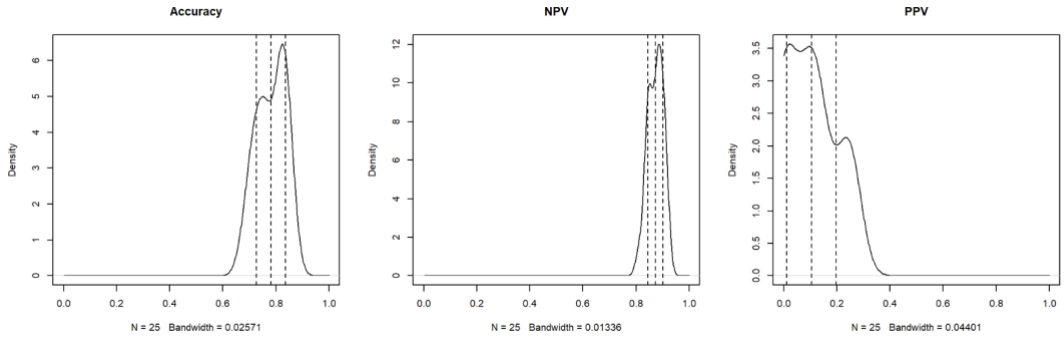

With a mean (accuracy) of 0.8981622, a mean (NPV) of 0.8733818 and a mean (PPV) of 0.1034342.

The random forest showed similar characteristics with the following NPV and PPV values for the training set and the testing set:

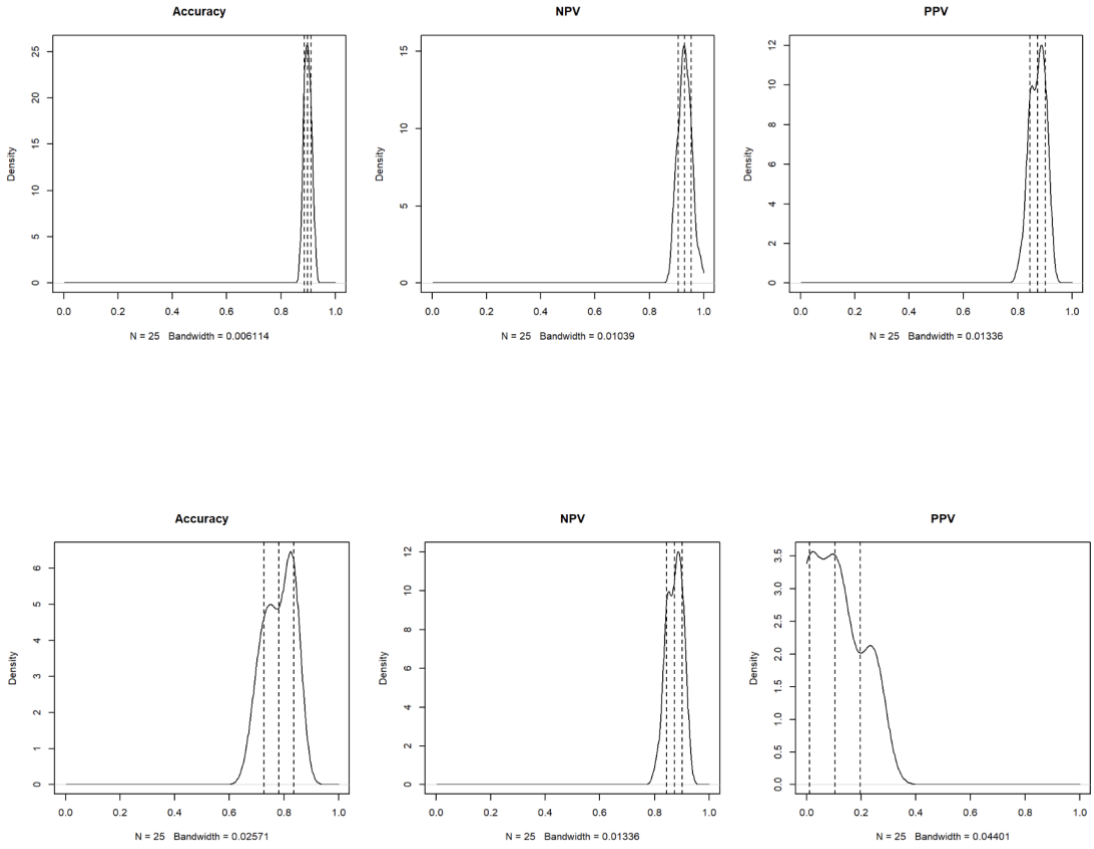

5. DISCUSSION

Melanoma remains an important public health concern globally. It is characterized by high incidence in fair-skinned populations of European descent and disproportionate mortality in transitioning countries.
A worldwide total of 325.000 new melanoma cases and 57.000 deaths was estimated for 2020. If these rates continue, the burden from melanoma is estimated to increase to 510 000 new cases (a roughly 50% increase) and to 96 000 deaths (a 68% increase) by 2040. [69]

To face this health problem, dermatologists have focused on the possibility of achieving an early diagnosis of skin tumors. If the latter could lead to an increase in the diagnosis of skin cancers, on the other hand it could theoretically eliminate the associated mortality. In fact, identifying and radically removing the tumor at an early stage drastically reduces the risk of distant metastases and the morbidity linked to the surgical removal of large lesions. For this reason, in today's clinical practice several diagnostic tools are used alone or in combination to improve the diagnostic performance of the dermatologist. Some of these instruments (such as manual dermoscopy and videodermoscopy) are very widespread, others such as 3D Total body Photography (3D TBP), RCM, LC-OCT are currently the exclusive prerogative of second level centers and hospitals due to the high costs of the devices. Ideally, when a skin lesion is considered clinically and dermoscopically suspicious, it is referred for second-level diagnostic exams such as RCM and LC-OCT. These different steps are carried out because, using clinical and dermoscopic diagnosis, the number needed to biopsy (NNB) for the diagnosis of melanoma is currently 15.6 globally. This number should be cut down to reduce the morbidity and stress of patients bound to multiple surgeries and the costs burdening the healthcare system.

The first publication, in the literature, on the use of LC-OCT for the diagnosis of skin cancer dates back to 2018. [51] Since then, 112 articles have been published on this topic, but of these only 8 regarding the diagnosis of melanocytic lesions, which represent the main cause of oncological mortality in the dermatological field.

LC-OCT is a device that has numerous advantages compared to other non-invasive diagnostic tools: it is a rapid method that can be carried out on an outpatient basis, it has cellular resolution (keratinocytes, melanocytes and cells of the immune system up to a depth of approximately 500 micrometres can be identified) and also allows a vertical histological-like and 3D view of the lesions being analysed. Finally, last but not least, it is equipped with a dermoscopic-like camera that allows to know exactly the area of the lesion that is being investigated. Despite these advantages, distinguishing benign melanocytic lesions, particularly if dysplastic, from melanoma, is currently challenging with this method. These difficulties are partly due to a long learning curve required by the device and because melanocytic lesions represent biologic entities that are often difficult to diagnose even for pathologists who use different combinations of immunohistochemical stains to identify antigens most frequently found in melanomas.

In this scenario, AI algorithms can be applied to LC-OCT images to improve the dermatologist's diagnostic performance. In 2023, Thamm et al[70] trained a Convolutional Neural Networks (CNNs) for automated PRO score quantification of Actinik Keratosis (AK) using vertical section of LC-OCT images.
This score is based on the evaluation of the number of protrusions, the depth of protrusion and the ondulation of the DEJ to predict the risk of evolution of an actinic keratosis into squamous cell carcinoma. In this case, for each image of the training set the ground truth contour of the DEJ was annotated manually by an operator, then segmentation models were first trained to segment skin layers on the healthy skin dataset and subsequently finetuned on images from the AK dataset.

The goal of developing an AI model capable of distinguishing benign melanocytic lesions from melanoma is much more ambitious and challenging. First of all, melanocytic lesions are not unique biological entities but encompass a range of lesions with different histological characteristics (e.g. junctional melanocytic nevus, compound melanocytic nevus, Spitz nevus, blue nevus). [71]
In addition, there are lesions, dysplastic nevi, whose potential to develop into melanoma is currently unclear.

Today's gold standard for the diagnosis of melanoma is represented by histopathological evaluation. This is based on a series of architectural criteria and a group of cytological criteria to make a diagnosis (Table 8).

Histological features of melanoma
Architectural features
Asymmetry
Poor circumscription
Ulceration
Consumption of the epidermis
Epidermal nests of melanocytes showing:
• *Confluence*
• *Expansion*
• *Variability in size and shape*

• *Haphazard interval and array*
Solitary epidermal melanocytes showing:
• *Predominance over nests*
• *Pagetoid spread*
• *Haphazard arrangement*
• *Confluent lentiginous growth*
Dermal nests showing:
• *Variability in size and shape*
• *Confluence*
• *Lack of maturation in depth*
• *Variability in melanin distribution*
Melanocytes within lymphovascular spaces
Neurotropism

Cytological criteria
Nuclear pleomorphism
Nucleolar variability (size and number)
Mitoses (increased, deep, and/or atypical)
Apoptosis increased

Table 8. Histopathological criteria for the diagnosis of melanoma.

This variety and biological complexity represent a first difficulty in the possibility of identifying clear criteria for training an AI model.
Furthermore, unlike the study proposed by Thamm et al[69] for actinic keratoses, all segments of the lesion must be taken into consideration for our analysis (the epidermis for the assessment of consumption or the evidence of pagetoid spread, the DEJ for the assessment of junctional nests and lentiginous growth, the dermis for the evaluation of dermal nests and melanocytes maturation).

The first part of the work consisted in describing the appearance of benign and malignant melanocytic lesions on LC-OCT. [61,72]
The next step was the description of LC-OCT criteria that would allow a distinction between benign and malignant melanocytic lesions (Table 6). [62]
Starting from these criteria we identified the ROIs for training our machine learning models. At the beginning, we tried to operate a manual segmentation of the images, contouring the DEJ to help the algorithm in distinguishing epidermis from the dermis.

This turned out to be a very time-consuming procedure, which was overcome by seeing how the automatic clustering procedure well reflected the anatomical division into epidermis, DEJ and dermis (Figure 28).
The image biomarkers were IBSI compliant and widely used in radiomics.[66-68]
The univariate analysis found 127 possible biomarkers useful for distinguishing dysplastic nevi/nevi from melanomas.
The variables with lower p-values were intensity-based statistical features such as kurtosis (kurt), that is is a measure of peakedness in the intensity distribution, intensity skewness (skew) (the skewness of intensity distribution) and the intensity-based robust mean absolute deviation (rmad).
However, also grey level distance zone-based features and grey level co-occurrence-based features showed a significant p-value such as large distance emphasis (lgze) and autocorrelation (cm.auto.corr).
The identification of these biomarkers is consistent with the anatomical diversity of benign and malignant lesions, since the presence of pagetoid melanocytic cells in the epidermis as well as that of confluent melanocytic nests in the epidermis, DEJ or dermis can be reflected in variations in intensity and gray levels.

With a forward feature selection strategy, the most promising bivariate regression models were extracted. To limit overfitting, a 7:3 cross-fold validation was used.
In the feature/AUC diagram showed in the results section it is possible to see the averages of the AUCs of the built models, once these have been ordered from the most performing to the least. In blue the performances on the training set, in red on the testing set.
As expected, the performances on the training set are high, while those on the testing set are lower: this means that apparently good results of this technique are probably due to overfitting. Plotting the dispositions of melanoma vs non-melanoma in the space of the biomarkers that had apparently better performances on the training set, it also emerges visually that space is not linearly separable, so the overfitting hypothesis is credible (results section).
These graphs perhaps suggest that we could have better PPV (positive predicting value) and NPV (negative predicting value) if we tried to set up a Support Vector Machine with

a Gaussian kernel: however, this this is not currently feasible given the small number of positive cases (it should be reconsidered after recruiting other melanoma cases).
Similarly, the decision tree and the random forest also showed excellent levels of accuracy, PPV and NPV for the training test with a drop in performance on the independent internal testing set.

6. CONCLUSIONS

In this pilot study we developed and demonstrated, for the first time in the literature, the feasibility of an artificial intelligence model for the in-vivo discrimination between benign melanocytic lesions, uncertain malignant potential lesions and melanoma based on LC-OCT images.
We have identified several biomarkers potentially useful for this purpose.
Although this model has not yet demonstrated good results in terms of performance, it could be improved in several ways: first of all, by using a higher number of images, in particular those that were currently less represented (melanomas). Secondly, given the variety of melanocytic lesions, it might be appropriate to start training our model with a more simplified set (for example including only lesions of the body and not of the face, which are anatomically different), thus avoiding selection bias.
Finally, it may be appropriate to make changes in the filters used and in the selection of ROIs, opting for a mixed approach (manual and automatic).

7. BIBLIOGRAPHY

1. Rigel DS, Carucci JA. Malignant melanoma: prevention, early detection, and treatment in the 21st century. CA Cancer J Clin 2000; 50:215-362.
2. Kosary CL, Altekruse SF, Ruhl J et al. Clinical and prognostic factors for melanoma of the skin using SEER registries: collaborative stage data collection system, version 1 and version 2. Cancer 2014; 120:3807-14.
3. Linos E, Swetter SM, Cockburn MG et al. Increasing burden of melanoma in the United States. J Invest Dermatol 2009; 129:1666-74.
4. Glazer AM, Rigel DS, Winkelmann RR, Farberg AS. Clinical Diagnosis of Skin Cancer: Enhancing Inspection and Early Recognition. Dermatol Clin 2017; 35:409-416.
5. Woltsche N, Schwab C, Deinlein T et al. Dermoscopy in the era of dermato-oncology: from bed to bench side and retour. Expert Rev Anticancer Ther 2016; 16:531-41.
6. Fuller SR, Bowen GM, Tanner B et al. Digital dermoscopic monitoring of atypical nevi in patients at risk for melanoma. Dermatol Surg 2007; 33:1198-206.
7. Kittler H, Pehamberger H, Wolff K, Binder M. Diagnostic accuracy of dermoscopy. Lancet Oncol 2002; 3:159-65.
8. Kollias N, Stamatas GN. Optical non-invasive approaches to diagnosis of skin diseases. J Investig Dermatol Symp Proc 2002; 7:64-75.
9. Fink C, Haenssle HA. Non-invasive tools for the diagnosis of cutaneous melanoma. Skin Res Technol 2017; 23:261-271.
10. Konig K, Riemann I. High-resolution multiphoton tomography of human skin with subcellular spatial resolution and picosecond time resolution. J Biomed Opt 2003; 8:432-9.
11. De Vries E, Bray FI , Eggermont AM , Coebergh JW . European Network of Cancer Registries. Monitoring stage specific trends in melanoma incidence across Europe reveals the need for more complete information on diagnostic characteristics. Eur J Canc Pr 2004;13:387-95.
12. Whiteman DC, Whiteman CA, Green AC. Childhood sun exposure as risk factor for melanoma: a systematic review of epidemiological studies. Cancer Causes Control 2001;12(1):69 82.

13. Fitzpatrick's Dermatology In General Medicine (Two Vol. Set) 6th edition (May 23, 2003).
14. Fargnoli MC, Argenziano G, Zalaudek I, Peris K. High and low penetrance cutaneous melanoma susceptibily genes. Expert Rev Anticancer Ther 2006;6:657-70.
15. Omholt K, Karsberg S, Platz A, Kanter L, Ringborg U, Hansson J. N-RAS and BRAF mutations arise early during melanoma pathogenesis and are preserved throughout tumor progression. Clin Cancer Res2003;9(11):6483-88.
16. Cadet J, Sage E, Douki T. Ultraviolet radiation-mediated damage to cellular DNA. Mutat Res 2005;571:3-17.
17. Van't Veer LJ, Burgering BMT, Versteeg R. N-RAS mutations in human cutaneous melanoma from sun-exposed body sites. Mol Cell Biol1989;9:3114-16.
18. Cohen Y, Rosenbaum E, Begum S, Goldenberg D, Esche C, Lavie O, Sidransky D, Westra WH. Exon 15 BRAF mutations are uncommon in melanoma arising in nonsun exposed sites. Clin Cancer Res 2004;15:3444 3447.
19. de Gruijl FR1 van Kranen HJ, van Schanke A. UV exposure, genetic targets in melanocytic tumors and transgenic mouse models. J Photochem Photobiol 2005;81:52-64.
20. Ryan JW, Anderson PH, Morris HA. Pleiotropic Activities of Vitamin D Receptors -Adequate Activation for Multiple Health Outcomes. Clin Biochem Rev 2015;36(2):53-61.
21. Del Marmol V, Ortonne JP. Groundwork for the prevention of melanoma in Europe. J Eur Acad Dermatol Venereol 2015;29:1.
22. Berwick M, Armstrong BK, Ben-Porat L, Fine J, Kricker A, Eberle C, Barnhill R. Sun exposure and mortality from melanoma. J Natl Cancer Inst 2005; 97:195.
23. Glodman L. Some investigative studies of pigmented nevi with cutaneous microscopy. J Invest Dermatol 1951;16:407-27.
24. Vestergaard ME, Macaskill P, Holt PE, Menzies SW. Dermoscopy compared with naked eye examination for the diagnosis of primary melanoma: a meta-analysis of studies performer in a clinical setting. Br J Dermatol 2008;159:669-76.
25. Rosendahl C, Tschandl P, Cameron A, Kittler H. Diagnostic accuracy of dermatoscopy for melanocytic and nonmelanocytic pigmented lesions. J Am Acad

Derm 2011;64(6):1068-73.

26. Kreusch JF. Vascular pattern in skin tumors. Clin Dermatol 2002;20:248-54.
27. Argenziano G, Zalaudek I, Corona R, Sera F, Cicale L, Petrillo G, Ruocco E, Hofmann-Wellenhof R, Soyer HP. Vascular structures in skin tumors: a dermoscopy study. Arch Dermatol 2004;140:1485-9.
28. Malvehy J, Puig S, Argenziano G, Marghoob AA, Soyer HP; International Dermoscopy Society Board members. Dermoscopy report: proposal for standardization. Result of a consensus meeting on the International Dermoscopy Society. J Am Acad Dermatol 2007;57:84-95.
29. Pehamberger H, Steiner A, Wolff K. In vivo epiluminescence microscopy of pigmented skin lesions. Pattern analysis of pigmented skin lesions. J Am Acad Dermatol 1987;17:571-583.
30. Argenziano G, Fabbrocini G, Carli P, De Giorgi V, Sammarco E, Delfino M. Epiluminescence microscopy for the diagnosis of doubtful melanocytic lesions. Comparison of the ABCD rule of dermatoscopy and a new 7-point checklist based on pattern analysis. Arch Dermatol 1996;132:1178-1182.
31. Argenziano G, Catricalà C, Ardigo M, Buccini P, De Simone P, Eibenschutz L, Ferrari A, Mariani G, Silipo V, Sperduti I, Zalaudek I. Seven-point checklist of dermoscopy revisited. Br J Dermatol 2011;164:785-790.
32. Yélamos O, Braun RP, Liopyris K et al. Dermoscopy and dermatopathology correlates of cutaneous neoplasms. J Am Acad Dermatol 2019; 80:341-363.
33. Rezze GG, Scramim AP, Neves RI, Landman G. Structural correlations between dermoscopic features of cutaneous melanomas and histopathology using transverse sections. Am J Dermatopathol. 2006 Feb;28:13-20.
34. Shahriari N, Grant-Kels JM, Rabinovitz H et al. Reflectance confocal microscopy: Diagnostic criteria of common benign and malignant neoplasms, dermoscopic and histopathologic correlates of key confocal criteria, and diagnostic algorithms. J Am Acad Dermatol 2021; 84:17-31.
35. V. Ahlgrimm-Siess, R.G.B. Langley, R. Hofmann-Wellenhof. Solar lentigo, seborrheic keratosis and lichen planus-like keratosis. R. Hofmann-Wellenhof, G. Pellacani, J. Malvehy, H.P. Soyer (Eds.), Reflectance Confocal Microscopy for Skin Diseases (1st ed.), Springer, New York (2012), pp. 259-273.

36. P. Calzavara-Pinton, C. Longo, M. Venturini, R. Sala, G. Pellacani. Reflectance confocal microscopy for in vivo skin imaging. Photochem Photobiol, 84 (2008), pp. 1421-1430.
37. M. Rajadhyaksha, M. Grossman, D. Esterowitz, R.H. Webb, R.R. Anderson. In vivo confocal scanning laser microscopy of human skin: melanin provides strong contrast. J Invest Dermatol, 104 (1995), pp. 946-952.
38. A. Scope, C. Benvenuto-Andrade, A.L.C. Agero, et al. In vivo reflectance confocal microscopy imaging of melanocytic skin lesions: consensus terminology glossary and illustrative images. J Am Acad Dermatol, 57 (2007), pp. 644-658
39. M. Huzaira, F. Rius, M. Rajadhyaksha, R.R. Anderson, S. González. Topographic variations in normal skin, as viewed by in vivo reflectance confocal microscopy. J Invest Dermatol, 116 (2001), pp. 846-852.
40. M. Rajadhyaksha, S. González, J.M. Zavislan, R.R. Anderson, R.H. Webb. In vivo confocal scanning laser microscopy of human skin II: advances in instrumentation and comparison with histology. J Invest Dermatol, 113 (1999), pp. 293-303.
41. K.J. Busam, C. Charles, G. Lee, A.C. Halpern. Morphologic features of melanocytes, pigmented keratinocytes, and melanophages by in vivo confocal scanning laser microscopy. Mod Pathol, 14 (2001), pp. 862-868.
42. A. Levine, O. Markowitz. Introduction to reflectance confocal microscopy and its use in clinical practice. JAAD Case Rep, 4 (2018), pp. 1014-1023.
43. S. Borsari, R. Pampena, A. Lallas, et al. Clinical indications for use of reflectance confocal microscopy for skin cancer diagnosis. JAMA Dermatol, 152 (2016), pp. 1093-1098.
44. A. Stevenson, S. Mickan, S. Mallett, M. Ayya. Systematic review of diagnostic accuracy of reflectance confocal microscopy for melanoma diagnosis in patients with clinically equivocal skin lesions. Dermatol Pract Concept, 3 (2013), pp. 19-27.
45. C. Navarrete-Dechent, M. Cordova, S. Aleissa, et al. Reflectance confocal microscopy confirms residual basal cell carcinoma on clinically negative biopsy sites before Mohs micrographic surgery: a prospective study. J Am Acad Dermatol, 81 (2019), pp. 417-426.

46. M. McLeod, S. Choudhary, G. Giannakakis, K. Nouri. Surgical treatments for lentigo maligna: a review. Dermatol Surg, 37 (2011), pp. 1210-1228.
47. P. Guitera, F.J. Moloney, S.W. Menzies, et al. Improving management and patient care in lentigo maligna by mapping with in vivo confocal microscopy. JAMA Dermatol, 149 (2013), pp. 692-698.
48. J.M. Guilera, A. Barreiro Capurro, C. Carrera Alvárez, S. Puig Sardá. The role of reflectance confocal microscopy in clinical trials for tumor monitoring. Dermatol Clin, 34 (2016), pp. 519-526.
49. K.L. Connolly, R.I. Nijhawan, S.W. Dusza, K.J. Busam, K.S. Nehal. Time to local recurrence of lentigo maligna: implications for future studies. J Am Acad Dermatol, 74 (2016), pp. 1247-1248.
50. M. Ardigo, M. Agozzino, C. Franceschini, F. Lacarrubba. Reflectance confocal microscopy algorithms for inflammatory and hair diseases. Dermatol Clin, 34 (2016), pp. 487-496.
51. Dubois A, Levecq O, Azimani H et al. Line-field confocal optical coherence tomography for high-resolution noninvasive imaging of skin tumors. J Biomed Opt 2018; 23:1-9.
52. Ruini C, Schuh S, Sattler E, Welzel J. Line-field confocal optical coherence tomography-Practical applications in dermatology and comparison with established imaging methods. Skin Res Technol. 2021 May;27(3):340-352.
53. Suppa M, Fontaine M, Dejonckheere G, Cinotti E, Yélamos O, Diet G, Tognetti L, Miyamoto M, Orte Cano C, Perez-Anker J, Panagiotou V, Trepant AL, Monnier J, Berot V, Puig S, Rubegni P, Malvehy J, Perrot JL, Del Marmol V. Line-field confocal optical coherence tomography of basal cell carcinoma: a descriptive study. J Eur Acad Dermatol Venereol. 2021 May;35(5):1099-1110.
54. Gonzalez S, Tannous Z. Real-time, in vivo confocal reflectance microscopy of basal cell carcinoma. J Am Acad Dermatol 2002; 47: 869–874.
55. Hussain AA, Themstrup L, Jemec GB. Optical coherence tomography in the diagnosis of basal cell carcinoma. Arch Dermatol Res 2015; 307: 1–10.
56. Boone M, Suppa M, Miyamoto M et al. Three-dimensional high-definition optical coherence tomography image acquisition procedure for basal cell carcinoma. Br J Dermatol 2015; 172: 1153–1154.

57. Cinotti E, Tognetti L, Cartocci A, Lamberti A, Gherbassi S, Orte Cano C, Lenoir C, Dejonckheere G, Diet G, Fontaine M, Miyamoto M, Perez-Anker J, Solmi V, Malvehy J, Del Marmol V, Perrot JL, Rubegni P, Suppa M. Line-field confocal optical coherence tomography for actinic keratosis and squamous cell carcinoma: a descriptive study. Clin Exp Dermatol. 2021 Dec;46(8):1530-1541.
58. Schuh S, Ruini C, Perwein MKE, Daxenberger F, Gust C, Sattler EC, Welzel J. Line-Field Confocal Optical Coherence Tomography: A New Tool for the Differentiation between Nevi and Melanomas? Cancers (Basel). 2022 Feb 23;14(5):1140.
59. Perez-Anker J, Puig S, Alos L, García A, Alejo B, Cinotti E, Orte Cano C, Tognetti L, Lenoir C, Monnier J, Machuca N, Castillo P, Gibert PR, Rubegni P, Suppa M, Perrot JL, Del Marmol V, Malvehy J. Morphological evaluation of melanocytic lesions with three-dimensional line-field confocal optical coherence tomography: correlation with histopathology and reflectance confocal microscopy. A pilot study. Clin Exp Dermatol. 2022 Aug 21.
60. Verzì AE, Broggi G, Caltabiano R, Micali G, Lacarrubba F. Line-field confocal optical coherence tomography of lentigo maligna with horizontal and vertical histopathologic correlations. J Cutan Pathol. 2022 Sep 3.
61. Soglia S, Pérez-Anker J, Albero R, Alós L, Berot V, Castillo P, Cinotti E, Del Marmol V, Fakih A, García A, Lenoir C, Monnier J, Perrot JL, Puig S, Rubegni P, Skowron F, Suppa M, Tognetti L, Venturini M, Malvehy J. Understanding the anatomy of dermoscopy of melanocytic skin tumours: Correlation in vivo with line-field optical coherence tomography. J Eur Acad Dermatol Venereol. 2024 Jun;38(6):1191-1201.
62. Perez-Anker J, Soglia S, Lenoir C, Albero R, Alos L, García A, Alejo B, Cinotti E, Orte Cano C, Habougit C, Dorado Cortes C, Pellegrino L, Tognetti L, Castillo P, Rubegni P, Suppa M, Perrot JL, Del Marmol V, Puig S, Malvehy J. Criteria for melanocytic lesions in LC-OCT. J Eur Acad Dermatol Venereol. 2024 May 10.
63. Suppa M, Palmisano G, Tognetti L, Lenoir C, Cappilli S, Fontaine M, Orte Cano C, Diet G, Perez-Anker J, Schuh S, DI Stefani A, Lacarrubba F, Puig S, Malvehy J, Rubegni P, Welzel J, Perrot JL, Peris K, Cinotti E, Del Marmol V. Line-field confocal optical coherence tomography in melanocytic and non-melanocytic skin

tumors. Ital J Dermatol Venerol. 2023 Jun;158(3):180-189.

64. Bao Zhou. Image Segmentation using SLIC Superpixels and Affinity Propagation Clustering. International Journal of Science and Research. 2015 April, 4(4): 1525-1529.

65. Dinapoli N, Alitto AR, Vallati M, Gatta R, Autorino R, Boldrini L, Damiani A, Valentini V. Moddicom: a complete and easily accessible library for prognostic evaluations relying on image features. Annu Int Conf IEEE Eng Med Biol Soc. 2015 Aug;2015:771-4.

66. Zwanenburg A, Leger S, Valli`eres M, L¨ock S. Image biomarker standardisation initiative. arXiv preprint arXiv:1612.07003.

67. Lambin P, Leijenaar RT, Deist TM, Peerlings J, de Jong EE, van Timmeren J, Sanduleanu S, Larue RT, Even AJ, Jochems A, van Wijk Y. Radiomics: the bridge between medical imaging and personalized medicine. Nature Reviews Clinical Oncology. 2017 Dec;14(12):749.

68. Lambin P. Radiomics Digital Phantom, CancerData (2016), DOI:10.17195/candat.2016.08.1

69. Arnold M, Singh D, Laversanne M, Vignat J, Vaccarella S, Meheus F, Cust AE, de Vries E, Whiteman DC, Bray F. Global Burden of Cutaneous Melanoma in 2020 and Projections to 2040. JAMA Dermatol. 2022 May 1;158(5):495-503.

70, Thamm JR, Daxenberger F, Viel T, Gust C, Eijkenboom Q, French LE, Welzel J, Sattler EC, Schuh S. Artificial intelligence-based PRO score assessment in actinic keratoses from LC-OCT imaging using Convolutional Neural Networks. J Dtsch Dermatol Ges. 2023 Nov;21(11):1359-1366.

71. Patterson, James W., et al. *Weedon's Skin Pathology*. Fifth edition, Elsevier, 2021

72. Soglia S, Pérez-Anker J, Albero R, Alós L, Berot V, Castillo P, Cinotti E, Del Marmol V, Dorado Cortez C, Fakih A, García A, Lenoir C, Monnier J, Perrot JL, Puig S, Rubegni P, Suppa M, Tognetti L, Venturini M, Malvehy J. Understanding anatomy of dermoscopy of melanocytic skin tumors part 2: correlation in vivo with line-field optical coherence tomography of melanocytic and other pigmented facial lesions. Submitted elsewhere.